UCRL-ID-104582
PATC-IR 89-12

DEVELOPMENT OF SOIL/ROCK CONSTITUTIVE MODELS AND BENCHMARK ANALYSIS FOR GAS-GUN PENETRATION TESTS AT THE PSA FLIGHT 1771 CRASH SITE

March 22, 1990

J. C. Chen, M. C. Witte

Prepared for
U.S. Nuclear Regulatory Commission

DISCLAIMER

This work was supported by the United States Nuclear Regulatory Commission under a Memorandum of Understanding with the United States Department of Energy.

PATC-IR 89-12

DEVELOPMENT OF SOIL/ROCK CONSTITUTIVE MODELS AND BENCHMARK ANALYSIS FOR GAS-GUN PENETRATION TESTS AT THE PSA FLIGHT 1771 CRASH SITE

March 22, 1990

J. C. Chen, M. C. Witte

Prepared for
U.S. Nuclear Regulatory Commission

ABSTRACT

A series of studies have been conducted for the purpose of understanding the crash environment and impact conditions of the PSA Flight 1771 crash on December 7, 1987 which has been specified by the Nuclear Regulatory Commission as representing the "worst case" accident. This information is needed for establishing the criteria for suitable package development tests and for an aircraft crash test that would replicate the conditions of the PSA Flight 1771 crash.

The work reported here is part of the study defining the aircraft impact environment. In particular, the results of the geotechnical investigation of the PSA Flight 1771 site are summarized here. The site characteristics and the geotechnical properties at the PSA Flight 1771 crash site were developed from extensive field investigations and laboratory tests. Field investigations consisted of topography surveys, exploratory borings, seismic refraction measurements, and dynamic penetration tests. Laboratory tests measured the basic material properties, compressibility characteristics, and the stress-strain behaviors of the soil/rock samples. The results of laboratory tests were used for the development of soil/rock constitutive models for dynamic impact analysis.

Four gas-gun penetration tests were conducted at the PSA Flight 1771 crash site. The results and the data of the penetration tests were used as a benchmark of the developed constitutive model and finite element codes DYNA2D and DYNA3D. These codes were used for conducting impact-crash analyses in support of the criteria for development (controlled) tests used in the design of plutonium air transport packages. Input parameters for the best-estimate, the upper, and the lower bound models were developed and provided for the PSA Flight 1771 crash site. In addition, three other soil models are also provided for conducting finite element impact analyses that provide a methodology for establishing the equivalence between impact velocity of a package on an arbitrary surface and an unyielding surface.

TABLE OF CONTENTS

LIST OF FIGURES

LIST OF TABLES

Tables

ACKNOWLEDGMENTS

The work described in this report was carried out in support of the Plutonium Air Transport Certification (PATC) Program, conducted by the Nuclear Systems Safety Program (NSSP) at Lawrence Livermore National Laboratory for the U.S. Nuclear Regulatory Commission (NRC). John Jankovich and John Cook of the NRC provided guidance of this work.

Carl Walter and Larry Fischer provided valuable technical and administrative reviews of this report. C. K. Chou provided expert program leadership for administrative guidance and support. Jim VanSant and Jerry Goudreau gave technical advice in various areas of modeling and analysis.

Garry Holman and Dave Carpenter conducted the geotechnical investigation of the crash site. Mark Eli assisted in the early development of the model. Steve Blair conducted the laboratory tests on rock samples and C. Y. Chang of Geomatrix Consultants, Inc. conducted the laboratory tests on soil samples. C. W. Young of Sandia National Laboratory, Albuquerque, conducted the gas-gun penetration tests. Mike Chiesa of Sandia National Laboratory, Livermore, provided valuable geotechnical data of other sites.

Finally, Merry Carter, Millie Heim and Dawn Matz typed the manuscript. Marilyn Kamelgarn edited the manuscript. Lisa Hensel and Ellen Strumer provided publication services.

1. INTRODUCTION

This report presents results of a benchmark analysis for gas-gun penetration tests at the PSA Flight 1771 crash site near Paso Robles, California. This analysis helps to determine the constitutive properties of the crash site most suitable for conducting crash-impact analyses in support of appropriate development tests for the design of plutonium air transport (PAT) packages that meet requirements to be established. The characteristics and constitutive relationship for the geological materials at the PSA Flight 1771 crash site must also be evaluated in support of the development of crash site criteria for aircraft crash test (Ref. 1). This study is one of a series of studies in defining the aircraft impact environment for the Plutonium Air Transport Certification (PATC) Program being conducted for the U.S. Nuclear Regulatory Commission (NRC) by the Nuclear Systems Safety Program (NSSP) of the Lawrence Livermore National Laboratory (LLNL).

1.1 Background

Section 5062 of Public Law 100-203 is concerned with air shipment of plutonium from one foreign country to another through United States airspace. It applies specifically to the packages in which the plutonium is shipped, requiring that the packages be certified by the NRC as safe for the purpose and that the packages must be able to survive the worst aircraft accident without releasing significant quantities of the plutonium.

The law requires certain tests to be conducted in the certification process. These tests include a drop test of the package and a crash test of the cargo aircraft with test packages aboard to replicate actual worst-case aircraft accident conditions. In lieu of the aircraft crash test, tests used in the development of the package may be substituted, provided that an independent scientific review group agrees that these development tests produce load conditions that exceed those encountered in a worst-case accident. The NRC specified that the conditions associated with the crash of PSA Flight 1771 on December 7, 1987, represent a worst-case aircraft accident and therefore are suitable for use as the basis for the required tests.

In order to assure adequacy of testing, the geotechnical characteristics of the aircraft crash test or drop test site must be similar or more resistant to impact than the site where PSA Flight 1771 crashed. Gas-gun penetration tests at the PSA Flight 1771 site provide the data (e.g., S-number) for the characterization of the site under the condition of high-velocity impact. The data are essential in support of the development of crash site criteria for the required tests. In addition, the measured deceleration responses and penetration depths obtained from the penetration tests were used as a benchmark to determine the most suitable constitutive properties of the PSA Flight 1771 crash site. These constitutive properties are required for conducting finite element impact analyses in support of draft criteria for development (controlled) package tests.

Four gas-gun penetration tests were conducted at the PSA Flight 1771 crash site on May 22-24, 1989. Sandia National Laboratory (SNL) performed the tests at the request of LLNL. Because the Earth Penetration Weapon (EPW) program of SNL was interested in obtaining penetration data into intensely weathered sandstone and claystone to fill a gap in their penetration data base, SNL provided partial support by supplying penetrators and instrumentations for the tests. The data and results of the gas-gun tests are documented in Ref. 2.

1.2 Objectives and Scope

Subsequent to the gas-gun penetration test, LLNL conducted an analytical study to determine the best method of modeling this sandstone-and-shale site for impact conditions using the finite element codes DYNA2D and DYNA3D (Refs. 3 and 4). The eventual purpose was to develop a model suitable for use in finite element impact calculations of aircraft crashes and package drops. The model itself has been benchmarked against the results reported in Ref. 2. The input parameters for the model are derived from standard geotechnical tests (both in-situ and laboratory) conducted by LLNL. Input parameters for three models are provided for this site: a "best estimate" model, an upper bound model, and a lower bound model.

In support of the development (controlled) test criteria, an unyielding surface equivalence methodology was developed using results obtained from finite element analysis and from empirical equations of the earth penetrator. An extensive finite element analysis was conducted for specific packages (Refs. 5 and 6) impacting on the PSA Flight 1771 crash site and other targets with various hardness. Geotechnical properties and specific model parameters of these targets are required for finite element analysis. Three target materials whose soil constants and geotechnical properties have been published were used for the development of constitutive properties for finite element analysis. These three target materials are (1) intensely weathered and fractured granite (2) low strength unfractured Antelope tuff, and (3) stiff Antelope Lake soil.

1.3 Report Organization

Section 2 summarizes the results of gas-gun tests. One of the penetration tests was selected for the benchmark of the DYNA code with implemented models. Section 3 describes the development of penetrator and target models. For the development of the target model, the main items are: constitutive description, model parameter requirements and evaluation, geotechnical properties, model consideration for scale-fracture and strain effect, and suggested constitutive relations. Section 4 gives the best estimate model based on sensitivity analyses. Calculation results are compared to experimental data. Modeling uncertainty is discussed. The upper and lower bound models are also presented. Finally, constitutive properties for four other geological materials are presented in Section 5. Appendix A presents detailed discussions of scale-fracture and strain-rate effects.

2. GAS-GUN TESTS AT PSA FLIGHT 1771 CRASH SITE

The center of the area for the four earth-penetrator tests is approximately 33 m (100 ft) southeast of the PSA impact point, as shown in Fig. 2-1. At the end of each test, a test pit was excavated to recover the penetrator and to obtain detailed geologic information on the material penetrated. Typical rock samples were collected for laboratory tests to study their characteristic strengths and compressibilities. Detailed geological records of the four test pits were reported by D. W. Carpenter, et al. (Ref. 7). The area selected for the test is the closest location to the impact point where heavy penetrator equipment could gain access to the hillside. Based on our engineering geologic evaluation of the site, the test area is geologically similar to the impact point.

2.1 Penetrator and Instrumentation

The penetrators used in these tests were developed at SNL as part of the Earth-Penetrator-Weapon (EPW) program. The penetrator weighs 35.5 kg (78 lb) and has a conical nose. The dimensions are: 78 cm (30.75 in.) long and 14.7 cm (5.8 in.) diam., with a 15.2 cm (6-in.) base/flare diam. Two acceleration measurement stations were built into the penetrator: the forward station is referred to as FWD, and the afterward station is referred to as AFT. Each station consists of a triaxial set of accelerometers hard-mounted in the data package. Details of the instrumentation package and data system are described in Ref. 2. The dimensions of the penetrator, the accelerometer positions, and the acceleration coordinate system are shown in Fig. 2-2.

Data obtained from the instrumentation provide valuable information for benchmark analysis. Acceleration data were obtained in all four tests. The acceleration time histories were integrated to get the resulting velocity and displacement time histories. The plots of three components of acceleration time histories at both stations (FWD and AFT) and the resulting velocity and displacement time histories in the axial direction (X-axis) for all four tests are shown in Ref. 2. Table 2-1 shows the impact velocities and penetration lengths obtained from integrations of recorded acceleration data. Note that the integration results for the FWD and AFT stations are different due to errors of the data acquisition system. It has been pointed out (Ref. 2) that the accuracy of the system is controlled by the accelerometers, the signal conditioners, and the quantization process. Errors introduced by accelerometers and signal conditioners are controlled by the accuracy of their calibration. The error bound for acceleration due to calibration is 5.4%. The total integration error bound for velocity is 5.9%; for displacement, 7.4%. The integration results of velocity and displacement have been compared to the measured data, and the values were found within the error bounds. Thus, the recorded acceleration time histories and the integrated velocities and displacements are sufficiently accurate for benchmark analyses. The typical acceleration time-history obtained from instrumentation is shown in Fig. 2-3 for the Test No.2. The integrated velocity and displacement from these acceleration data are shown in Figs. 2-4 and 2-5 for the same test.

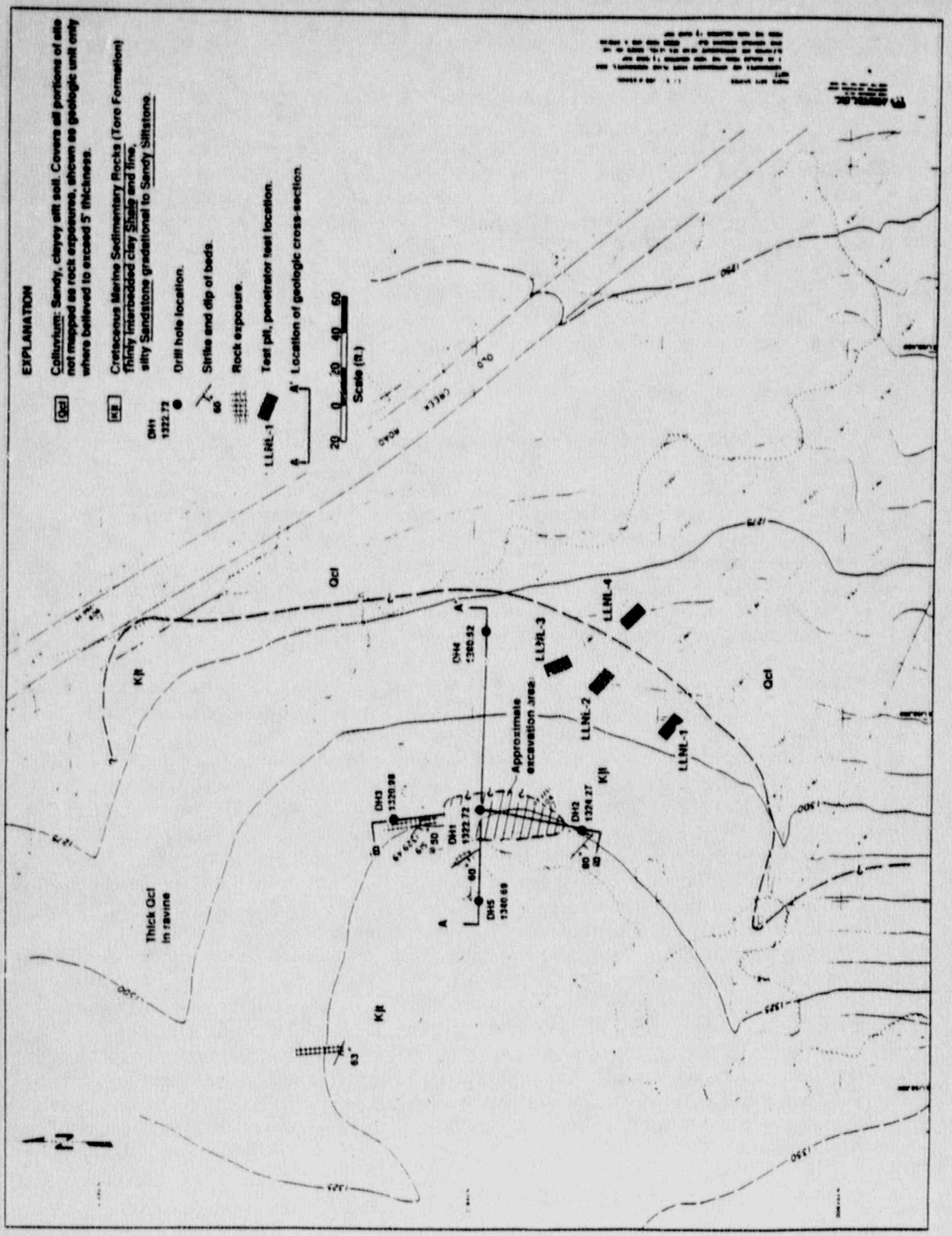

Figure 2-1. Gus-gun test and drill hole locations at PSA Flight 1771 crash site.

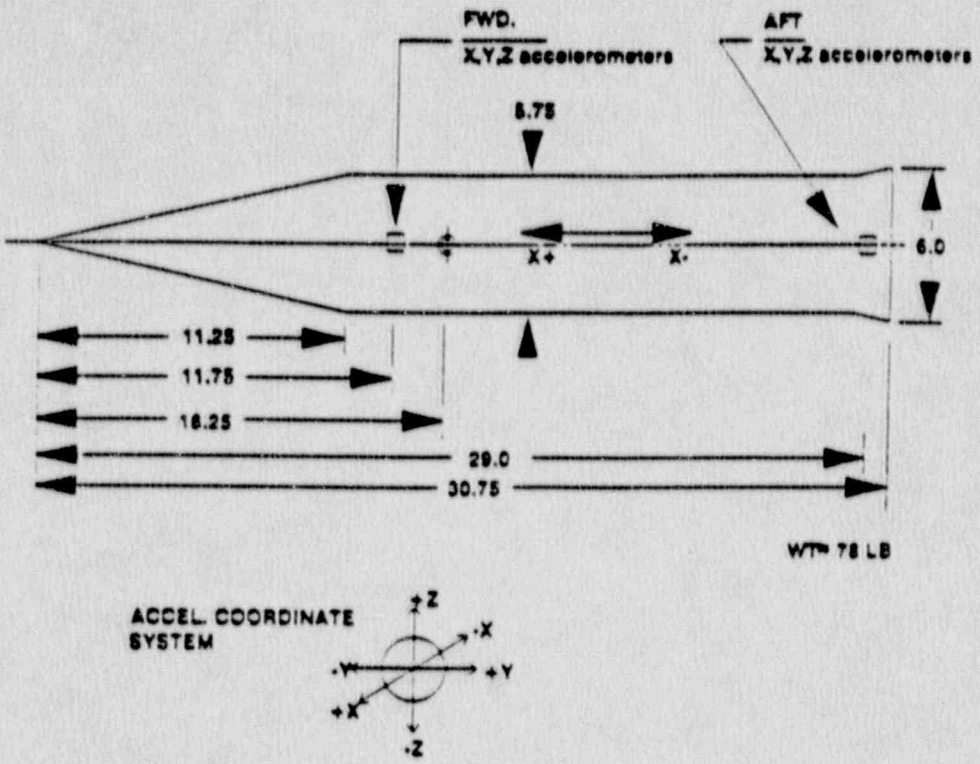

Figure 2-2. The dimensions (inch) of the penetrator, the accelerometer positions, and the acceleration coordinate system.

Table 2-1. Impact velocities and penetration length obtained from integrations of recorded acceleration data.

Test no.	AFT velocity (ft/s)	FWD velocity (ft/s)	Average velocity (ft/s)	AFT pen. length (ft)	FWD pen. length (ft)	Ave. pen. length (ft)
1	658	698	678	5.8	6.1	6.0
2	779	853	816	6.7	7.3	7.0
3	833	905	869	7.8	8.4	8.1
4	868	947	907	12.3	13.4	12.8

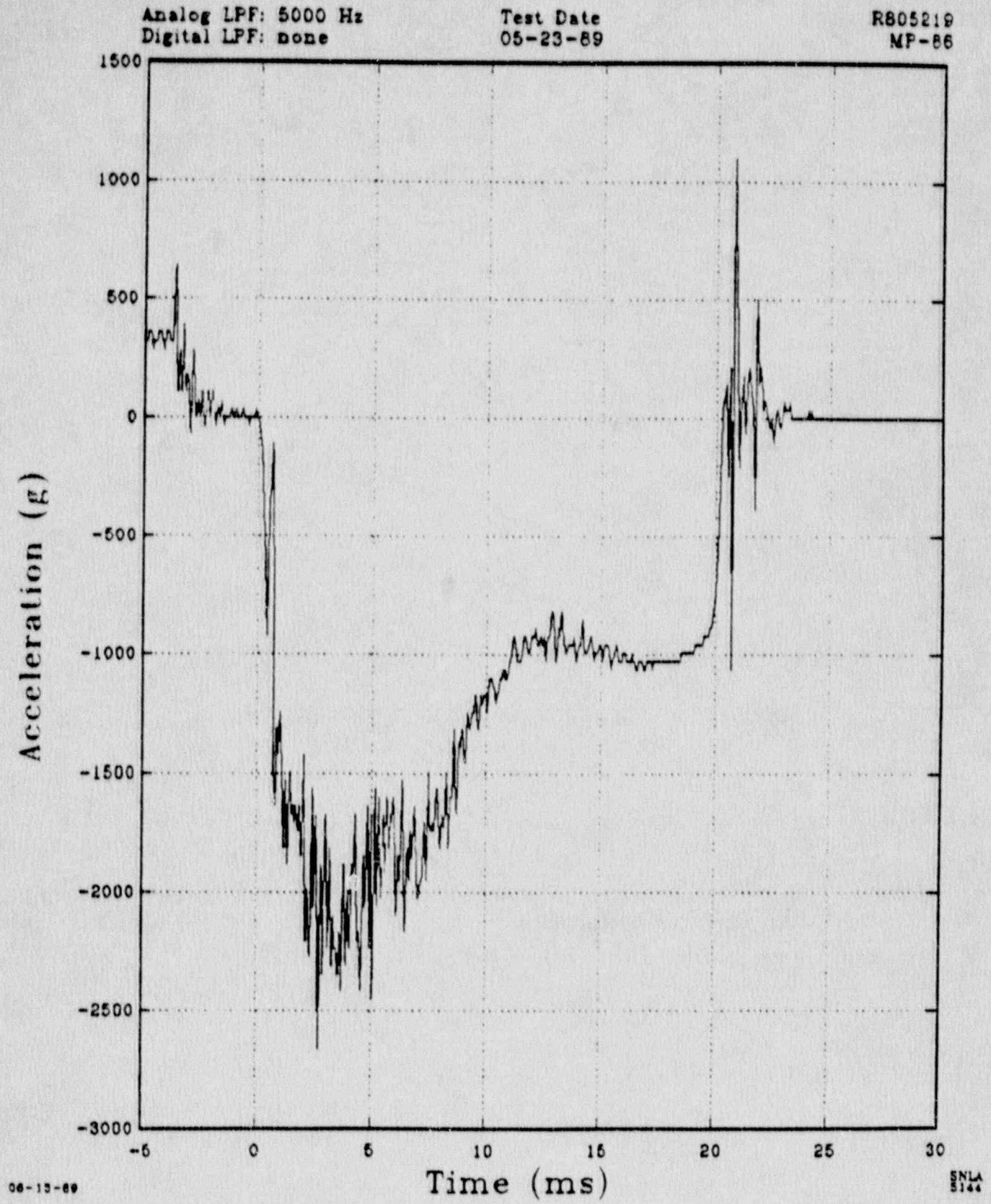

Figure 2-3. The forward axial acceleration time history for Test No. 2.

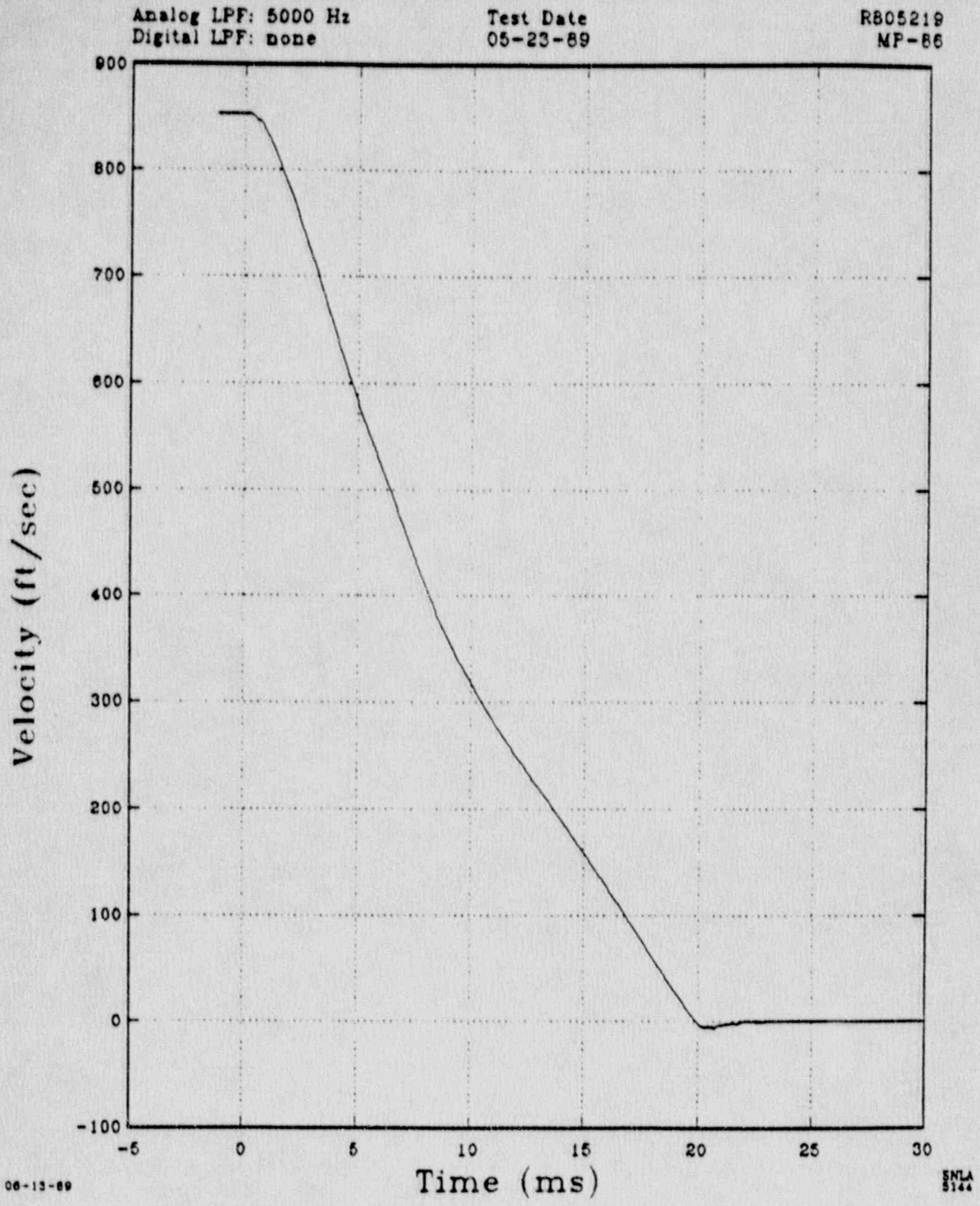

Figure 2-4. The integrated velocity time history from the forward axial acceleration time history of Test No. 2.

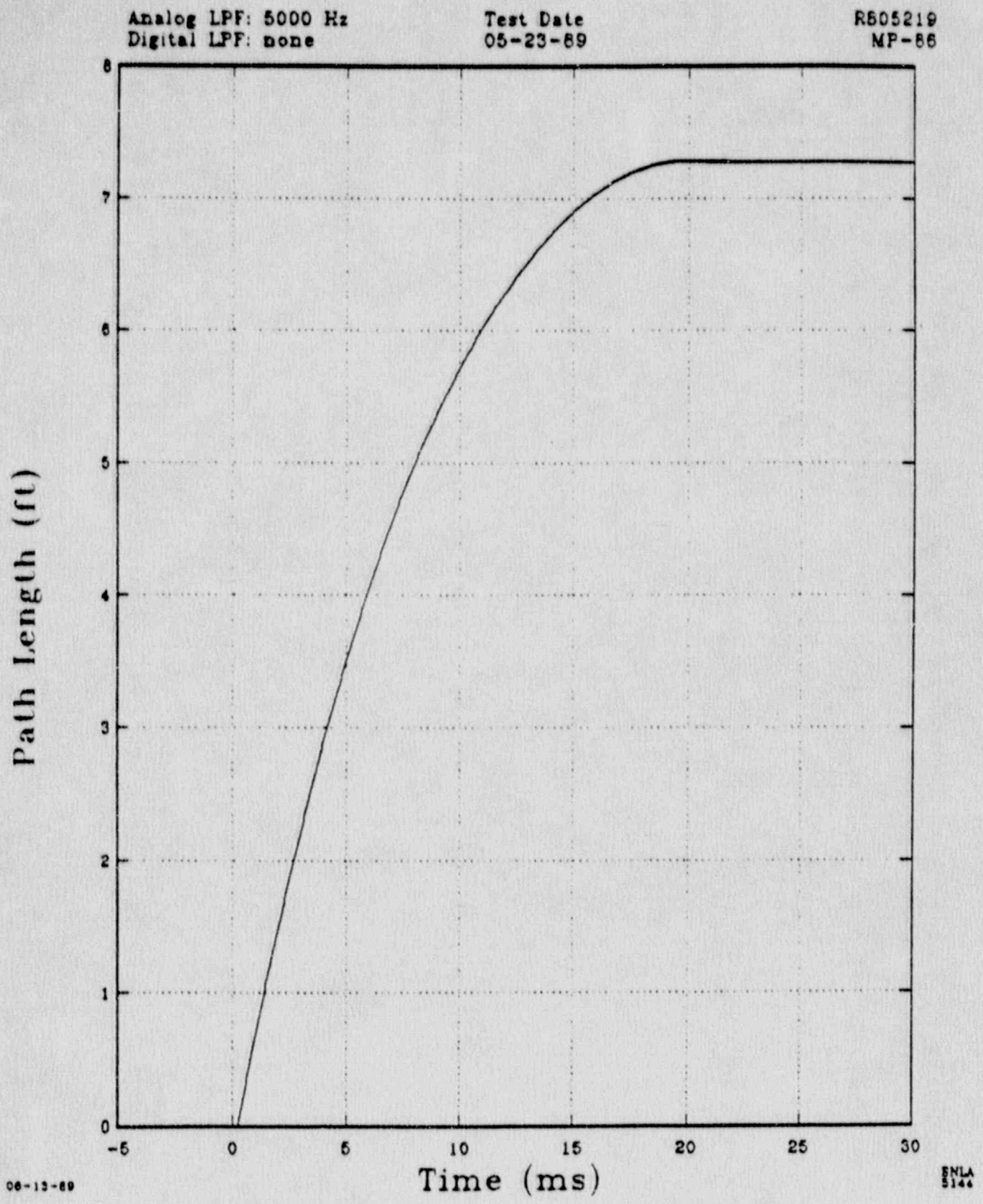

Figure 2-5. The integrated displacement time history from the forward axial velocity time history of Test No. 2.

2.2 Test Ground Conditions

The impact angles and the ground conditions are defined in Fig. 2-6. The ground condition of each test point and the penetration path of each test are briefly described in the following paragraphs.

Test No. 1 The test point is located 110 ft southeast of DH1 and 110 ft southwest of DH4. The site consists of about 2 ft of silty clay and about 4 ft of intensely to moderately weathered clay stone. The ground has a slope of about 19°, and the impact point is about 75° from the lower end of the ground surface. The penetration path was essentially straight in an x-z plane; however, the path was 1° up in an x-y plane at the end of penetration.

Test No. 2 The test point is located about 68 ft southwest of DH4. The ground slope is about 15° from the horizontal plane. The ground consists essentially of intensely to moderately weathered interbedded shale and sandstone. The penetration path curves about 15° downward in an x-y plane, but the path remains symmetrical in an x-z plane. The penetration is about 72° from the lower end of the surface.

Test No. 3 The test point is located 46 ft southwest of DH4. The ground consists essentially of interbedded shale and sandstone, intensely weathered, with moderately weathered lenses. The ground was graded horizontally. The firing direction is about 75° from the ground. The penetration path curved 8° in the direction normal to the penetration path (the x-z plane). This nonsymmetric curvature makes it difficult to model the target for 2-D analysis.

Test No. 4 The test point is located about 40 ft southeast of Test No. 3. During the recovery operation, it was observed that the site consists of 4 ft of stiff clayey silt and 7 ft of interbedded shale and sandstone, decomposed to intensely weathered conditions. The ground was level, and the penetration is about 81° from the ground.

Among these four test points, the ones for Test No. 1 and Test No. 4 are covered by a soil layer. For the ultimate purpose of this study, it is more conservative to select either Test No. 2 or Test No. 3 for benchmark analysis. However, since the penetration path curving in both directions was observed in test Test No. 3, it is more appropriate to select Test No. 2 for DYNA2D analysis.

2.3 Test Results

Prior to the test, the impact velocity for each test was estimated by an empirical chart correlated with the firing pressure accumulated in the power chamber. During the test, photographic coverage included image motion for velocity (2000 frames/sec) and 400 frames/sec movies. The impact velocity for each test was measured by these image motion films. The velocity and displacement of the penetrator were also

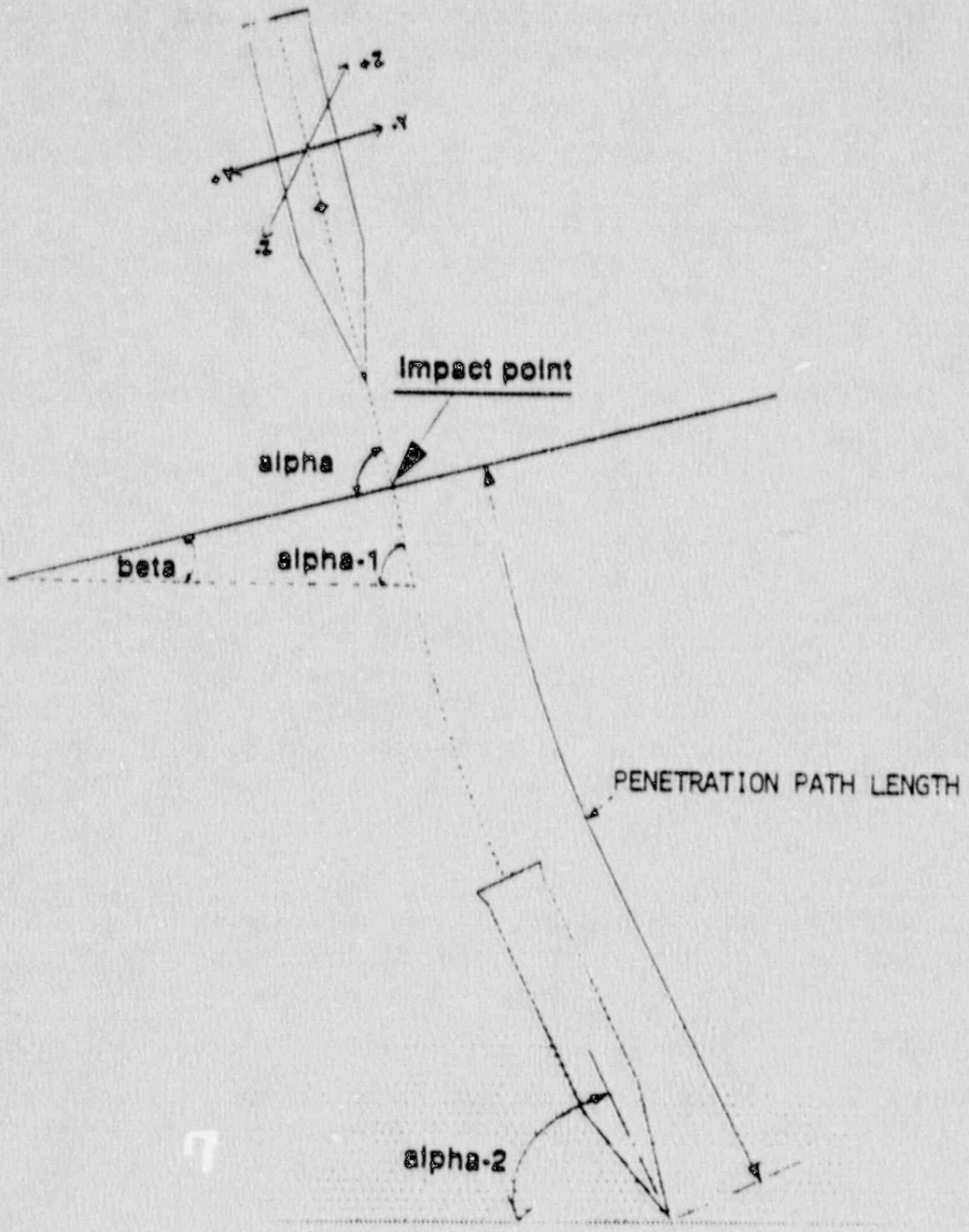

Figure 2-6. The penetrator-target geometry nomenclature.

obtained from the recorded acceleration data received after each test. The penetrator trajectory through the ground was recorded during the recovery operation.

Table 2-2 contains the pertinent data from the four penetrator tests. A comparison of the actual measured data of velocity and displacement of each test with the integrated value shown in Table 2-1 indicates that the differences are within 6% for velocity and within 3% for displacement.

Table 2-2. Test data obtained from each of the gas-gun tests.

Test no.	Firing pressure (psi)	Impact velocity (fps)	Pen. length[a] (ft)	Impact angle (deg) Alpha	Alpha-1	Beta	Rest angle (deg) Alpha-2
1	1700	698	5.7	75	56	19	55
2	2840	864	7.1	72	57	15	72
3	3328	900	8.3	75	75	0	(2)
4	3485	900	12.2	81	81	0	73

(a) These measured values are within 2% to 3% of the values obtained by integrating the acceleration record.

(b) 85° in plane-of-impact angle, 82° in out-of-plane direction.

2.4 Site Penetrability Profiles

The penetrability (*S*-number) is a constant based on soil and rock properties averaged over the penetration distance of a specially instrumented projectile. The *S*-number reflects the hardness of the geological materials under the dynamic loading of a penetrator. The penetrability constant was first introduced by Young in 1967 (Ref. 8) as a measure of earth penetration using an experimental data base. Young developed empirical equations to calculate the penetration depth in natural earth material and to estimate the average and peak axial deceleration of the penetrator (Ref. 9). The depth prediction capability was refined to predict penetration in the layered system by earth penetrations of various configurations (Ref. 10).

The analytical methods described by Young in 1988 (Ref. 11) were used for all data analyses for these tests. The penetrability profiles for each test were determined by

an iterative method. The *S*-numbers and layer thickness were estimated, and the deceleration-depth profiles were calculated. Then the profiles were adjusted until the calculated deceleration profiles matched the profiles measured by the accelerometers. Table 2-3 shows the *S*-number profile for each test. The average or typical *S*-number for the site was determined based on all of these *S*-number profiles. The *S*-number for the soil is 3.4 ± 0.3; for the rock, the *S*-number is 2.5 ± 0.5. This variability is reasonable in hilly terrain and a test area of this size.

Table 2-3. Target penetrability profiles.

Site no.	Layer	Material	Thickness (ft)	Average g	S-no.
1	1	Soil	1.0	630	3.75
	2	Rock	3.0	1990	2.0
	3	Rock	-	1080	2.4
2	1	Rock	5.5	1900	2.4
	2	Rock	-	1050	2.6
3	1	Rock	1.5	2270	1.9
	2	Rock	4.5	1400	2.9
	3	Rock	-	1280	2.3
4	1	Soil	4.0	870	3.4
	2	Rock	2.5	1500	3.0
	3	Soil	2.0	840	>3.0
	4	Rock	-	1190	3.0

3. MODELING FOR THE PENETRATOR AND THE TARGET

The structure and target models for the penetrator-impact finite element calculations are described in this section. We had two primary goals in developing the structural and material models. The first was to reproduce as closely as possible the response of the gas-gun penetrator tests at the PSA Flight 1771 site so that we could develop a soil-rock model for the site that might be used in other structural impact analyses. The second goal was to develop a methodology for the PSA Flight 1771 soil-rock model for impact analyses that can be used for other soils or rocks for similar impact analyses.

3.1 Penetrator Model

The finite element model of the penetrator is shown in Fig. 3-1a. The model has the dimensions specified in Fig. 2-2. It was necessary for our calculations that the model have an elliptical nose to approximate the actual conical shape of the penetrator nose. (The problem crashed without this approximation.) The penetrator has symmetry boundary conditions along the center line, and it is modeled with a slideline along the surface in contact with the ground. The penetrator is modeled with the properties of mild steel, with a density adjusted to give the correct total mass (since the actual penetrator is partially hollow in order to allow for instrumentation).

3.2 Finite Element Model Combined for Penetrator and Target System

The combined penetrator and soil-rock target model is shown in Figs. 3-1b and 3-1c. The target is modeled as a semi-infinite layered half-space, with the boundary far enough away from the point of impact so that a shear wave is not capable of making a round trip from the impact location to the boundary and back before the calculation is complete. According to the data from Test No. 2 described in Section 2.2, the geotechnical properties of the upper layer of 5.5 ft thick are slightly different from those of the halfspace. Therefore, the model parameters for the elements in this layer are slightly different from those of the bottom layer. The constitutive properties for the target model will be discussed in Section 4.

The target is modeled with a slideline with void option along the center line, so that the action of the penetrator is to push the soil aside instead of merely crushing it. This method was developed by Rosinsky and is discussed in Ref. 12. The penetrator and target are separated by a slideline, with a coefficient of friction of 0.08. All of the runs made give an initial velocity to the penetrator while the target remains initially fixed.

3.3 Target Model

To analyze the response of geological materials to penetrator impact, one must characterize the geological materials. Characterization of the site material has been accomplished through (1) extensive field explorations and measurements and

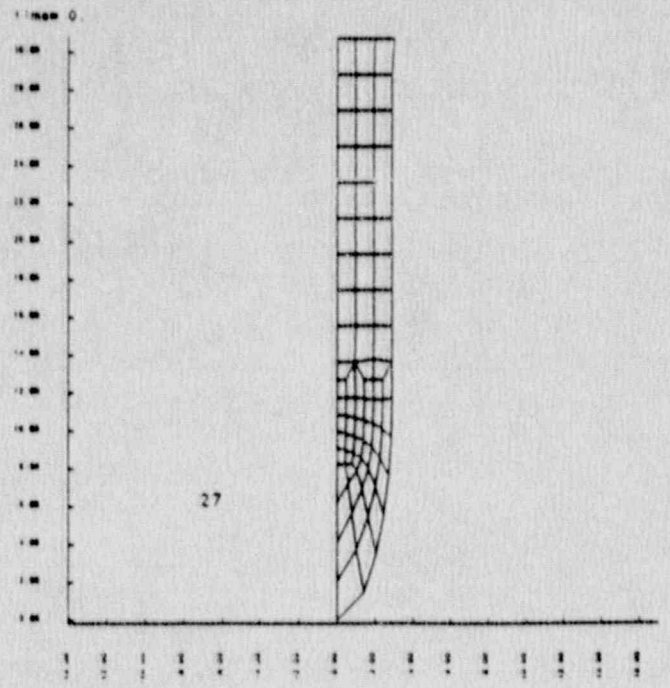

Figure 3-1a. Finite element model for the penetrator.

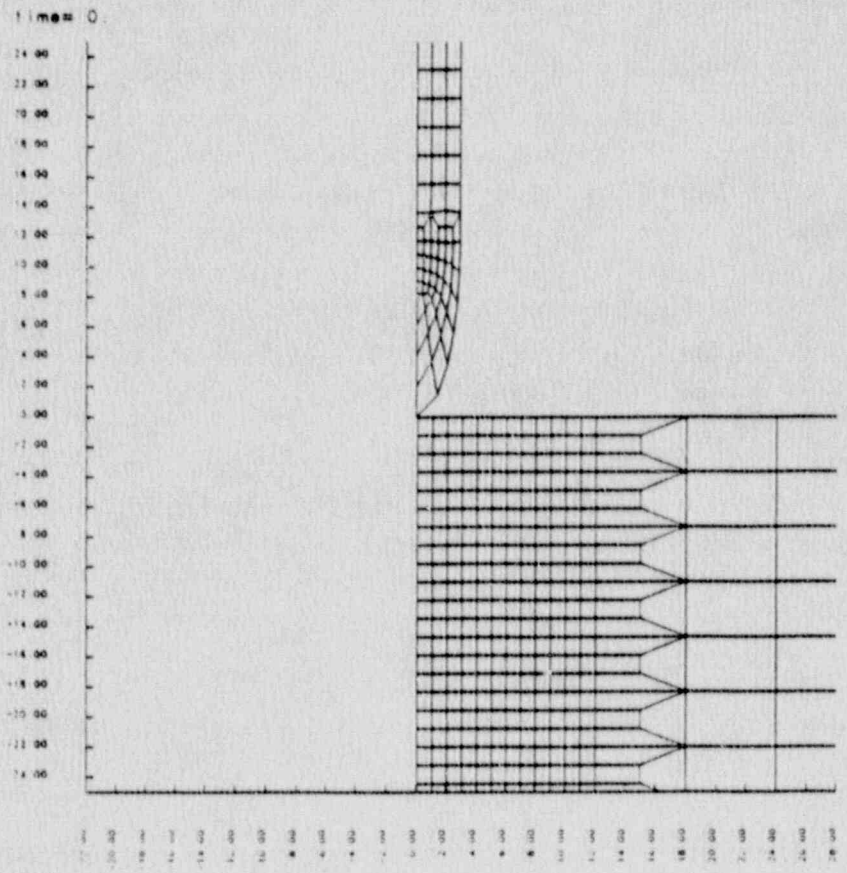

Figure 3-1b. Detailed model for the penetrator tip and adjacent soil elements at time = 0.

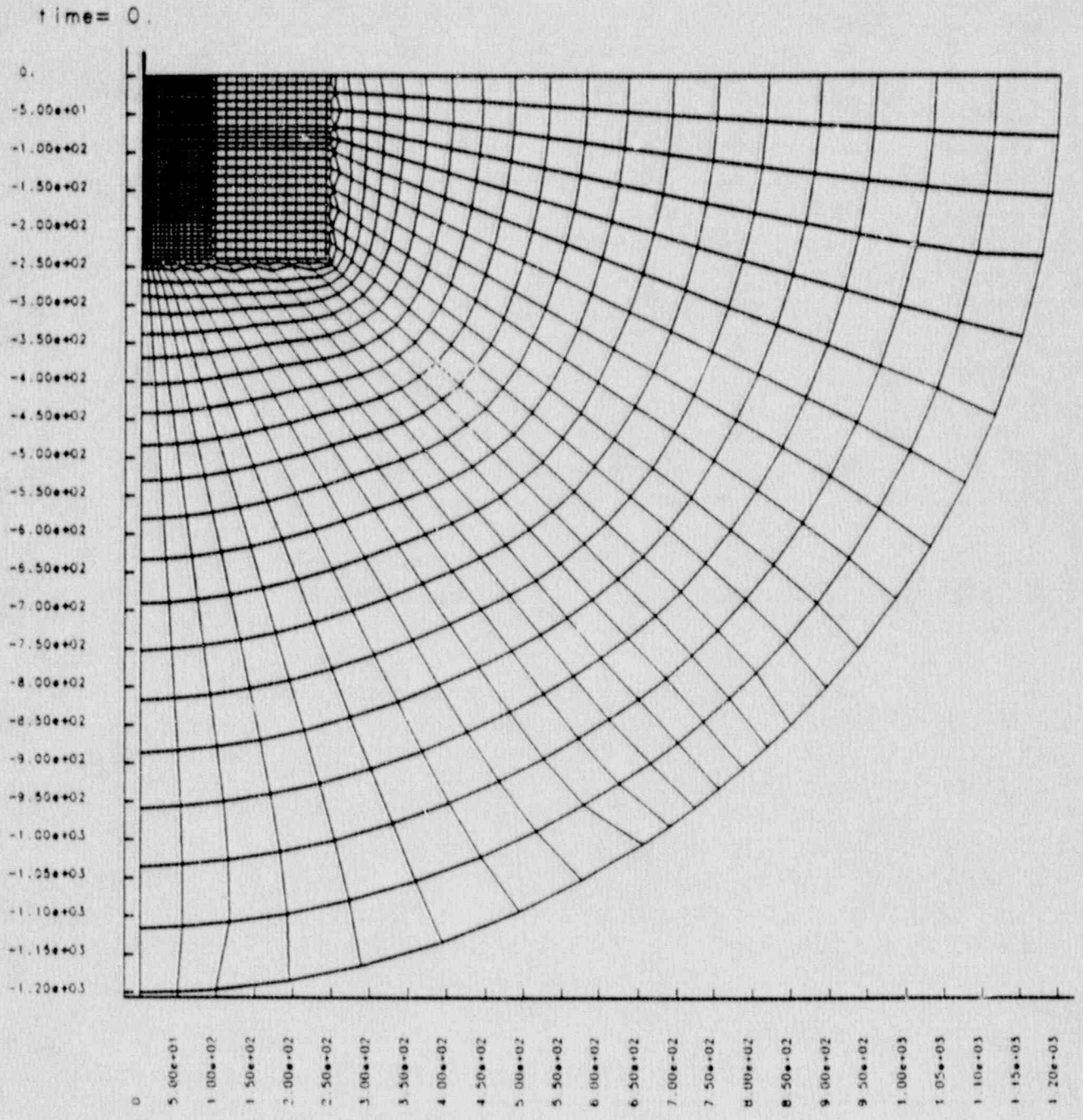

Figure 3-1c. Finite element model for the penetrator-target system.

(2) laboratory tests on soils/rock samples obtained from the site. The geological properties measured through the field and laboratory tests provide both the data base for development of constitutive models and the parameters necessary for finite-element impact analysis.

Currently, a total of 28 material models are implemented in the DYNA family of computer codes. These models can be used in a wide range of applications. Among the 28 implemented models, there are 3 models designed for the constitutive modeling of geological materials. These models are: (1) model 5 for the soil and crushable foam model; (2) model 16 for the pseudo-TENSOR concrete/geological model; and (3) model 25 for the inviscid two-invariant geologic cap model.

Model 5 (the soil and crushable foam model) is an elasto-plastic type of constitutive model originally developed by R. D. Krieg (Ref. 13) for cellular concrete. The model provides a very simple yet useful constitutive relationship for concrete and geological materials. The yield surface description consists of a surface of revolution with a plane end cap. The plane cap, normal to the hydrostat in principal-stress space, is movable due to volumetric work-hardening. Plasticity is handled in two parts: volumetric and deviatoric.

Model 16 (the Pseudo-TENSOR concrete/geologic model) was developed by S. J. Sackett (Ref. 14). This material model is developed from model 10 (DYNA isotropic-elastic-plastic-hydrodynamic model) by incorporating the option of a constant Poisson ratio material, rate effects, and an improved treatment of spall and fracture. In addition, these factors are considered: (1) reinforcement for concrete materials and (2) loading-rate sensitivity for both the principal material as well as the reinforcement material. Additional features are a damage scaling-factor and a pressure-hardening coefficient.

Model 25 is a two-invariant inviscid cap model developed by J. C. Simo, et al. (Ref. 15). The yield surface and the cap have curved shapes in stress-invariant space. The revised algorithm for the inviscid cap model has two important features: (1) exact satisfaction of algorithmic normality and consistency on the failure envelope and (2) correct treatment of the singular cone at the corner. Eleven model parameters are required.

Model 5 was selected for the present study because of its simplicity in comparison with the other two models and because of the great uncertainty in geotechnical properties of the site.

3.3.1 Constitutive Description

Concrete and most geological materials (such as rocks) subjected to tensile and compressive loads behave linearly in an elastic manner at small strains. However, as the strain becomes larger, nonlinear stress-strain behavior and permanent

deformation are developed. Permanent deformation is associated with the collapse of cells. The failure of the cells in compression is accomplished by the development of cohesive strength so that a finite shear strength remains while cells are being crushed, and this shear strength grows as the pressure increases. As shown in Fig. 3-2a, Krieg modeled this type of behavior (Model 5) with a yield surface in the principal stress space. The yield surface is a surface of revolution centered on the hydrostat. The yield surface increases in radius with increasing pressure. The shape of the yield-surface curve depends on the type of material. Although the yield surface for most geological material—based on most experimental data—appears to be a cone-shape or a paraboloid, a more general quadratic form of revolution with a plane cap on the normally open end was used in the development. The yield surface can be expressed as:

$$\phi = (p-h)(p-f)[J_2 - (a_0 + a_1 p + a_2 p^2)] = 0 \qquad (1)$$

where *h* is a constant for the tensile cut-off and *f* is a function of the volumetric strain as shown in Fig. 3-2b. This curve defines the relationship between the mean stresses and the volumetric strain for the material.

a_0, a_1 and a_2 are yield function constants. J_2 and p are stress invariant.

$$J_2 = \frac{1}{2} S_{ij} S_{ij}$$

where S_{ij} are deviatoric stresses. To simplify later description, we denote S for S_{ij}. The stress deviator is defined as:

$$S_{ij} = \sigma_{ij} - p\,\delta_{ij}$$

and

$$p = (\sigma_{11} + \sigma_{22} + \sigma_{33})/3$$

in which σ_{11}, σ_{22}, and σ_{33} are normal stresses and δ_{ij} is the Kronecker delta.

To ensure that the stress state is inside the yield surface, the first condition is $p \geq h$ so that the tensile fracture does not occur. The yield function can be kept in the form stated in Eq. (1). However, the theory is easier to explain and solve if two functions are defined—one function, ϕ_s, describing the quadratic surface, and the other, ϕ_p, describing a plane which is normal to the hydrostat; i.e.,

$$\phi_s = J_2 - (a_0 + a_1 p + a_2 p^2) \qquad (2)$$

and

$$\phi_p = p - f \qquad (3)$$

The two yield functions, ϕ_s and ϕ_p, govern, respectively, the deviatoric and the volumetric plasticity behaviors. The plasticity theories for volumetric and deviatoric parts were taken to be completely independent. The volumetric plasticity occurs if

$$\phi_p = 0 \text{ (or } p = f)$$

and

$$\dot{\phi}_p = 0 \text{ (or } \dot{p} = \dot{f}).$$

The response is elastic if $\phi_p < 0$ (or $p < f$), then

$$p - p(t_u) = -3K_e[\varepsilon_v(t) - \varepsilon_v(t_u)] \tag{4}$$

or

$$\dot{p} = -3K_e\,\dot{\varepsilon}_v \tag{5}$$

where t_u is the most recent time that the above condition was met and K_e is the elastic bulk modulus of the material. In addition, ε_v and $\dot{\varepsilon}_v$ are the volumetric strain and the strain-rate, respectively.

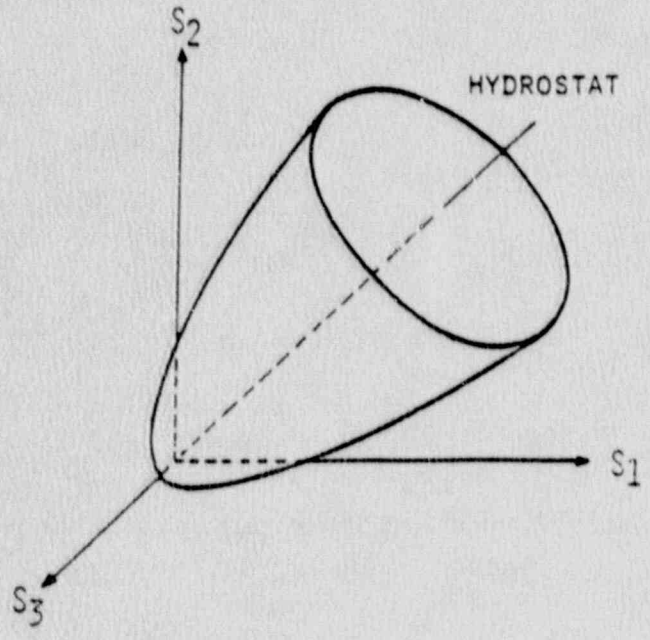

Figure 3-2a. Yield surface in principal stress space.

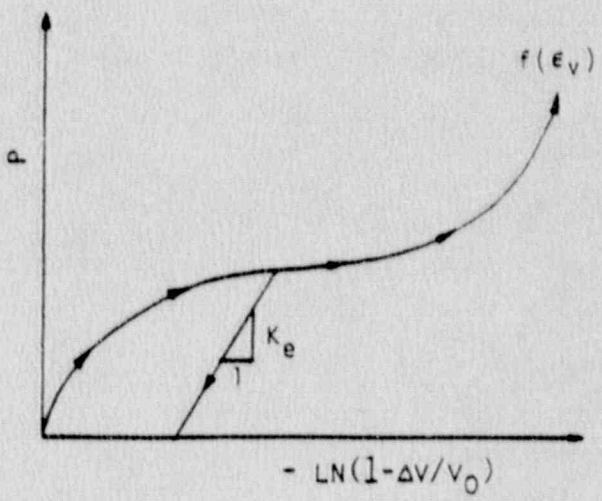

Figure 3-2b. Pressure versus volumetric strain relationship.

The deviatoric part follows the conventional plasticity theory. If $\phi_s < 0$ (or $\phi_s = 0$) and $\dot{\phi}_s < 0$, the material is assumed to behave elastically in the deviatoric mode, i.e.,

$$S = 2 G e_e \tag{6}$$

where G is the elastic shear modulus and e_e is elastic strain due to deviatoric stresses.

If the yield surface is reached and loading is taking place, a deviatoric plasticity process must be described. The plastic strain is obtained from the decomposition of the total deviatoric strain, e; i.e.,

$$e_p = e - e_e. \tag{7}$$

The plastic strain is assumed to lie in a direction normal to the yield surface. The deviatoric stress rate can be shown as follows:

$$\dot{S} = 2 G \dot{e} - \left[\frac{2 G S \cdot \dot{e} - (a_1 + 2 a_2 p)\dot{p}}{S \cdot S}\right] S \tag{8}$$

Assuming the strain-rate is constant throughout the time step, Eq. (8) can be integrated exactly so that the final stress state lies on the yield surface. The detail of the derivation and the exact integration can be found in Ref. 13.

The deviatoric stress rate depends on both the deviatoric strain-rate and the pressure rate. The deviatoric process is partially elastic in order to allow for the expanding deviatoric yield surface. The movement along the deviatoric yield surface is not accompanied by permanent volume change. Permanent volume change only occurs during the volumetric plasticity. This behavior is accomplished by making the deviatoric plastic strain-rate vector normal to the yield surface in the deviatoric subspace.

3.3.2 Model Parameter Requirement and Evaluation

As described in the previous section, the Krieg model (Model 5) can be characterized by six parameters (G, K_e, a_0, a_1, a_2, and h) and a complete definition of the function, f, for pressure versus volumetric strain relationships. The merit of this set of parameters is that each has clear physical and mechanical meaning and all parameters can be characterized using conventional laboratory test results. In this study, isotropic pressure-volume tests were conducted on core samples taken from the crash site to determine the f function and K_0. These values are input to the DYNA code in tabulated formats. Uniaxial unconfined compression tests and triaxial compression tests (at different confining pressures) were conducted to determine the Young's modulus, Poisson's ratio, and yield stresses. After the yield

stress function is defined, the yield function constants, a_0, a_1, and a_2, may be determined by one of the methods described in the following paragraphs.

3.3.2.1 Cone-shape yield surface

When the plot of deviatoric stress data versus mean effective stress shows a linear relationship (Fig. 3-3a), it is easy to find yield function constants by fitting the quadratic equation to the straight line (i.e., the cone-shape yield surface). The constants of the yield function can be defined as:

$$a_0 = 1/3\ \tau_0^2$$

$$a_1 = 2/3\ \mu\ \tau_0$$

$$a_2 = 1/3\ \mu^2$$

in which τ_0 is the cohesive deviatoric strength and μ is the slope of the yield surface. This type of model has been used in penetration analysis for the EPW program (Ref. 16). A correlation summary of model parameters and conventional soil-mechanics properties is shown in Table 3-1 (Ref. 17).

Table 3-1. Correlation between model 5 parameters and conventional soil properties.

Parameters for (Krieg) model 5	Correlation	Soil parameters
G = shear modulus	Need a proper estimate of confining pressure	G is shear modulus, pressure-dependent
K_e = unloading bulk modulus	Need a proper estimate of mean pressure change	K is bulk modulus, pressure-dependent
τ_0 = cohesive strength	$\tau_0 = (6c \cos \Phi)/(3 - \sin \Phi)$	c is cohesion
μ = slope of σ_y-vs-p curve	$\mu = (6 \sin \Phi)/(3 - \sin \Phi)$	Φ = friction angle in Mohr-Coulomb failure envelope
p_t = pressure cutoff for tensile fracture		

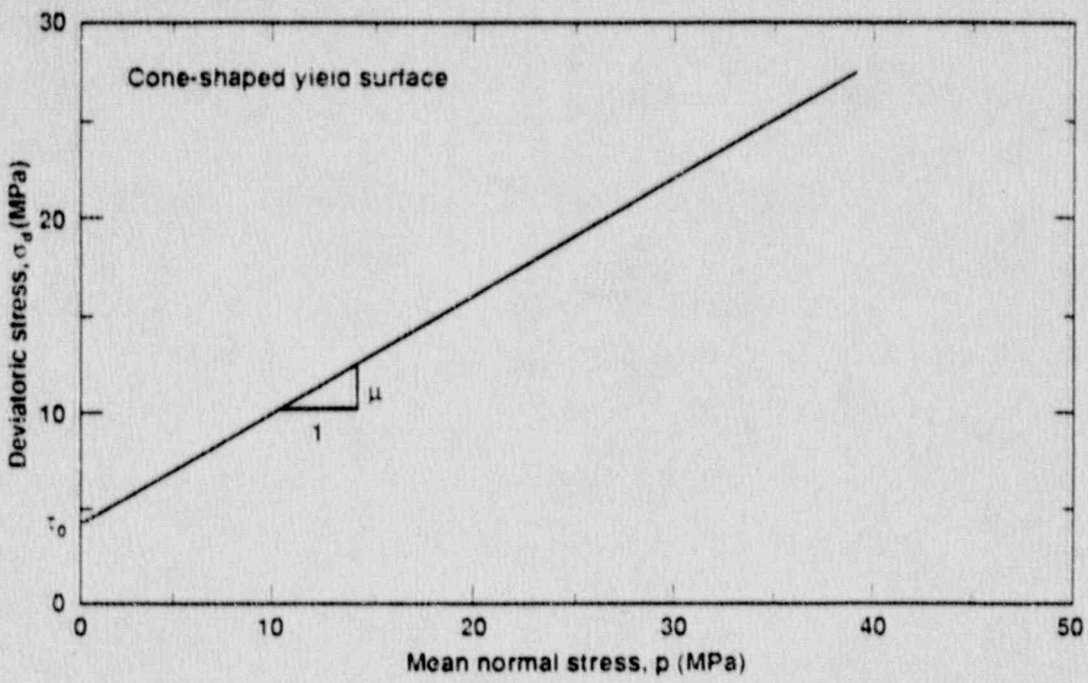

Figure 3-3a. Idealized cone-shape yield surface.

3.3.2.2 Paraboloid-shape yield surface

Strength data of geological materials may also be approximated by a parabola, as shown in Fig. 3-3b. The deviatoric stress, σ_d, versus the pressure, p, for this type may be written as:

$$\sigma_d^2 = c_1 + c_2\, p. \tag{9}$$

Fitting two given points $(p_0, 0)$ and (p_1, σ_{d1}) to find c_1 and c_2 as:

$$c_1 = -\, p\sigma_{d1}^2/(p_1 - p_0)$$

and

$$c_2 = \sigma_{d1}^2/(p_1 - p_0).$$

Comparing the parabola and the quadratic form, the constants for the yield function can be defined as:

$$a_0 = c_1/3$$
$$a_1 = c_2/3$$
$$a_2 = 0 .$$

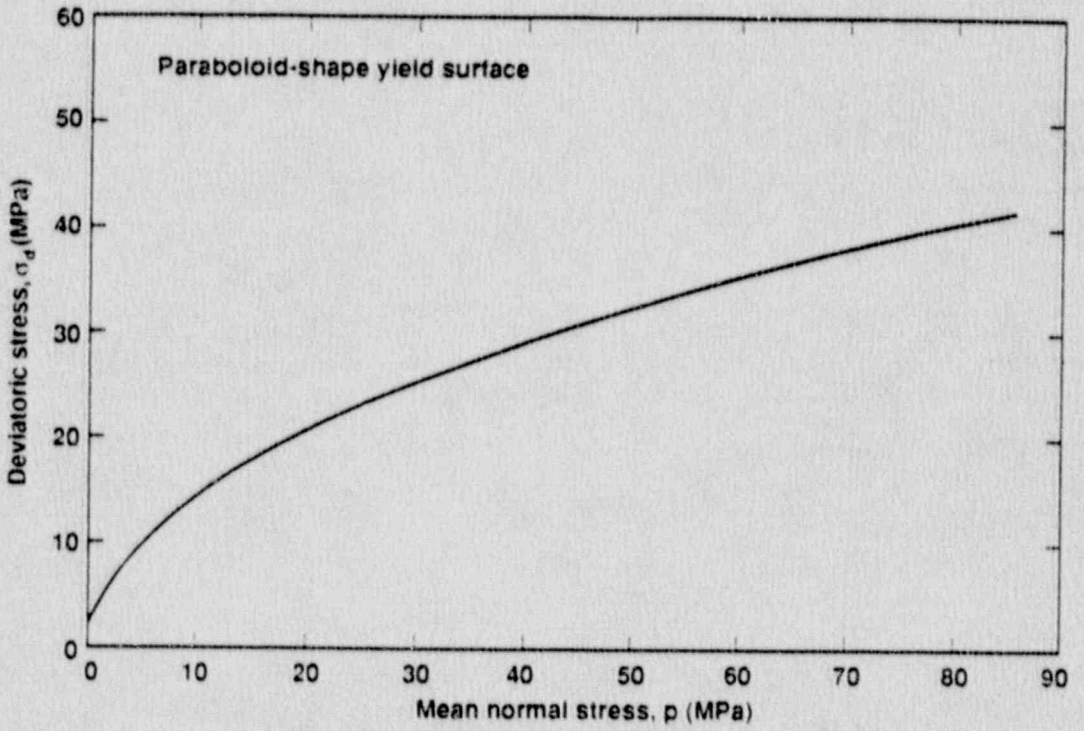

Figure 3-3b. Idealized paraboloid-shape yield surface.

3.3.2.3 Quadratic-shape yield surface

To find the best quadratic polynomial to fit a data set of m experimental points , we employed the least-squares minimization of adjustments to the J_2 values as described in Section 3.3.1. The yield surface has the form (for simplicity, we here denote J for J_2):

$$J = a_0 + a_1 p + a_2 p^2. \qquad (10)$$

The discrepancy between the value of the quadratic polynomial at the point k and the actual value is given by e_k, where:

$$a_0 + a_1 p_k + a_2 p_k^2 = J_k + e_k. \qquad (11)$$

The complete set of m equations of this type may be written in the matrix form of:

$$A\,x = B + e \tag{12}$$

where, A is an m-by-3 matrix of p; B and e are column vectors of order m containing m stress invariant J_2 and its error e; and x is a vector of the coefficient of the quadratic polynomial $(a_0, a_1, a_2)^T$. Through the minimization procedure of the least-squares method, it can be shown that the equation can be written in the final matrix form as:

$$A^T W A X = A^T W B \tag{13}$$

where W is a diagonal matrix of the weighting factors. If it is assumed that all experimental data points have equal weighting factor, then the solution of X can be easily found as:

$$X = A^T B. \tag{14}$$

A computer program can be developed easily to solve the system equation. However, the CAL 78 developed by Wilson (Ref. 18) has been used in this study. Because a total of 16 data points are relevant to develop the model, we decided to use the least-squares method to find the constants of yield functions. A typical fitting curve is shown in Fig. 3-4, together with the actual data points.

All required parameters were determined from the data obtained from both laboratory tests of core samples and field measurements at the crash site. The following section summarizes the geotechnical characteristics and properties at the site.

3.3.3 Geotechnical Characteristics and Properties at the Crash Site

The site characteristics and geotechnical properties at the PSA Flight 1771 crash site were studied on the basis of data from extensive field investigations and measurements, as well as laboratory tests. Field investigations consisted of topography surveys, exploratory borings, seismic refraction measurements, and dynamic penetration tests. Laboratory tests measured the basic engineering properties, compressibility characteristics, and the stress-strain behaviors of the soil/rock samples. The crash site information and test data for the site geological materials are being utilized in the study of dynamic impact-crash analyses.

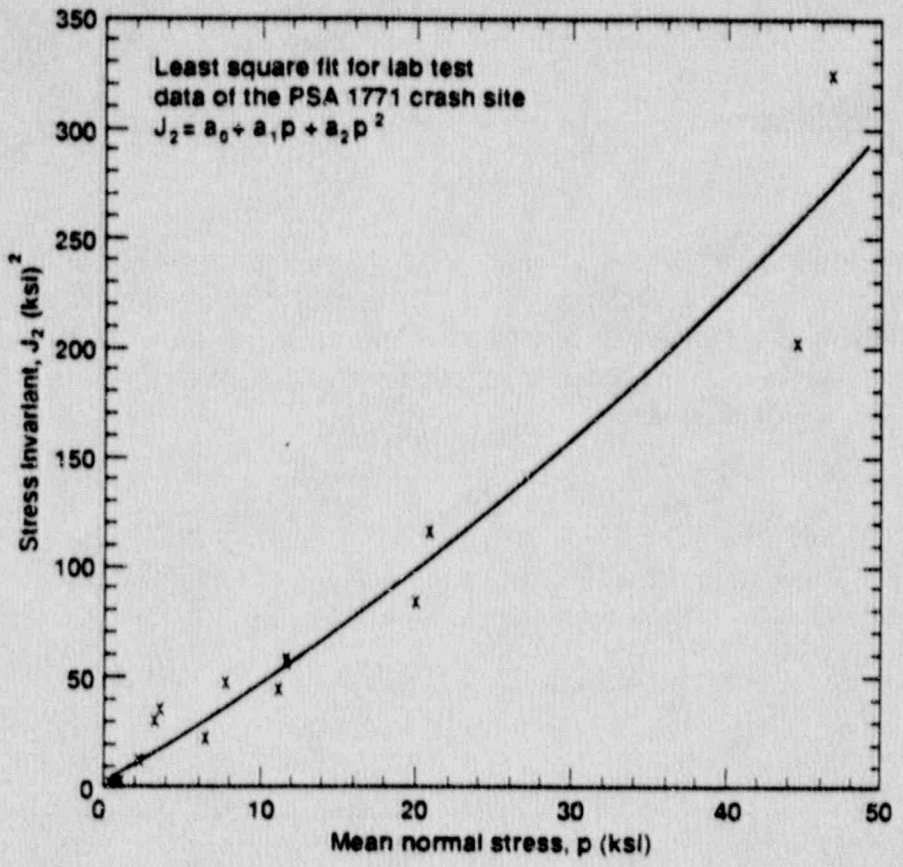

Figure 3-4. **The least-squares minimization of adjustments to the J_2 values obtained from Laboratory tests.**

3.3.3.1 Site characteristics and stratigraphic conditions

Detailed engineering geologic evaluation of the site was reported by D. W. Carpenter, et al. (Ref. 7). The impact point is located near the top of a hillside at an approximate elevation of 403 m (1322 ft) above mean sea level. The slope gradients of the hill vary from 20% to 40% in the vicinity of the impact point.

Prior to the dynamic penetration tests, subsurface geological conditions in the crash site vicinity were investigated by drilling and sampling five exploratory holes. The locations of these holes are shown in Fig. 2-1. A total of five holes were drilled. Hole DH-1 was drilled within the limit of the crash impact crater: the remaining four holes—DH-2 through DH-5—were drilled outside the crater boundary in an effort to characterize the pre-crash condition of the materials. The depth of the holes ranges from 15 m

to 21 m (49 ft to 70 ft). Drilling in each of the holes encountered a veneer of colluvial soil deposits and decomposed rocks overlying fractured rocks, grading from intensely weathered to unweathered. Drive samples of the soil materials and core samples of the rock were obtained for laboratory testing.

The geological cross sections through the site are illustrated in Fig. 3-5. Within the vicinity of the crash impact location, but outside the crater, colluvial deposits were encountered at the ground surface with thicknesses varying from 0.2 m to 0.6 m (0.5 to 2 ft). These deposits consisted variously of sandy silt, clayey silt, and silty clay. The sedimentary rocks of the late Mesozoic Toro Formation consist primarily of interbedded clay shales and silty sandstones, with occasional seams of siltstone and claystone. The upper portion of the rock formation—immediately underlying the colluvium—has been decomposed through weathering to a residual soil condition. Although these residual soils were formed from rock decomposed in place, they have properties and behavior characteristics of soil rather than rock. The residual soils consist of lean silty, sandy clay decomposed from the shale, and silty sand decomposed from the sandstone. The remainder of the rock formation graded with depth from intensely weathered to unweathered. These rocks are a portion of the Great Valley Sequence. They are separated from the marine sedimentary rock present in the vicinity of the crash site by a branch of the Oceanic Fault zone.

As a result of past tectonic activity, rock in the vicinity of the crash site has been intensely fractured and sheared. Matrix materials of the shale beds of the Toro Formation are intensely sheared and penetratively deformed (Ref. 7). The average value of rock quality-designation (RQD) of the intensely weathered rock is approximately 15, with a coefficient of variation (COV) of 0.9.

3.3.3.2 In-situ shear wave measurements

A seismic downhole survey was conducted to determine the overall seismic shear wave velocities in the upper 15 m (50 ft) of the site. The survey made use of an existing boring (DH-5) drilled at the site adjacent to the impact crater. The detailed procedure was reported in Appendix A of Ref. 7. The seismograms were recorded at each depth with 1.5-m (5-ft) intervals down to a depth of 15 m. The results of the survey are shown in Fig. 3-6. The average shear wave and compressional wave velocity in the upper 4.6 m (15 ft) of intensely weathered rock layers are about 610 m/s and 1320 m/s (2000 and 4000 fps), respectively. These values represent overall in-situ seismic velocities, and they are used for modeling consideration.

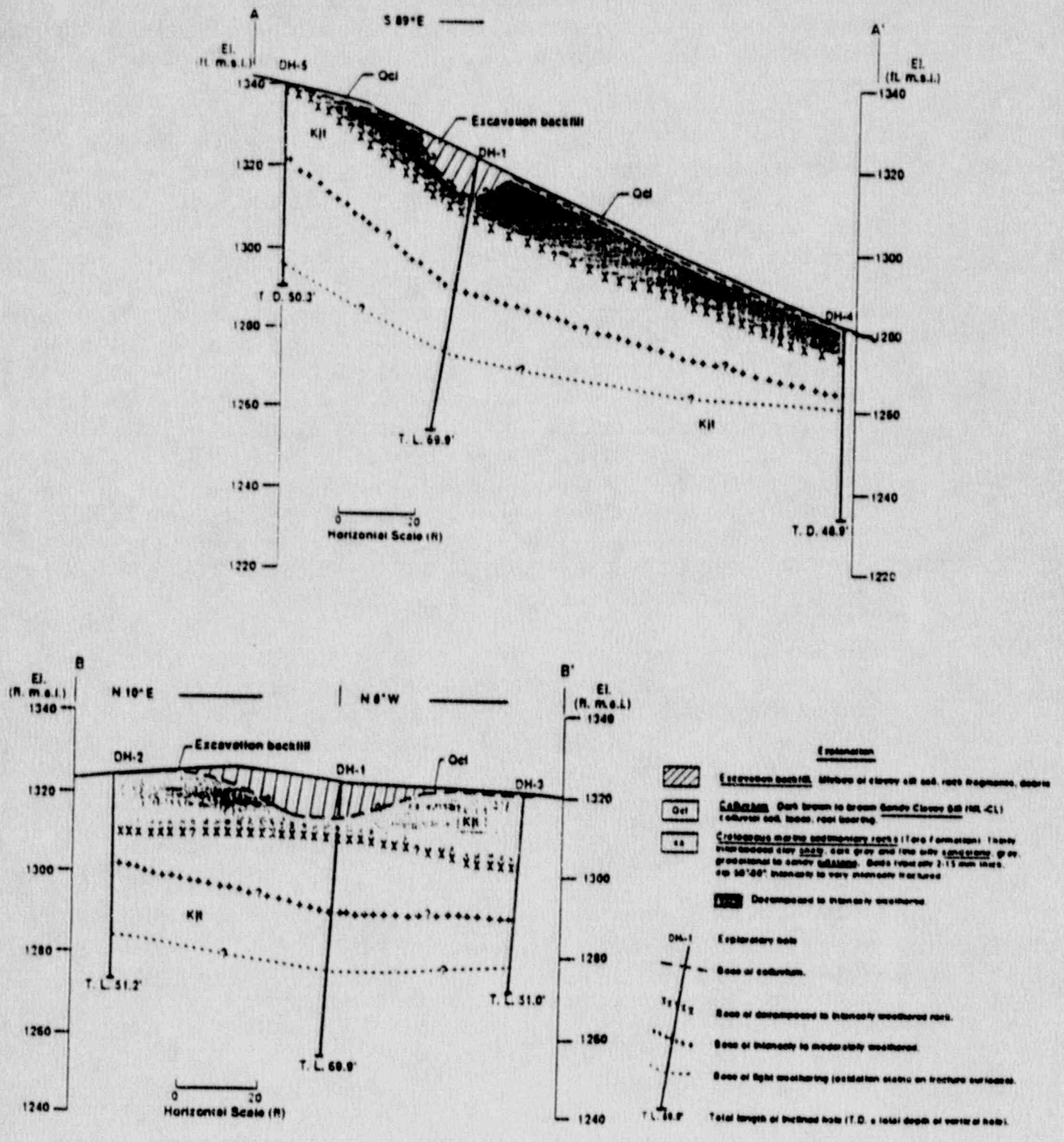

Figure 3-5. Geologic cross sections through the PSA 1771 crash site.

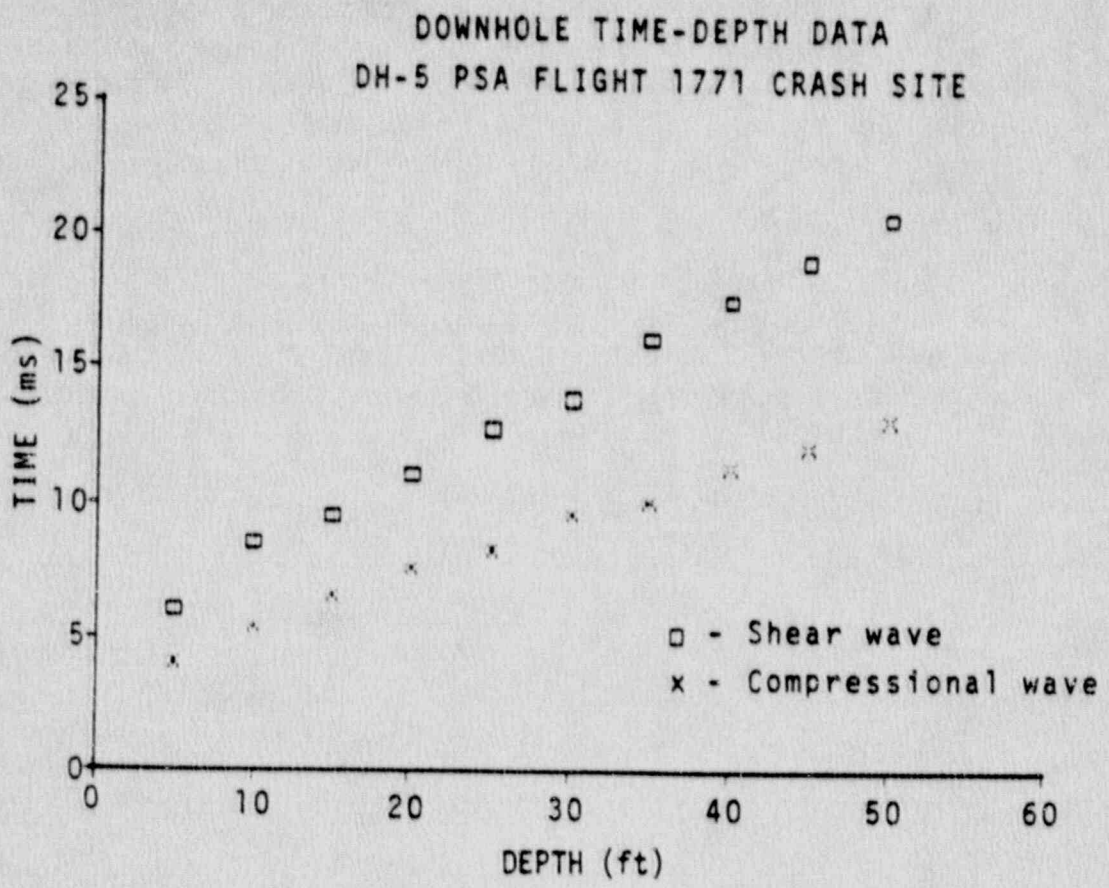

Figure 3-6. **The time-depth data obtained from geophysical downhole survey at drill hole DH5.**

3.3.3.3 Soil properties, compressibility characteristics and stress-strain behavior

The engineering properties, including compressibility characteristics and stress-strain behavior of the soils from the site, were reported by Chang, et al. (Ref. 17). During the exploration drilling, undisturbed soil samples were taken and Standard Penetration Tests (SPT) were conducted. The SPT consists of driving the standard split-spoon samples 0.5 m (18 in.) into the soil and counting the blows required to drive the sampler the last 0.3 m (12 in.). The blows are delivered by a 64-kg (140-lb) hammer falling 1 m (39 in.) onto the drill rod to which the spoon is attached. This is the simplest method for

obtaining information concerning the degree of compactness of the soil in situ. The higher blow-count number or SPT indicates ground that is relatively more compact. The average SPT number for the residual soils at the crash site is about 25. The average value of bulk density, moisture content, and porosity and their coefficient(s) of variations are shown in Table 3-2.

The liquid Atterberg limit and plasticity index are basic soil property descriptions commonly used in the geotechnical engineering field. Atterberg limits are the limiting values of water contents of a clay-water mixture that define physical states of the clay. Above the liquid limit (LL),

Table 3-2. Soil properties at the PSA Flight 1771 crash site.

Properties or parameters	Best estimate or average	Coefficient of variation
Bulk density (kg/m^3)	2090	0.1
Moisture content (%)	16.2	0.3
Porosity (%)	32.0	0.2
Unloading bulk modulus (MPa) (vary with mean effective stress)	130.0	
Ultimate strength (MPa) (at 1.5 m depth from surface)	0.73	
Shear modulus (MPa) (defined at 50% stress level)	11.6	
Poisson's ratio	0.45	
Liquid Atterberg limit, LL (%)	34 ± 2	
Plasticity index, PI (%)	11 ± 4	
Penetrability constant (S-number)	3.4 ± 0.3	

the soil-water mixture is a suspension. Below the liquid limit and above the plastic limit (PL), the soil-water mixture is said to be in a plastic state. The limiting water content serves as an index of properties useful in the classification of clays. The plasticity Index (PI) is the numerical difference between LL and PL; PI is an indication of the range of water content within which a soil possesses plasticity. The LL and PL values have been used to classify the type of clay soils. The LL of 34 and PI of 11 for the crash site indicate clay soils of inorganic clays of low to medium plasticity.

The values of unloading bulk modulus vary with the mean effective stress level and the amount of unloading. The range of values obtained from the test data is 2.1×10^5 to 0.5×10^5 kPa (0.3×10^5 to 0.07×10^5 psi) with an average of 1.3×10^5 kPa (0.18×10^5 psi). Secant shear moduli of the site soil vary with stress level as shown in Fig. 3-10. Values of shear modulus are defined at 50% stress level. The normalized shear modulus obtained from the undrained test data indicated that an average of 11,600 kPa (16800 psi) may be expected for a slow rate of loading and 16,750 kPa (2430 psi) for impact loading.

The compressibility characteristics of the crash site soils were investigated by laboratory one-dimensional consolidation tests and triaxial compressional tests. Significant differences of compressibility appear to be represented among soils at the site, with a ratio of 2 between volumetric strains for the near-surface colluvium and the residual soils tested from a depth of about 1.8 m (6 ft). However, there is an overall trend of decreasing compressibility with depth in the soil profile. The typical confining-pressure-versus-volumetric-strain curves from one-dimensional consolidation tests and triaxial compressional tests are shown in Figs. 3-7 and 3-8.

The strength, stress-strain, and modulus characteristics of the soils were investigated by testing relatively undisturbed specimens under unconsolidated-undrained conditions in triaxial compression. Fig. 3-9 shows the stress-strain response curve for four specimens. It is noted that three of the specimens tested (DH 3-2, 3-3, and 3-4) remained unsaturated at the beginning of shear and during shear; therefore, all the applied confining-pressure and shear-stress contributed to intergranular effective stress, and the specimen behaved in a drained fashion. The fourth specimen (DH 2-2) is interpreted to have been compressed to a saturated condition at or near its test's confining pressure, and therefore to have behaved in an undrained manner. Variation of shear modulus with applied stress level is shown in Fig. 3-10. This figure indicates a difference of response between the saturated, undrained specimen and the specimens interpreted to be "drained." It should be noted that the modulus may be on the lower side due to the disturbance of specimens. Generally, a factor of 2 to 3 is applied to compensate for sample disturbance.

3.3.3.4 Rock properties, stress-strain behavior, and compressibility characteristics

The mechanical properties of the rocks obtained from the site were reported by S. C. Blair, et al. (Ref. 19). Geotechnical properties of the rocks at the site were determined from a variety of laboratory tests and measurements on drill core and outcrop samples. Pressure-volumetric tests to determine bulk modulus

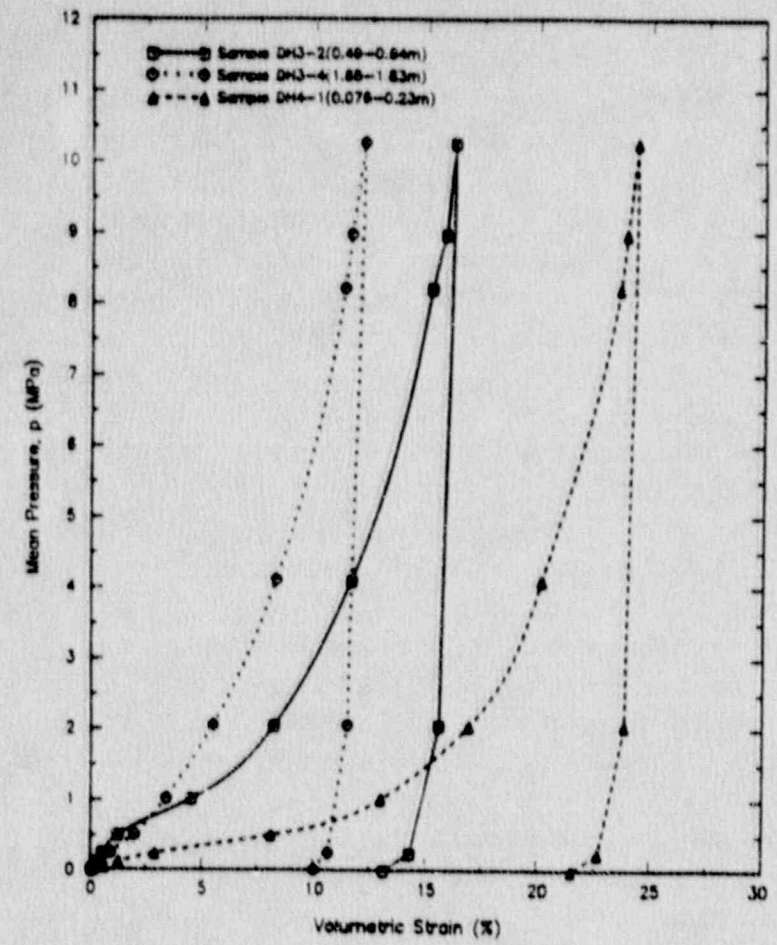

Figure 3 - 7.
One-dimensional consolidation tests of the PSA 1771 crash-site soils.

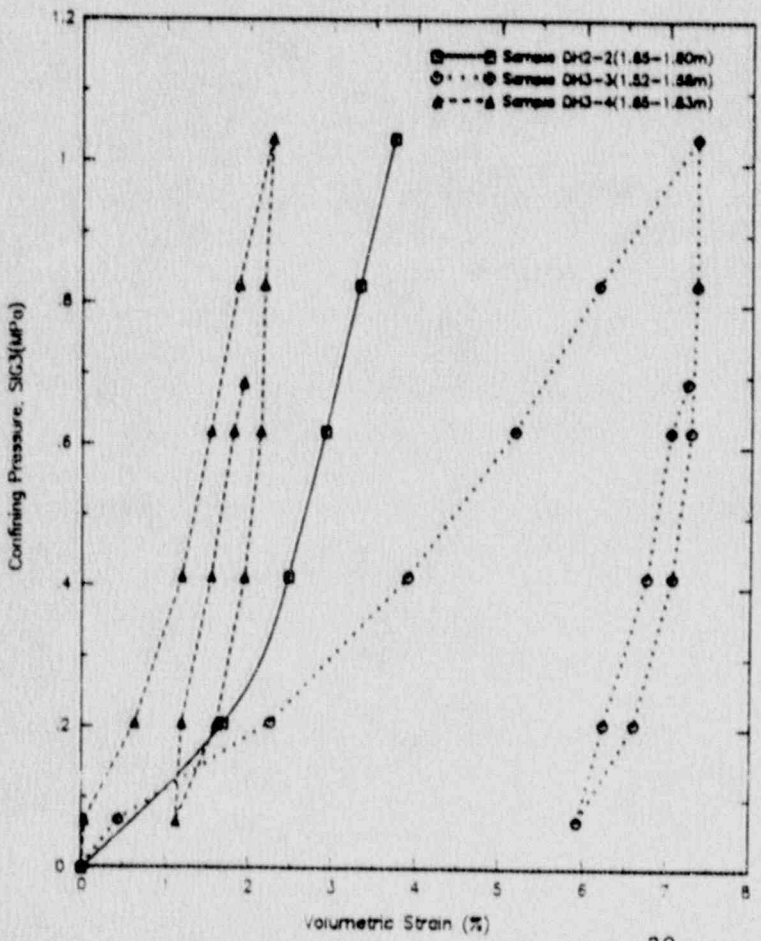

Figure 3 - 8.
Volumetric compression curves of triaxial UU tests on the PSA 1771 crash-site soils.

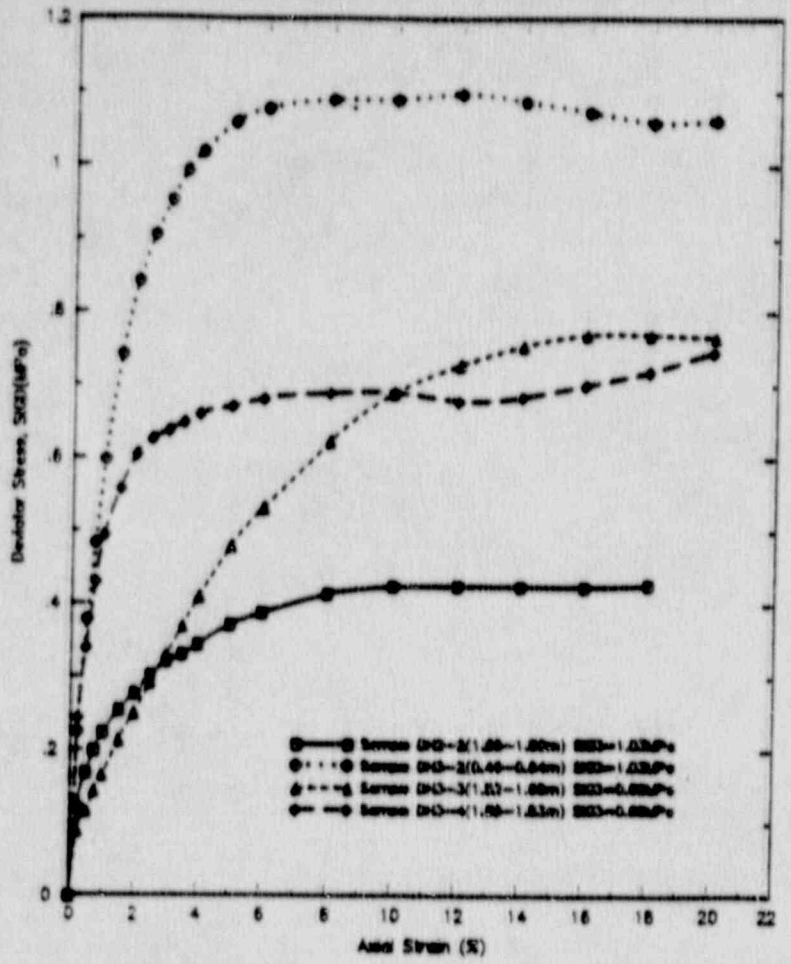

Figure 3-9. Stress-strain response curves obtained from triaxial UU tests on the PSA crash-site soils.

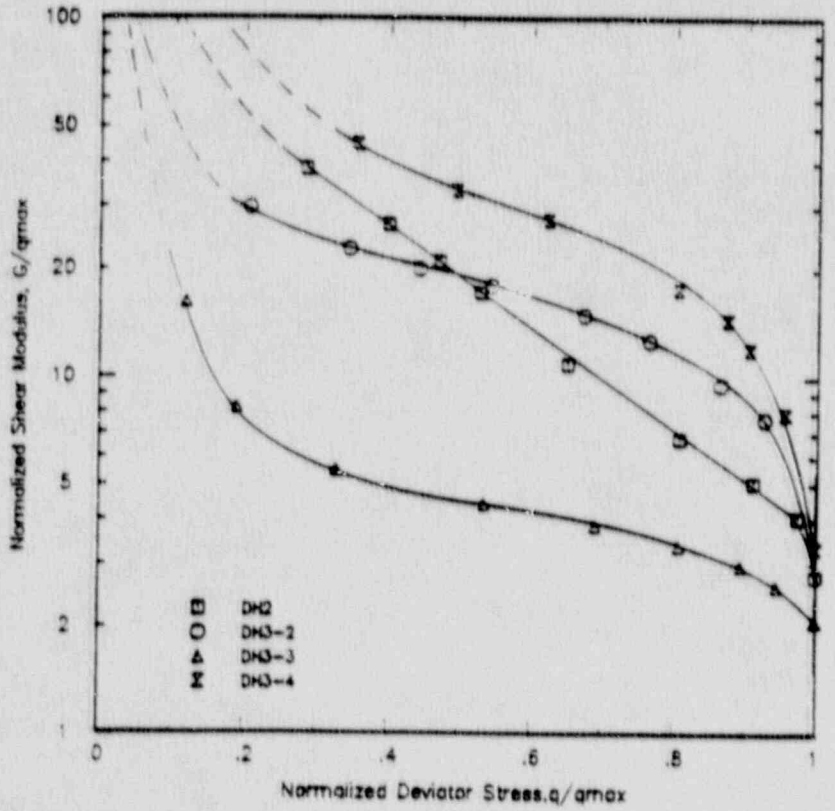

Figure 3-10. Variation of normalized shear modulus with relative deviatoric stress.

were conducted on sample sizes of 2.5- and 5.1-cm diam. and at pressures up to 480 MPa. The uniaxial compressive strength for both groups of samples was also measured. Triaxial compression tests were conducted at pressures between 25 and 500 MPa to investigate the effect of confining pressure on stress-strain behavior. As the confining pressure was elevated, the strength increased and the material response changed from brittle fracture to ductile, strain-hardening behavior. Strain-rate effect was investigated at the confining pressures of 25 and 50 MPa for strain-rates between 10^{-4} and 20/s. Ultimate strength and Young's modulus were observed to increase with increasing strain-rate. Dry densities and porosities for selected samples were also measured. Table 3-3 shows the measured properties of the average values and ranges on the coefficient of variation (COV) if sufficient data are available.

The pressure-volumetric strain curves obtained from isotropic compression tests on samples of drill core and outcrop material are shown in Fig. 3-11. The curve for the drill core sample has two distinct regions. The behavior in the first region (0-70 MPa) is controlled by closure of preexisting fissures

Table 3-3. Rock properties at the PSA Flight 1771 crash site.

Properties or parameters	Best estimate or average	Coefficient of variation
Bulk density (kg/m^3)	2370	0.1
Porosity (%)	8.0	
Unloading bulk modulus (MPa)		
First cycle (0 to 8 MPa)	2177	
Up to 4 cycles (8 to 250 MPa)	5100	
Unconfined compressive strength (MPa)		
Weathered rock	22.0	0.25
Unweathered rock	102.0	0.45
Weathered and unweathered rock	53.0	0.92
Shear modulus (MPa)		
Defined at 50% stress level		
Unconfined	1307	
Confined (25 to 250 MPa)	3396	
Poisson's ratio	0.28	
Seismic wave properties		
Shear wave velocity (m/s)	610	0.3
Compression wave velocity (m/s)	1220	0.3
Penetrability constant (S-number)	2.5 ± 0.5	

and large voids; the materials are slightly compressed in this region. In the second region—above 70 MPa—the deformation is controlled by deformation of pores and compression of grains. The rock behaves linearly in this region. The outcrop material was found less compressible than was the drill-core sample. The bulk modulus is very similar for the two samples once fractures and voids are closed. The unconfined compression tests were conducted on several samples of drill-core and outcrop materials to determine their unconfined compressive strength and Young's modulus. The unconfined compressive strength between the weathered and unweathered samples is quite different. The unconfined compressive strength was linearly increased with the sample density. Fig. 3-12 shows the typical stress-strain curves of the unconfined compression test on outcrop samples. Several samples of drill-core and outcrop material were tested in triaxial compression at three strain-rates to determine the effect of confining-pressure and strain-rate behavior. Stress-strain curves for samples of drill core tested at pressures between 25 and 500 MPa at a strain-rate of 10^{-4}/s are shown in Fig. 3-13. It is noted that the samples tested at 25 and 50 MPa behaved in a semibrittle manner, while the samples tested at pressures of 100 MPa and above displayed ductile, strain-hardening behavior, with compressive strength increasing with strain at high confining pressures.

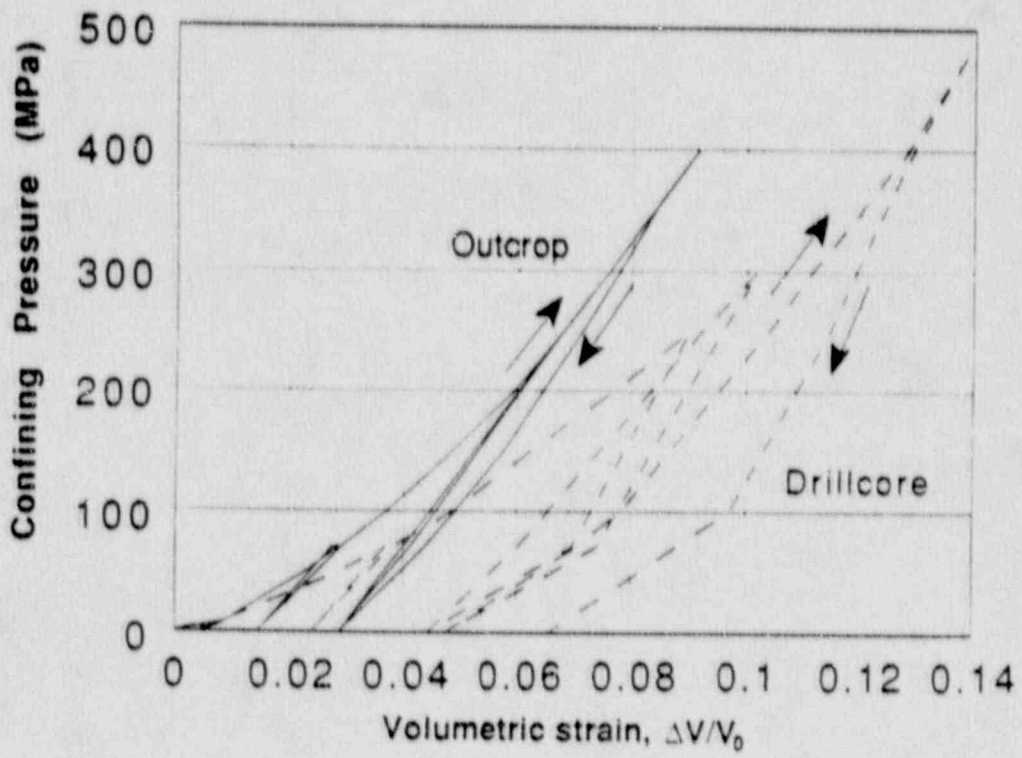

Figure 3-11. Pressure-volume behavior of rocks from drill core and outcrop samples.

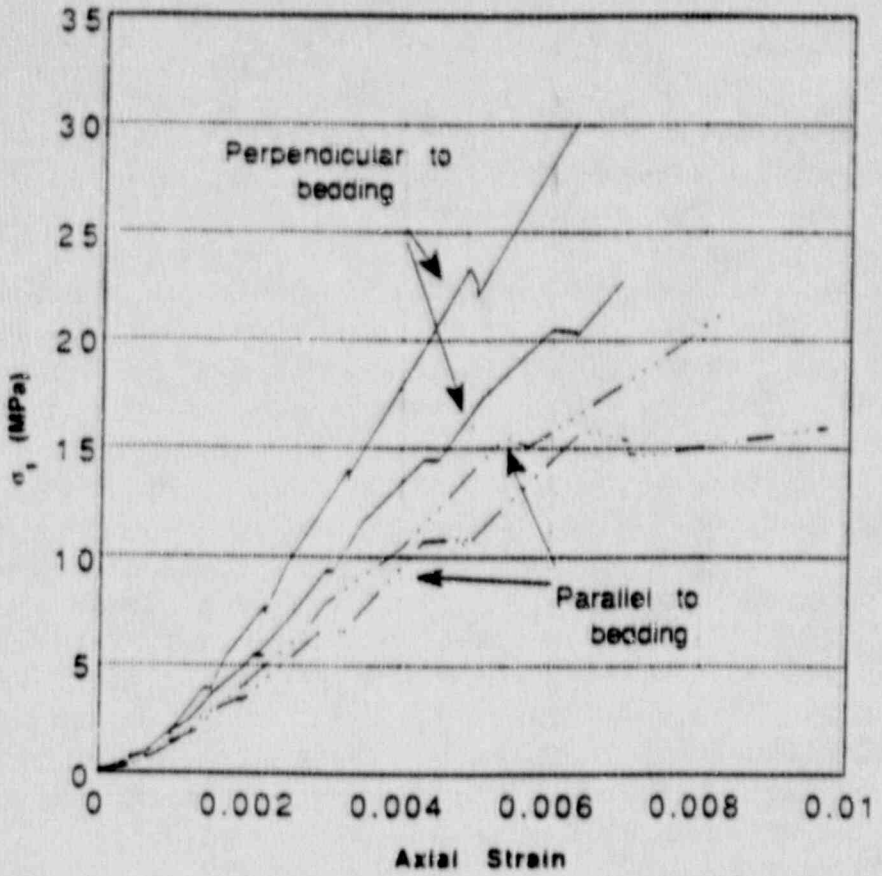

Figure 3-12. Stress-strain behavior of outcrop rock samples under confined compression tests.

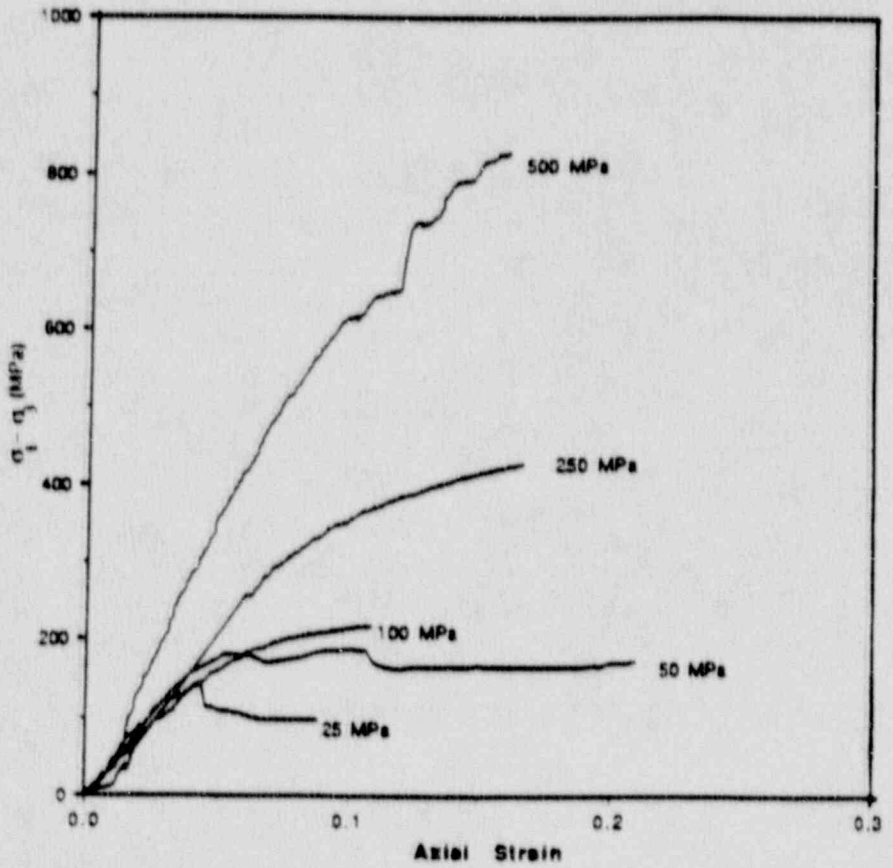

Figure 3-13. Stress-strain curves for samples of drill core tested at various confining pressures.

A suite of triaxial tests was conducted on samples from outcrop material. Strain-stress behavior of this material at confining pressures of 50, 100, and 150 MPa was plotted and compared with those of core materials tested at the same rate. Generally, the outcrop materials show a slightly stronger strength at the lower strain ranges, and they therefore have a higher Young's modulus. It was also found that, with strain-hardening, the behavior of the outcrop material is more semibrittle, while the behavior of the core material is more ductile.

The effect of tension cutoff may be important for analyzing an unfractured rock or concrete material. However, due to the intensely weathered and fractured nature of the site, the tension cutoff was set approximately to zero. The Poisson's ratio obtained from laboratory tests range from 0.25 to 0.3. Shear wave and compression wave measurements from the field gives a value of 0.33 for Poisson's ratio. We consider a value of 0.28 to be the appropriate as the overall Poisson's ratio for use in modeling.

The strengths, stress-strain behaviors, and compressibility characteristics of soils and rock are described on the basis of laboratory tests of intact specimens. However, the strength and the compressibility of most geological materials are significantly different between laboratory tests and in-situ, large-scale tests. In contrast to the laboratory tests on small intact specimens, in-situ tests cover the effect of field conditions in terms of the fracture characteristics of the rock mass. In addition, the effect of high strain-rate on the intact specimen was limited to 20/s due to the restriction of the equipment. The stress-strain behavior and modulus characteristics under high strain up to 10^4/s could be quite different. An extensive literature review was conducted to understand the scale and high-strain-rate effects and to approximately include them in models developed for impact-crash analysis.

3.3.4 Modeling Considerations

In the continuum approach of stress analysis, the material properties are always associated mathematically with the concept of infinitesimal volume. It is clear that no real-material properties can satisfy this mathematical assumption, especially geological materials. In stress analysis, the quantities such as dx, etc., mean to a mathematician lengths which decrease uniformly to zero. To an engineer, they represent small but finite dimensions for which the formality of mathematical representation remains approximately valid. "How small is small?" is an important question, and no exact general criterion of the relative smallness has been given. For a relatively uniform material such as steel, one will not hesitate to apply continuum theories for analyzing the stress-strain of the structure of a manufacturable size. The success of the analysis is often assessed and judged in comparison with results obtained experimentally.

For geological material such as soils and rock mass, the problems are of the same nature but obviously on a large scale. The soil/rock material generally consists of a granular-crystalline structure with its irregularities and heterogenetics. Furthermore, stratified and fractured rock masses exhibit their properties in dimensions varying from centimeters to more than meters. An exact calculation procedure to handle high-intensity fracture rocks—such as those at the PSA Flight 1771 crash site—is not available; however, the continuous modeling approach incorporated in the DYNA code appears to be a reasonable way to conduct this analysis. One of the most important aspects of the approach is the assessment of representative properties and parameters to be used in the constitutive models. Our development of the model parameters is based on evaluation of data obtained from laboratory tests and in-situ measurements. The nature of the geological discontinuities and fractures within the zone of influence is a significant factor that affects the determination of the strength and the compressibility of the rock mass. The best source of information that can be used to provide a reasonable estimate of the effect of these discontinuities is large-scale field-load tests. The loaded area must be sufficiently large to stress a volume of rock that contains enough discontinuities and represents the site characteristics. To perform the in-situ test to measure the field strength and deformation modulus requires heavy equipment and a longer period of time than was available. Also, due to the hilly nature of the PSA Flight 1771 crash site and the desire to minimize disturbance of the crash site a literature review to estimate the scale-fracture effect was conducted instead of pursuing field tests.

Another aspect to consider in modeling is the nature of the loading condition due to the high velocity impact. During the moments of aircraft/package impact and penetration into the soil/rock, the high-impact stress states rapidly impose increased confining stress conditions within the soil/rock mass. In response to the increased confining stress, the soil/rock density increases as a result of compression of any air in the void spaces, and intergranular effective stresses are increased accordingly. The high-velocity impact load induces shear stress in the soil/rock mass at a very high rate, with resultant shear deformation and failure response of the soil/rock in accordance with the loading-rate-compatible modulus and strength characteristics of the soil/rock. To assess the high strain-rate effect, we conducted an extensive literature review on strain-rate effects in the determination of strength and deformability of different geological materials.

3.3.4.1 Scale-fracture and strain-rate effects

We briefly summarize the results of our review on the effects of the characteristics of field condition (scale-fracture effect) and loading condition (high strain-rate effect). Detailed discussions are presented in Appendix A. It should be noted that we present more information for rock materials because the benchmark calculations presented in the report do not include soils. Detailed review and discussion on soil materials can be found in Ref. 17.

In summary, the in-situ characteristics of soils or rocks must be considered in modeling the site target. Soil materials are more easily disturbed during the process of drilling, sampling, transporting, and sample preparation. A disturbance factor of 1.5 to 2.5 may be used for the correction of strength and deformation modulus depending on the degree of disturbance. Unlike soils, to model the rock material, the difference in strength and modulus between those of an intact sample and the global in-situ rocks must be assessed. The results of our review indicate that, based on data obtained from both laboratory and field tests, the overall strength of the in-situ fracture rock is only about 25% to 50% of the strength of intact rock specimens given by laboratory tests. Furthermore, the overall deformation moduli of the in-situ fracture rock are about 20% to 50% those of laboratory test values. The effect of strain-rate on the strength and modulus of soil varies considerably with soil types as well as with the stress history of a given soil. When the degree of saturation of the soil is greater than 85%, the strain-rate effect is more important. For several normally consolidated cohesive soils under review, a factor between 1.3 and 2.2 increase in strength and deformation modulus was observed. Our review of many types of rock tested under static conditions and under rapid strain-rates show that the strength could increase from 1.3 to 2.6 times from static loading to impact-type rapid-rate loading. Most of the data show that the strength factor increases in the range between 1.5 and 1.8. The strain-rate effects on the deformation modulus of many types of rocks under review is as important as the effect on strength. A factor between 1.3 to 2.0 increase in modulus is observed from static loading to dynamic impact loading conditions.

3.3.4.2 Effect of crash on geologic materials beneath the site

The third aspect of modeling that needs to be considered is the effect of an aircraft crash on geotechnical properties beneath the impact crater. The effect may be important for the specification of site requirement for controlled tests. During an aircraft accident, will the soil be densified by the nose of the plane before the package impact?

PSA Flight 1771 impacted at the crash site with high velocity (925 ft/s) and excavated a crater with maximum dimensions about 3.5 m deep by 6 m wide by 12 m long (11.5 ft x 20 ft x 40 ft). Materials expelled from the crater consisted largely of decomposed and intensely weathered sandstone and shale bedrock. Minor amounts of surface soil and vegetation were also ejected.

The effect of the crash on geological materials beneath the crater appears minor. A sample of decomposed rock obtained 12 ft below the surface in drill hole DH1, directly beneath the crater backfill, appears to have been slightly densified on the basis of the observation of its physical appearance

and the comparison of blow count numbers relative to similar materials sampled in the adjacent holes. The difference in blow count numbers is negligible. In addition, the basic properties and the strength does not appear significantly different from those of samples taken from other holes.

As discussed previously, the geological materials at the crash site have been over-consolidated, the material is considerably denser and stronger than the unconsolidated materials. The materials are compressed at an extremely high strain-rate when the plane crashes. Their behavior under high-velocity impact is very complicated. The state of stress changes with loading and unloading; heating and cooling; consolidation, spallation and vaporization. For over-consolidated geologic materials, some fractures may be introduced around the impact point from the initial crash. Thus, it is unlikely that the geological materials beneath the crater would be densified and become stronger. Criteria for impact surfaces used in the tests required by Section 5062 should therefore be based on crash site conditions existing prior to the crash.

3.3.5 Derived Constitutive Relation

Based on laboratory and field data, as well as consideration of scale-fracture and strain-rate effects, we recommend sets of constitutive relations that represent the important geotechnical properties of the PSA Flight 1771 crash site. Our main objective is to give the parameters for the material model (DYNA Model 5) that most closely represents the relationships already used by many investigators (Refs. 12, 20) for penetrator calculations.

3.3.5.1 Constitutive relation for soils

As discussed in previous sections, changes of soil density and intergranular effective stress are controlled by the volumetric compressibility characteristics of soils and by the degree of saturation existing for the soils at the time of the crash. The volumetric compressibility curve at various depths in the soil profile should be developed for impact-crash analysis. The procedure for development is described in Ref. 17. Curves developed for depths of 0.75 m (2.5 ft) and 1.5 m (5 ft) below the ground surface are illustrated in Fig. 3-14. The second aspect controlling volumetric strain and effective stress is the degree of saturation. During the crash impact, volumetric strain and effective stress increases can occur up to the point where the soil becomes saturated. The saturation limit may be identified from the variation of volumetric strain potential, with depth developed from the data of laboratory tests. As indicated in Fig. 3-14, the volumetric strains induced by the crash impact are anticipated to be sufficient in this case for the mean effective stress to increase beyond the past maximum consolidation stress to an essentially normally consolidated state. The soil is

expected to behave under shear according to characteristics for normally consolidated saturated-undrained conditions.

The variations of undrained shear strength with depth are shown in Fig. 3-15. By applying strain effect to their strength, the ultimate strength expected to be mobilized during the crash impact is given by the band as labeled in the figure. This band represents an increase of strength due to rapid loading on the order of 35% to 50%. This effect was evaluated using the expression developed in Ref. 17.

$$S_1/S_0 = (\varepsilon_1/\varepsilon_0)^{A*OCR}$$

in which S_0 and S_1 are soil strengths at strain-rates ε_0 and ε_1, respectively, OCR is the over consolidation ratio of the soil, and A is the empirical coefficient. This empirical equation may be determined from the following equation

$$A = 10^{(PI/76 - 1.75)}$$

in which PI is the plasticity index described in Section 3.3.3. The plasticity index for the site is 11 ± 4. The values of OCR were estimated to be about 100 at the depth of 0.2 m and about 85 at the depth of 0.75 m below the ground surface.

The yield surface is modeled as cone-shape as described in section 3.3.2.1. The slope of failure limit is 0.37. The cohesive strength and the tensile strength are zero.

The other parameters required for the model developed for the PSA Flight 1771 crash site soils have been shown in Table 3-2.

3.3.5.2 Constitutive relation for rocks

The development of the constitutive relation of the PSA Flight 1771 crash site rocks for impact analysis is based on the data of numerous laboratory tests on samples collected from several locations in the crash crater region.

A total of 10 unconfined uniaxial compression tests were performed on rock specimens selected from cores of exploratory drilling holes and from float (outcrop) samples during the excavation for the gas-gun penetration test. In addition, a total of 13 triaxial compression tests were performed either on core or outcrop samples over different confining pressures up to 500 MPa. These test data provide the strength and stress-strain behavior of the intact rocks of the PSA Flight 1771 crash site.

As shown in Section 3.3.3, the rock tested at low confining pressure or unconfined condition fails in a brittle manner when the stress state reaches its ultimate strength. The failure strain is relatively small. On the other hand, the samples tested at pressures of 100 MPa and above always show ductile strain hardening behavior, with compressive strength increasing with strain at high pressures.

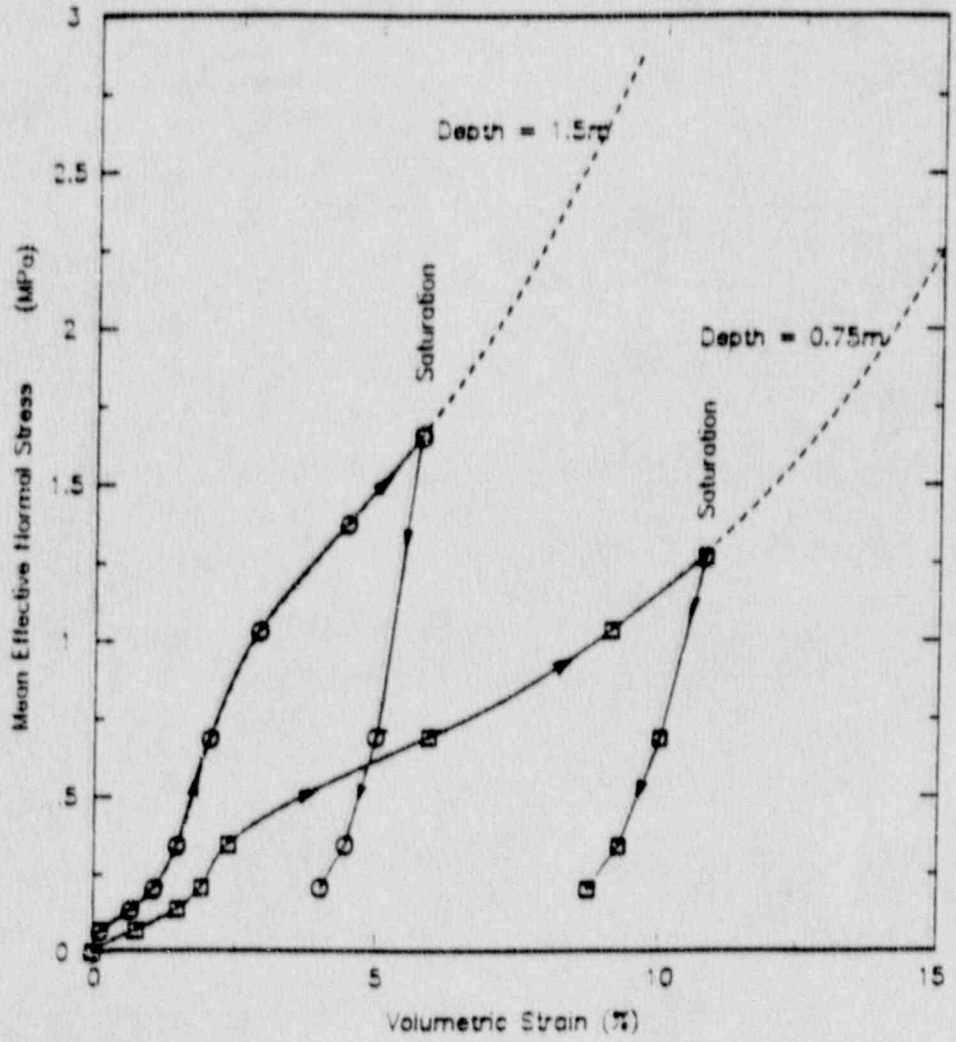

Figure 3-14. Expected compressibility, saturation, and effective stress behavior during impact loading for depths of 0.75 and 1.5m of the PSA Flight 1771 crash site soil.

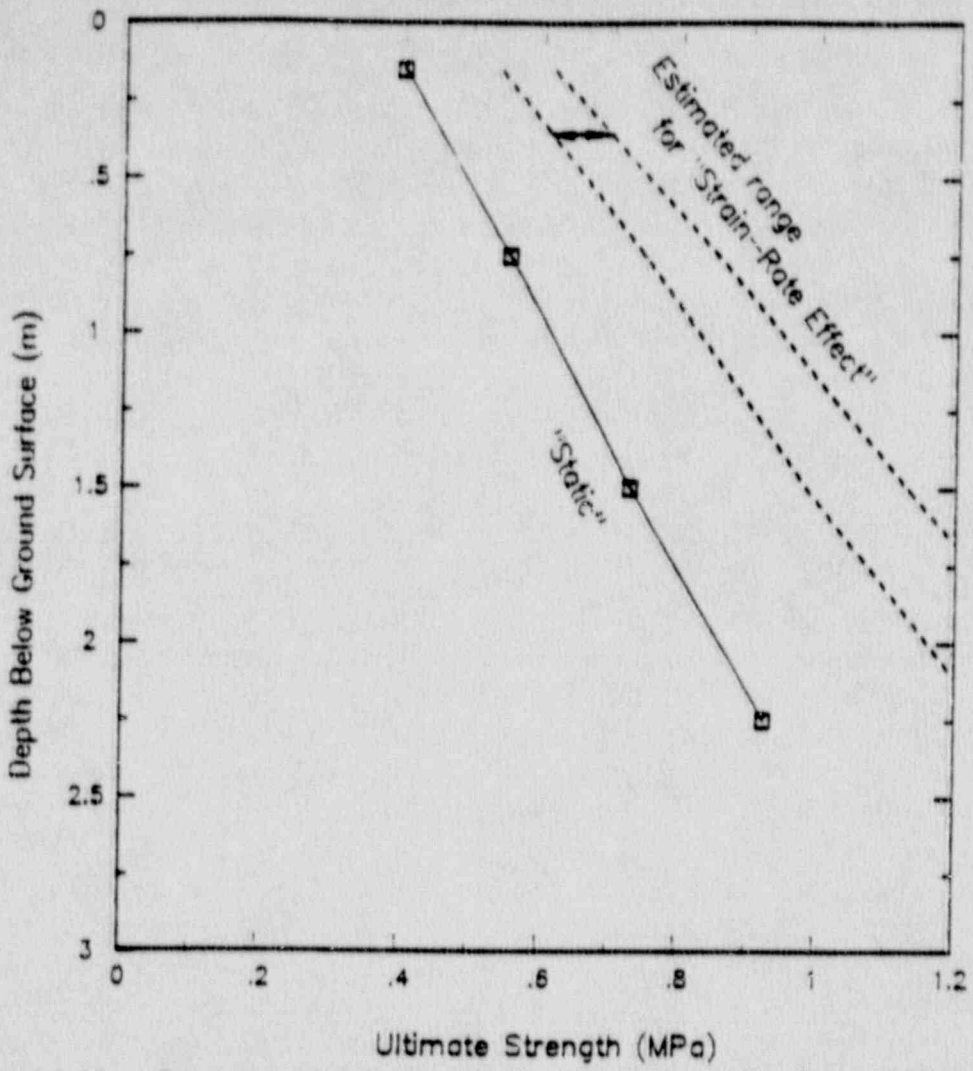

Figure 3-15. Expected depth variation of ultimate strength of the PSA Flight 1771 crash site soils for static and loading conditions.

Generally, the failure surface may be defined by the envelope of the failure strength in individual unconfined and triaxial test. The "failure point" may be clearly defined as the ultimate strength in unconfined or low confined compression tests. However, for high confining pressure tests when the material shows ductile behavior, the failure point may also be defined by its ultimate strength or by the stress level associated with a certain amount of strain.

One can always define the failure surface as the ultimate strength the sample can support at a given confining pressure without concerning the magnitude of strain. The problem with this definition of failure surface could lead to an overestimate of response load and underestimate of penetration depth because the yield limit may be set too high. Thus, according to Kreig's model (DYNA Model 5), we need to define a yield surface instead of failure surface.

Two approaches have been taken: (1) For brittle failure data of uniaxial unconfined tests, the yield is defined at its ultimate strength and for ductile

failure data of confining triaxial tests, the yield stress is defined at the stress level that requires 0.5% of strain deviation from linear elastic behavior. This yield surface is shown in Fig. 3-16 labeled as yield surface #2. (2) For simplicity, the yield surface is defined at the stress level of 50% of ultimate strength as shown in the figure (labeled "yield surface #1"). This yield limit allows the plastic deformation to occur more easily because the stress level is reduced to a strain deviation of 0.1% or less from the elastic behavior. It is noted that the shape of these two yield surfaces are the same within the pressure range of stress ratio less than 4. It is only slightly different in shape when the stress ratio is greater than 4.

Since we need to apply scale factors for fracture and strain-rate effects, we select the yield surface #1 as the basis for the benchmark analysis. It is also noted that the average unconfined strength (σ_u) of the weathered rock at the PSA crash site is about 22 MPa. At the mean pressure of 88 MPa (13 ksi) or greater, the use of different yield surfaces will lead to a different prediction of response load and penetration depth. It is anticipated that the specification of yield surface #2 will give much higher loads and less penetration if the mean normal pressure is greater than 88 MPa.

Tables 3-4 through 3-6 show the laboratory data points used to develop yield surface #1 and yield surface #2. The data points marked "high strain-rate" and "unweathered" were not used, simply because the strain-rate effect would be accounted for from a scale factor and the rock near the surface is severely weathered. Fig. 3-17 shows the actual laboratory test data and the defined yield surface. After these data points are selected to define the yield surface, the stress invariant, J_2, may be calculated and the least squares method as defined in Section 3.3.2 may be applied to determine the constants of yield functions.

Typical pressure versus volumetric-strain relationships obtained from isotropic compression tests on samples of outcrop and core materials are shown in Fig. 3-11. For the outcrop sample, a total of four cycles were performed during the test. The first cycle was loaded up to 8 MPa and then unloaded to zero. The sample was reloaded to 8 MPa again and then was increased up to 50 MPa and 70 MPa and down to zero to complete the second cycle. At each pressure step, the volume change was recorded and the volumetric strains were calculated. The tests were repeated with four cycles and pressure increased to 400 MPa. Observations of the P-V tests showed that, during the first stage of loading up to 70 MPa, the crack and large void in the material was closed. From the loading stage of 70 MPa to 250 MPa, the pore voids were collapsed and the materials were more compacted. For

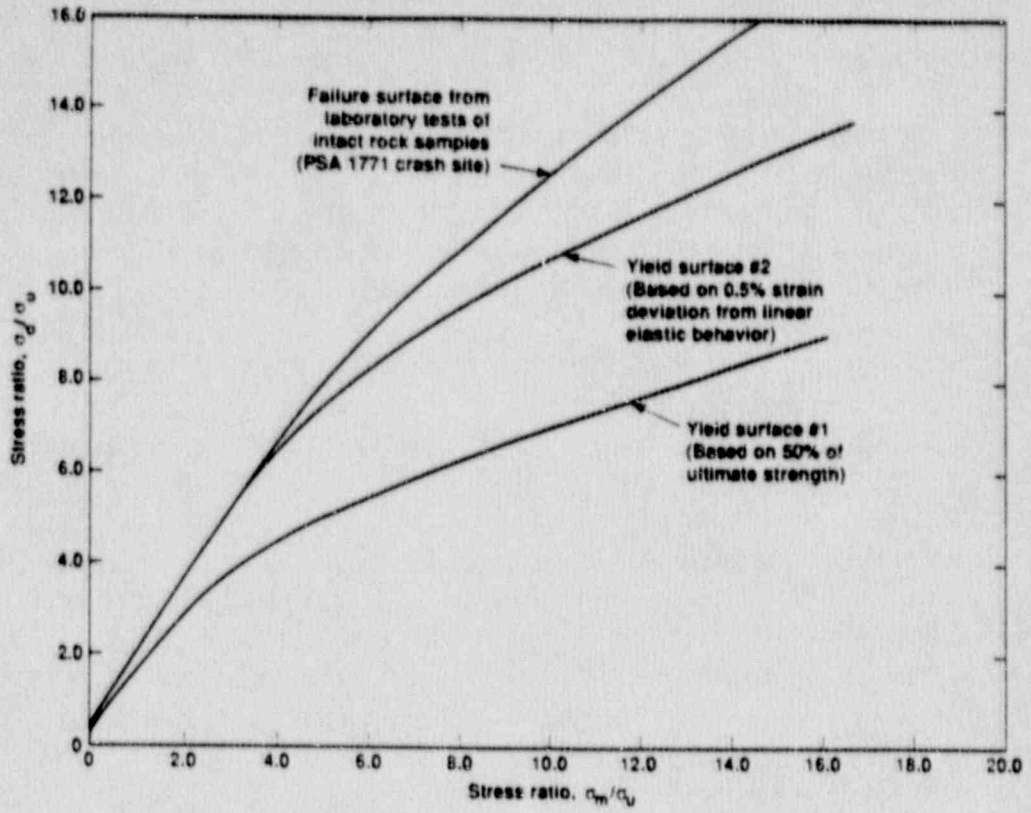

Figure 3-16. Normalized failure surface and the defined yield surface based on laboratory test data of intact specimens.

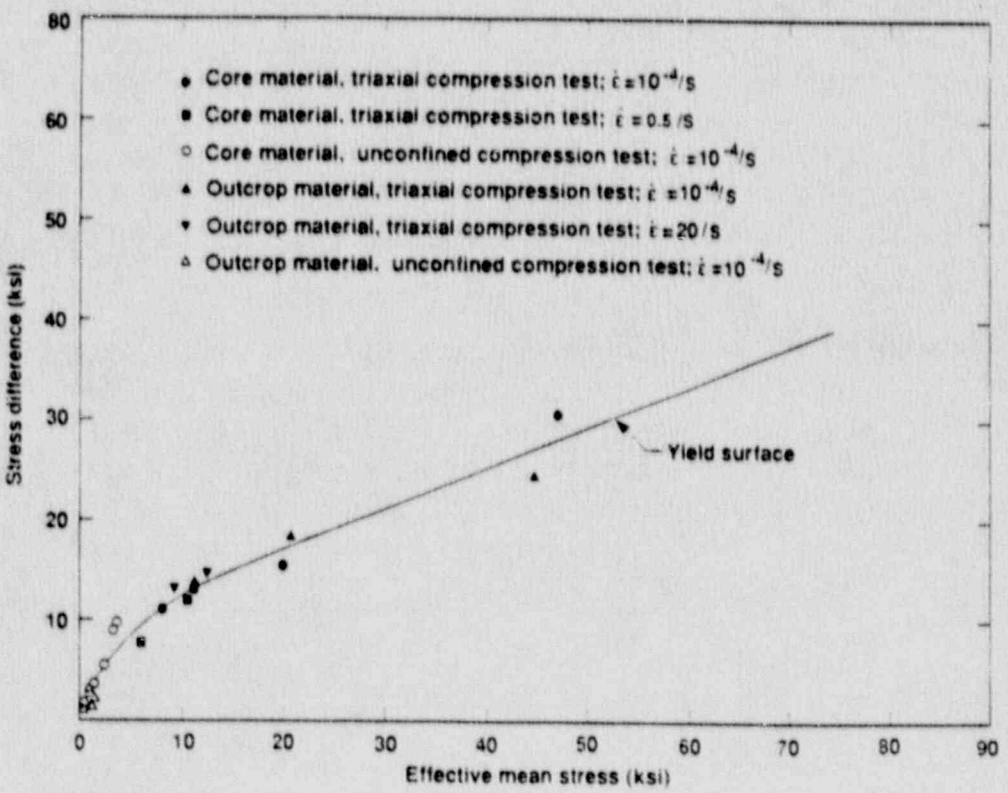

Figure 3-17. The defined yield surface #1 and the data points of laboratory compression tests of intact specimens of the PSA Flight 1771 crash site rocks.

pressures above 250 MPa, the material was in grain-to-grain contact and was eventually crushed. It can be seen that the loading history has an important effect on the loading and unloading modulus. The bulk loading modulus increases as the pressure increases while the bulk unloading modulus remains essentially unchanged after the first cycle.

The loading bulk modulus calculated from the weighted average of test data up to the confining pressure of 250 MPa is 5476 MPa. The envelope of the loading curve represents the P-V behavior of the intact sample of the outcrop material.

A total of five cycles of loading and unloading were conducted on drill core samples. As can be seen from Fig. 3-11, the behavior of the drill core sample during the first cycle of compression is similar to the outcrop sample. The first cycle in each case represents the closure of pre-existing fissures and large voids. During the second cycle, the core sample is more compressible than the outcrop sample. This fact is probably due to the high water content and the low density (2.19 g/cm^3 vs. 4.35 g/cm^3 of average density). After the third cycle, the behavior is similar to the outcrop sample. The average value of the bulk unloading modulus is 4723 MPa.

The envelope of the loading curve of the P-V test represents the P-V behavior of the intact sample of the core material. This curve with appropriate scale factors accounting for fracture and strain-rate effect is used for the lower layer incorporated in the computation model.

The other parameters (obtained from the laboratory tests) required for the model developed for the PSA crash site rocks have been shown in Table 3-3.

These constitutive properties are based primarily on the evaluation of laboratory tests on small scale intact samples collected from different locations around the crash crater. Scale factors accounting for the effect of in-situ rock mass characteristics and of high strain-rate impact loading, as summarized at the end of Section 3.3.4, should be explicitly applied to the laboratory data. The parametric study in the following section will show the sensitivity of these parameters and lead to the best-estimate model for crash-impact analysis.

Table 3.4. "Yield stress 1" defined by 50% ultimate strength of intact specimens of outcrop material from laboratory compression tests.

Sample ID	σ_3 (MPa)	$0.5(\sigma_1 - \sigma_2)_{ult}$ (MPa)	ε_y (%)	σ_m (MPa)	E (GPa)	Strain rate (s^{-1})	Remarks
OC2-BV	250.	170.0	2.0	306.7	8.75	10^{-4}	
OC2-AV	100.	129.0	1.6	143.0	8.25	10^{-4}	
OC2-CP	50.	91.0	1.8	80.3	5.31	10^{-4}	
OC1-1CV	50.	90.0	1.9	80.0	4.52	0.5	
OC3-BV	50.	106.0	1.3	85.5	8.52	20.0	High Rate
OC3-AV	25.	93.8	1.2	56.3	7.81	20.0	High Rate
OC2-4Ap	0.	8.0	0.35	2.7	2.60	10^{-4}	
OC2-4Bp	0.	10.5	0.39	3.5	3.30	10^{-4}	
OC2-4AV	0.	15.0	0.35	5.0	5.60	10^{-4}	
OC2-4BV	0.	11.5	0.37	3.8	3.80	10^{-4}	

Table 3.5. "Yield stress 1" defined by 50% ultimate strength of intact specimens of core material from laboratory compression tests.

Sample ID	σ_3 (MPa)	$0.5(\sigma_1 - \sigma_2)_{ult}$ (Mpa)	ε_y (%)	σ_m (MPa)	E (GPa)	Strain rate (s^{-1})	Remarks
DH1-4a	500.	437.5	6.3	645.8	6.98	10^{-4}	Unweathered
DH2-3a	250.	215.0	5.0	321.7	4.30	10^{-4}	
DH5-3a	100.	110.0	3.3	136.7	3.33	10^{-4}	
DH1-5	50.	90.0	2.4	80.0	4.13	10^{-4}	
DH3-6av	50.	80.0	–	76.7	–	0.5	
DH1-4b	25.	82.5	1.4	52.5	6.00	10^{-4}	
DH3-6b	25.	57.0	–	44.0	–	0.5	
DH2-7c	0.	66.5	0.45	22.2	14.7	10^{-4}	Unweathered
DH2-8a	0.	8.5	0.4	2.8	2.9	10^{-4}	
DH4-4	0.	44.0	–	14.7	9.8	10^{-4}	Unweathered
DH4-5	0.	71.5	0.6	23.8	11.9	10^{-4}	Unweathered
DH4-7	0.	21.0	–	7.0	–	10^{-4}	Unweathered
DH5-4a	0.	11.0	0.6	3.7	1.9	10^{-4}	

Table 3.6. "Yield stress 2" defined by stress levels required 0.5% strain deviation from linear elastic behavior for intact specimens of outcrop and core materials.

Sample ID	σ_3 (MPa)	$0.5(\sigma_1 - \sigma_2)_{ult}$ (MPa)	ε_y (%)	σ_m (MPa)	E (GPa)	Strain rate (s^{-1})
OC2-BV	250.	270.	3.3	340.0	8.75	10^{-4}
OC2-AV	100.	230.	3.3	176.7	8.25	10^{-4}
OC2-CP	50.	165.	3.5	105.0	5.31	10^{-4}
OC1-1CV	50.	140.	3.8	96.7	4.52	0.5
OC2-4AP	0.	16.	–	5.3	2.60	10^{-4}
OC2-4BP	0.	21.	–	7.0	3.30	10^{-4}
OC2-4AV	0.	30.	–	10.0	5.60	0.5
OC2-4BV	0.	23.	–	7.7	3.80	10^{-4}
DH2-3a	250.	312.	7.8	354.0	4.30	10^{-4}
DH5-3a	100.	175.	5.8	158.3	3.30	10^{-4}
DH1-5	50.	168.	4.5	106.0	4.13	10^{-4}
DH1-4b	25.	140.	3.0	71.7	6.00	10^{-4}
DH2-8a	0.	17.	–	5.7	2.90	10^{-4}
DH5-4a	0.	22.	–	7.3	1.90	10^{-4}

4. BEST-ESTIMATE MODEL

In this section, we present the results of a sensitivity study on benchmark analysis of penetration tests. Many DYNA2D calculations were performed to select the best-estimates of material properties at the site. Each calculation is identified by RND series. The sensitivity study was performed by the variation of input parameters to determine the effect of each material parameter on the depth of penetration and the response deceleration. The most important parameter affecting the calculation results is the defined yield surface function, which is related to the yield stress level of the material. The shear modulus and bulk unloading modulus are also important. Although the P-V curve is important, it is not as sensitive as yield surface functions.

We compared the results of these analyses with the experimental data, and we determined that RND29 provides the best estimate of properties. Selection criteria are based on the close agreement of calculational results with experimental data, as well as considerations of conservatism. After the best-estimate material properties were selected, we also performed two analyses for upper- and lower-bound properties. The definition of upper- and lower-bound properties was based on one standard deviation from the mean of the available data; this is described in a later section.

4.1 Comparison of Calculations to Experimental Data

Calculated results in average deceleration, penetration depth, time histories (acceleration, velocity, and displacement) from the best-estimate model are compared to the experimental data. The instrumented data from the forward station of Test No. 2 are used for the comparison. Table 4-1 shows the comparison of average deceleration and the penetration depth. The average decelerations are obtained from the maximum slope of the velocity time history within the defined time window. The weighting average values over the defined time window are also compared. Within the earlier time (within 5 ms) of impacting, the calculated result appears higher than the experimental data. Close agreement is observed within the time window of 5 to 10 ms. The value of calculated penetration depth is very close to the experimental data.

The calculated deceleration time history of the best estimate model is shown in Fig. 4-1. Observation between this time history and the measured acceleration time history (Fig. 2-3) shows that the overall trend of the deceleration time histories are similar up to the first 16 ms. After 16 ms the calculated time history shows that the penetrator still has some degree of high frequency oscillation in amplitude till the end of calculation at 23 ms. However, the experimental data shows that the penetrator is stopped around 20 ms. The integrated velocity and displacement time histories are shown in Figs. 4-2 and 4-3. The characteristics of both time histories are

generally similar to those of the experimental data. The variation of kinetic energy with time during the process of penetration is shown in Fig. 4-4. At the end of calculation the level of kinetic energy is about 1.6% of the maximum kinetic energy. The final position of the penetrator of the calculation model is shown in Fig. 4-5.

Table 4-1 Comparison of calculations to experimental data.

	Average deceleration (g)			Total penetration depth (ft)
	Upper layer		Lower layer	
	(0-5 ms)	(5-10 ms)	(>10 ms)	
Experiment*	2144 (1917)	1736 (1622)	972 (972)	7.3
Best estimate	2554 (2313)	1697 (1241)	739 (310)	7.6
Upper bound	3471 (3197)	1883 (808)	471 (366)	5.9
Lower bound	1519 (1413)	1346 (1120)	681 (511)	11.8

* See Table 2.1 and Figure 2-4, Test 2.

Note: The values in parentheses are based on weighting average values over the defined time window.

4.2 Sensitivity Study

From the calculation results, we investigated the effect of each parameter on the response deceleration and the depth of penetration of the penetrator. Because the variation of material densities for this site is not significant (COV = 5.2%), the average density of 2.35 g/cm^3 (146 lb/ft^3) was used for each case. The effect of tension cutoff may be important, however, owing to the intensely weathered and fractured nature of the site. The tension cutoff was therefore set to essentially zero (0.1 Pa or 1.45 x 10^{-5} psi) for all cases. The remaining parameters are shear modulus, bulk unloading modulus, P-V curves, and yield functions. From case to case, one or more than one parameter were changed in order to achieve the best result in comparing the calculation to the experiment data.

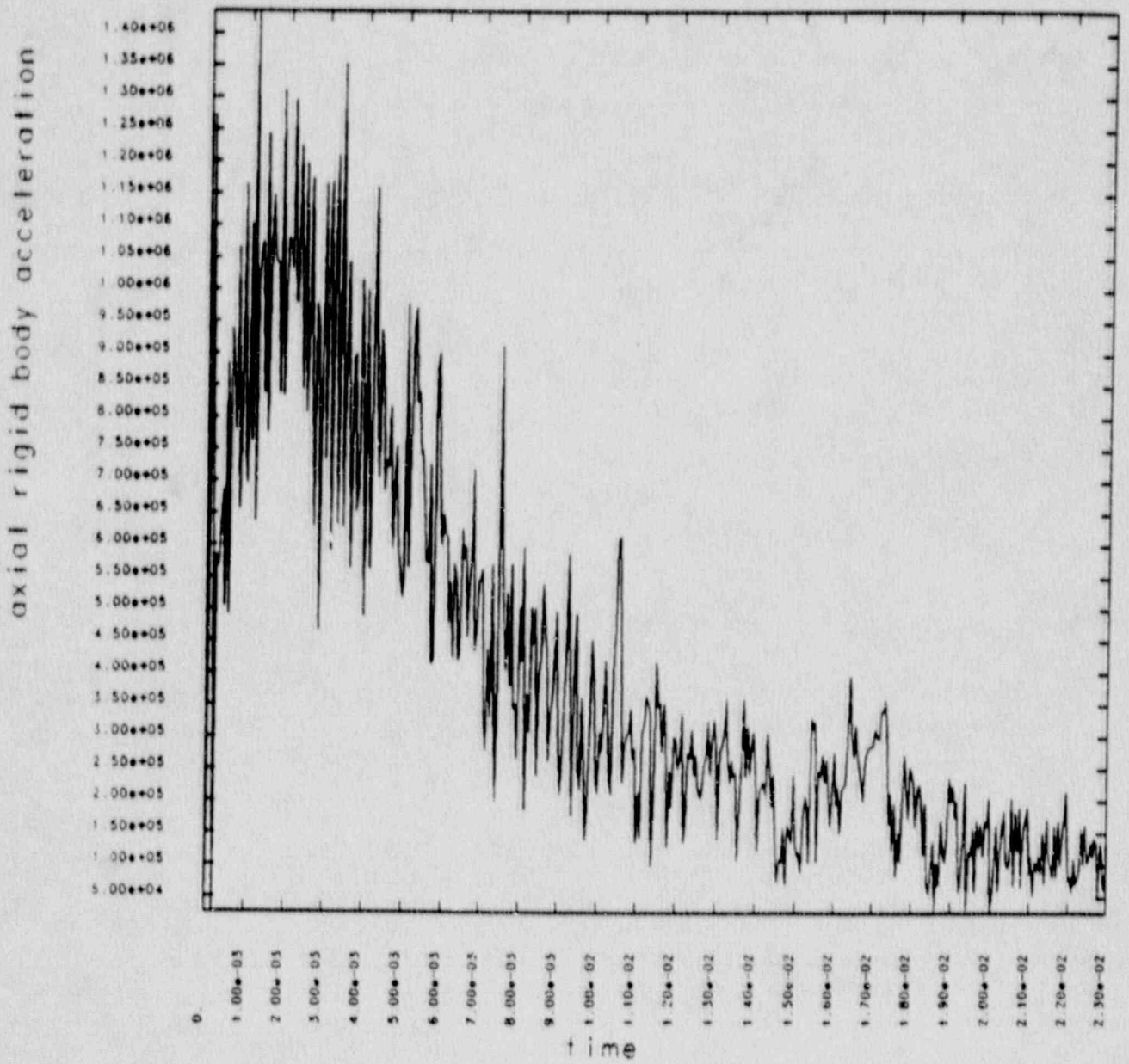

Figure 4-1. Calculated acceleration time history of the best estimate model RND29.

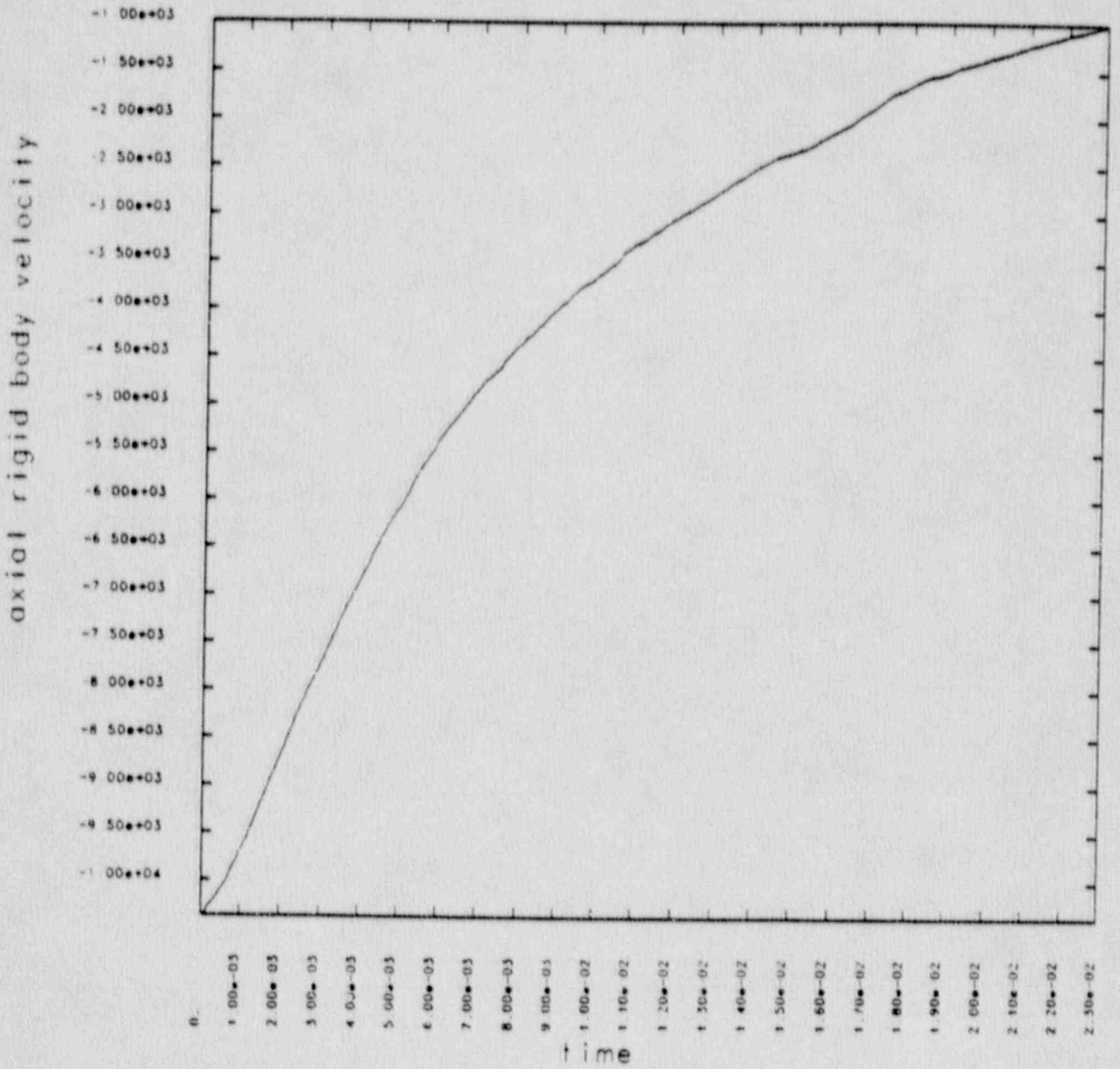

Figure 4-2. Calculated velocity time history of the best estimate model RND29.

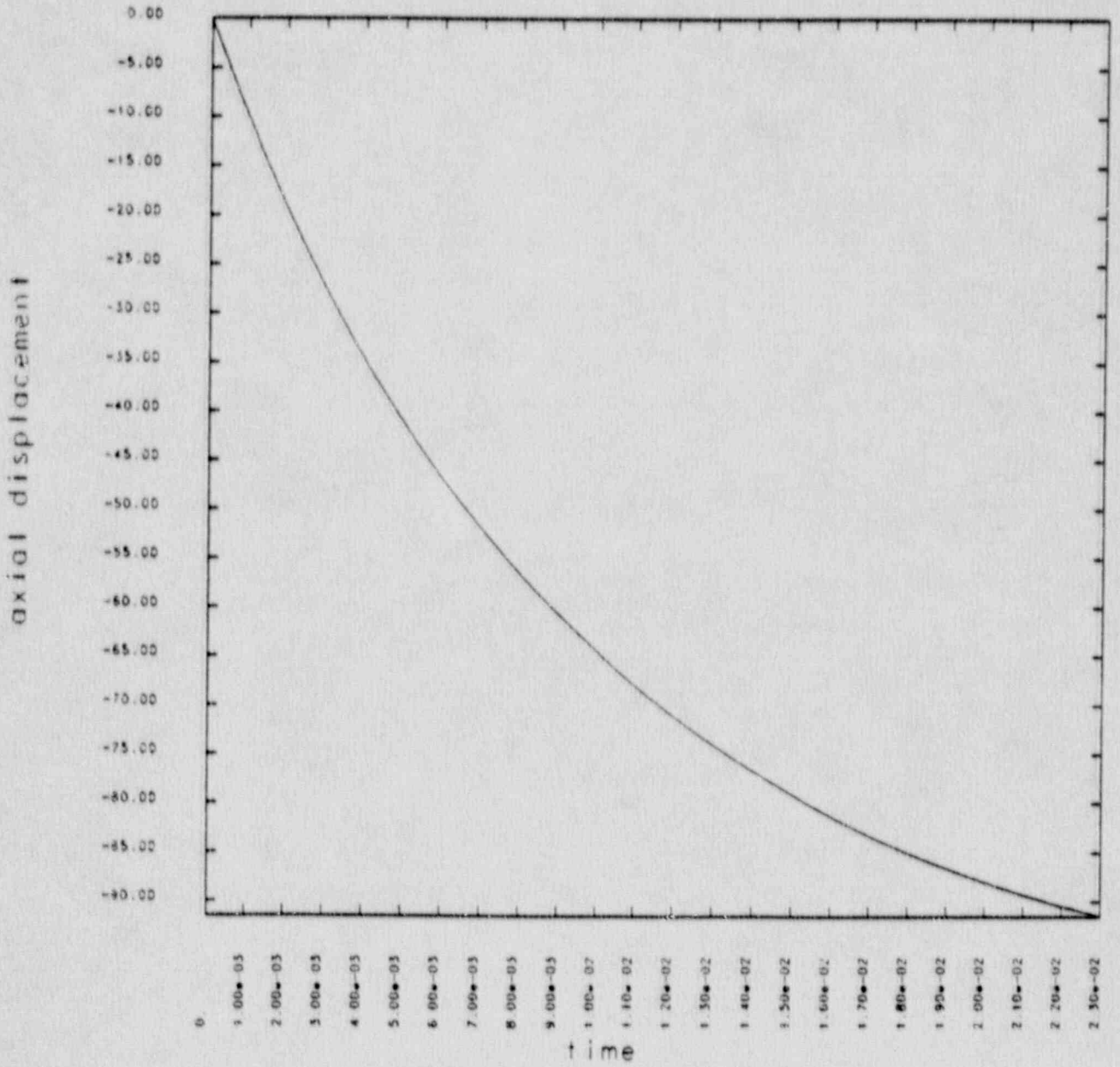

Figure 4-3. Calculated displacement time history of the best estimate model RND29.

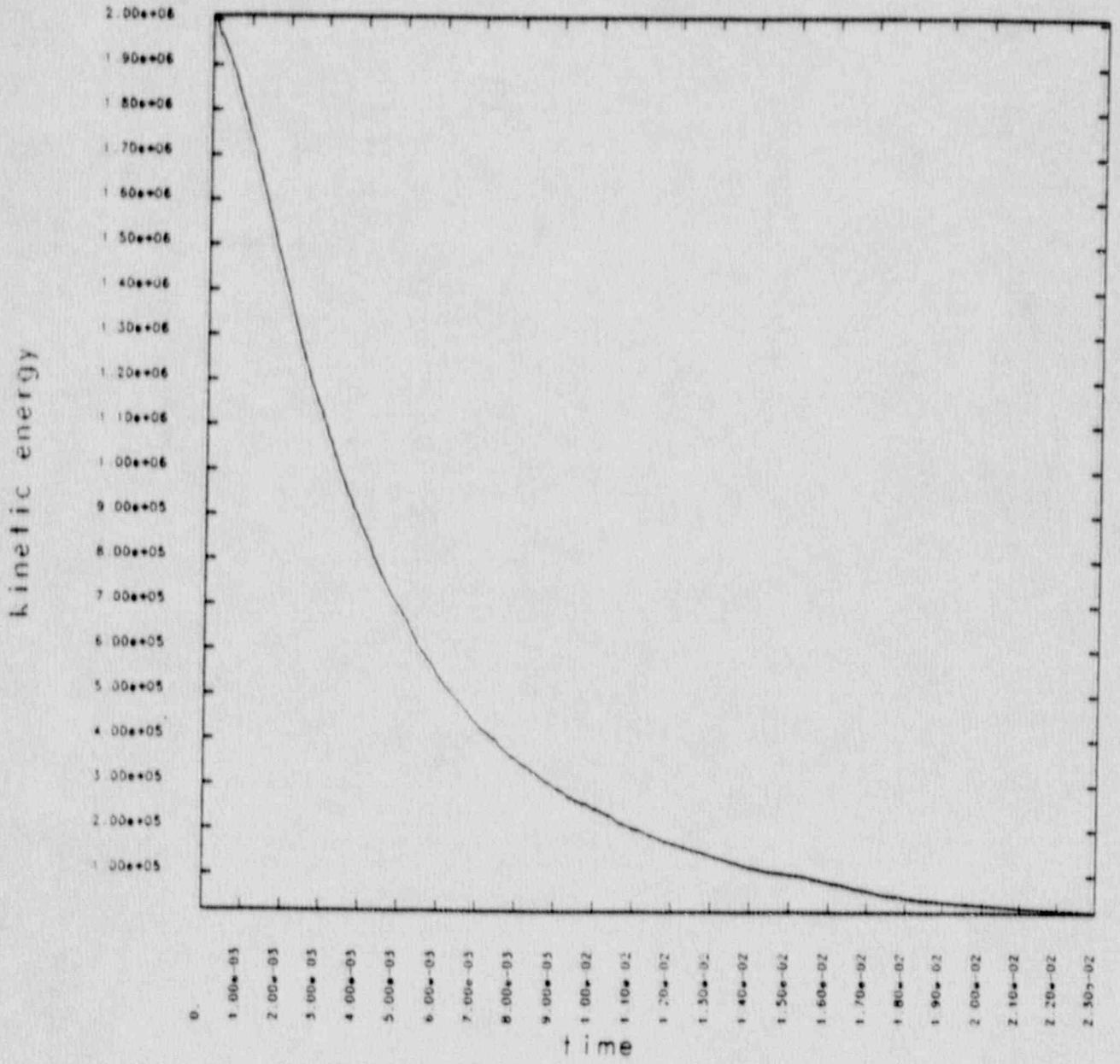

Figure 4-4. The variation of kinetic energy with time during the process of penetration for the best estimate model RND29.

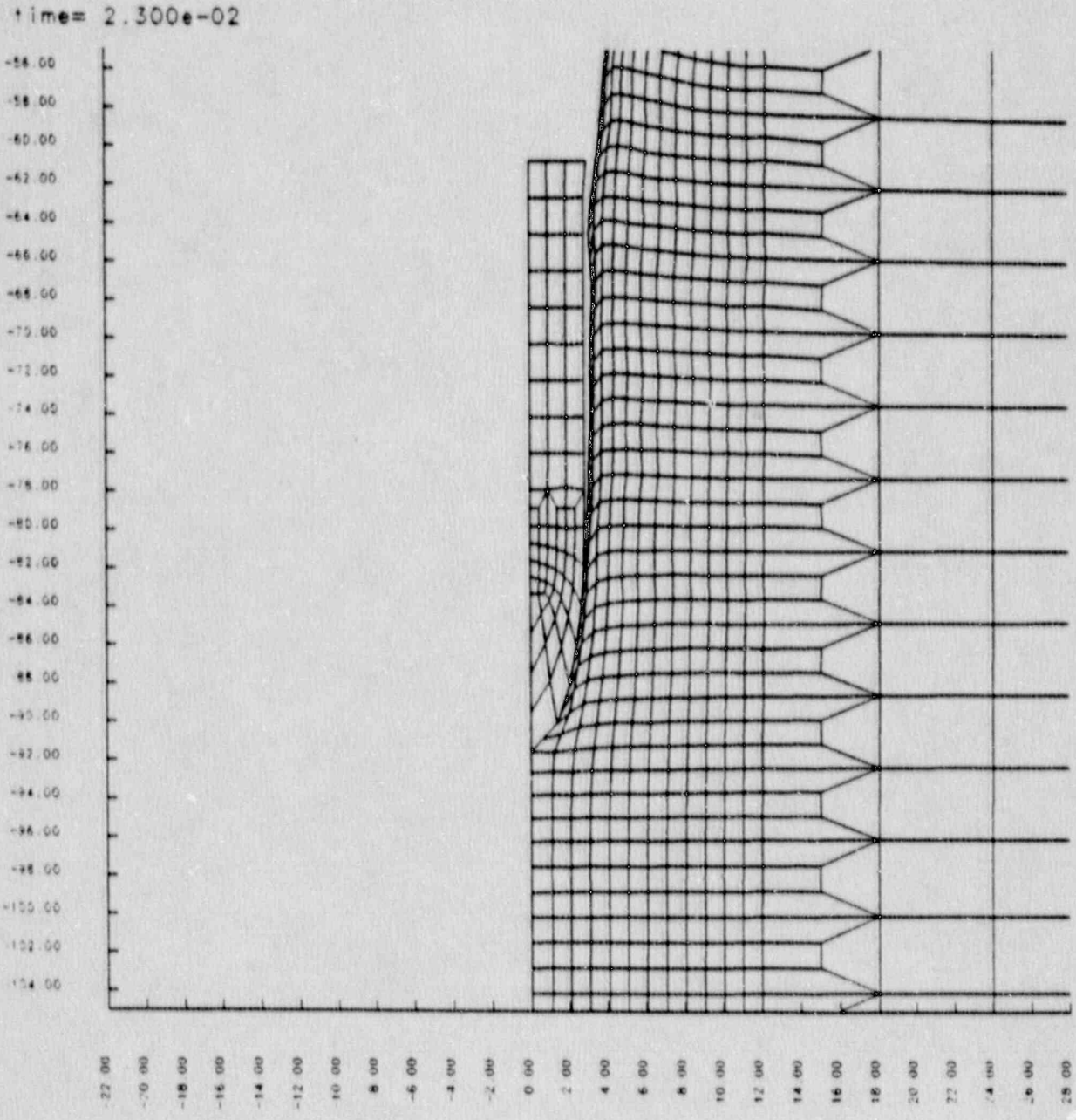

Figure 4-5. The depth of penetration at the final time step of calculation, the best estimate model RND29.

The parameters that were used in the calculations are shown in Table 4-2. In this first calculation, the impact velocity of 274.4 m/s (900 fps) was used. The stress reduction factors of 1.5/4 and 1/4 are applied to the defined yield shear stress for the upper layer and the lower layer. The modulus reduction factors of 1.5/4 and 1.5/3 are also applied to the P-V curve of the upper and lower layers. The average shear modulus value of 1807 MPa (2.62×10^5 psi) was obtained on the basis of all unconfined and triaxial compression tests on weathered samples. The average shear modulus drops to 1310 MPa (1.9×10^5 psi) if we consider only the test results of a subset of 6 unconfined compression tests. This may be a low end of shear modulus to begin benchmark analysis. The factor of 1.5/4 was also applied to scale the average shear modulus obtained from laboratory tests on intact samples.

Thus, the shear modulus of 490 MPa (7.1×10^4 psi) was used for RND19. The unscaled bulk unloading modulus of 9448 MPa (1.37×10^6 psi) obtained from the early stage of P-V test data was used for this case. The results show that the average deceleration was 1786 g, and the total penetration depth was 3.1 m (10.2 ft).

The results of RND19 show that the calculated penetration is about 91.5 cm (3 ft) deeper than the measured penetration of 2.2 m (7.3 ft), and the average deceleration is about 1786 g for calculation versus about 2144 g for experiment. Thus, the model appears too soft. The model needs to be adjusted for less compressibility. In the calculation of RND20, we first tried to increase the modulus reduction factor from 1.5/4 to 2/4 for the upper layer and from 1.5/3 to 2/3 for the lower layer. By applying the new factors, it is expected that the volumetric strains would reduce about 20%. The input impact velocity was changed from 274.4 m/s to 263.4 m/s (900 fps to 864 fps) of the actual impact velocity for this particular experiment, which was selected for benchmark analysis. The reduction of impact velocity implies the reduction of 4% of kinetic energy. The combined reduction of about 20% of the modulus reduction factor and 4% of the kinetic energy would have reduced the depth of penetration to about 24%.

The shear modulus and the yield function remained unchanged from RND19. However, in RND20 we evaluated and changed the bulk unloading modulus for both layers based on additional data from P-V tests. The average unloading modulus for pressure up to 250 MPa (36.25 ksi) is 4896 MPa (7.10×10^5 psi) for the upper layer and 4724 MPa (6.85×10^5 psi) for the lower layer. The modulus reduction factors of 2/4 and 2/3 were applied for each layer respectively. The results of RND20 show an average deceleration of 2009 g and a total depth of penetration of 2.6 m (8.4 ft). The reduction of penetration from RND19 is about 18%.

The target system still appears a little bit too soft. In response to these results in RND21, we tried to model the bottom layer to be 20% less compressible, and we also increased the shear modulus of the whole system from 490 MPa (0.71×10^5 psi) to 655 MPa (0.95×10^5 psi). The effect of shear modulus on the response load is important. The maximum average deceleration increases from 2009 to 2417 g. The results of

Table 4-2 Sensitivity study on benchmark analysis of gas-gun penetration tests.

Calculation ID*	G 10^5 (psi)	K_u 10^5 (psi)	P-V relation deforma. modul. redc. factor	Yield stress reduction factor	Yield function contants			Max. ave. deceleration (g)			Pene. depth (ft)	E_{min}/E_{max} (%)
					a_0 10^5 (psi)^2	a_1 10^2 (psi)	a_2 10^{-3}	(0-5) ms	(5-10) ms	(>10) ms		
RND19	0.71	13.70 (13.70)	1.5/4 (1.5/3)	1.5/4 (1/4)	1.87 (1.08)	7.95 (3.77)	3.41 (1.25)	1786 (1786)	1508 (1350)	1021 (789)	10.2	1.1
RND20	0.71	3.55 (4.57)	2/4 (2/3)	1.5/4 (1/4)	1.87 (1.08)	7.95 (3.77)	3.41 (1.25)	2009 (1927)	1866 (1339)	859 (717)	8.4	2.2
RND21	0.95	3.55 (4.57)	2/4 (2/2.5)	1.5/4 (1/4)	1.87 (1.08)	7.95 (3.77)	3.41 (1.25)	2417 (2148)	2148 (1235)	685 (536)	8.9	1.5
RND22	0.95	3.55 (4.57)	2/4 (2/2.5)	1.5/4 (1.2/4)	1.87 (1.40)	7.95 (5.30)	3.41 (1.93)	2436 (2113)	2113 (1245)	891 (538)	8.0	3.5
RND24	0.95	4.73 (5.48)	2/3 (2/2.5)	1.5/4 (1.2/4)	1.87 (1.40)	7.95 (5.30)	3.41 (1.93)	2184 (1902)	1432 (1241)	613 (513)	8.8	3.8
RND25	0.95	3.55 (4.57)	2/3 (2/2.5)	1.5/4 (1.2/4)	1.87 (1.40)	7.95 (5.30)	3.41 (1.93)	2214 (2093)	1775 (1179)	579 (570)	7.4	8.4
RND26	0.95	3.55 (4.57)	2/4 (2/3)	1.5/4 (1.2/4)	1.87 (1.40)	7.95 (5.30)	3.41 (1.93)	2282 (2035	1813 (1308)	964 (691)	8.2	1.4
RND27	1.26	5.29 (4.57)	2/3 (2/3)	1.5/4 (1.2/4)	1.87 (1.40)	7.95 (5.30)	3.41 (1.93)	2324 (2055)	1840 (1382)	581 (457)	8.2	2.1
RND28	1.26	5.29 (4.57)	2/3 (2/3)	2/4 (1.5/4)	2.49 (1.87)	13.27 (7.95)	7.01 (3.41)	3109 (2558)	1531 (1139)	550 (437)	7.2	1.8
RND29	1.26	5.29 (4.57)	2/3 (2/3)	1.75/4 (1.5/4)	2.22 (1.87)	10.48 (7.95)	5.02 (3.41)	2554 (2315)	1697 (1300)	739 (528)	7.6	1.6
The values in parentheses refer to parameters or properties of the bottom layer.								The values in parentheses are based on weighting averages over the defined time window.				

*RND19, V = 900 ft/s; RND20 to RND29, V = 864 ft/s.

G = Shear modulus

K_u = Bulk unloading modulus

E_{min} = Minimum kinetic energy

E_{max} = Maximum kinetic energy

the RND21 calculation indicate that the response load of the bottom layer was relatively lower than that of the experimental data. Therefore, in RND22 we increased the yield stress reduction factor for the lower layer from 1/4 to 1.2/4. Due to this change, the maximum average deceleration in the bottom layer increases from 685 to 891 g. The effect of the yield stress level is significant.

Up to the RND22 test calculation, the response level is about right. However, the window of penetration is still about 2 ms larger than the field data. Since the thickness of 1.7 m (5.5 ft) in the first layer of the model is about 76% of the total penetration depth of the experimental data, one way to reduce the total depth of the penetration is to increase the deformation modulus of the first layer.

If we increase the modulus scale factor from 2/4 to 2/3 (as shown in RND25), the weighting average value of deceleration is practically the same as that for RND22. Since the calculation stops at 16 ms, the depth of penetration also stops at 2.3m (7.4 ft). There is still 8.4% of kinetic energy left. The effect of increasing the modulus factor from 4/2 to 2/3 for the first layer does not significantly change the response load and the depth of penetration.

The effect of increasing the unloading bulk modulus can be seen by the comparison of the results between RND24 and RND25, as well as RND19 and RND20. The increase in unloading bulk modulus gives a smaller response deceleration and a larger depth of penetration. The effect of shear modulus is observed by comparing the results between RND20 and RND26. By increasing 33% of shear modulus in the calculation, the acceleration response in earlier time increases about 6% and the depth of penetration decreases about 3%. From the investigation of the calculation results among RND19 to RND26, we found that the change in each factor such as shear modulus, unloading bulk modulus, or P-V curve has an important effect on the calculated response deceleration and penetration depth. The combination of these factors shows more important effects in some cases.

The effect of yield surface on the response deceleration and penetration depth can be seen from the comparison of the results among RND27, RND28, and RND29. The value of shear modulus, unloading bulk modulus, and P-V curve are kept for the same value, but the scale factors are changed from 1.5/4 to 2/4 for the upper layer and from 1.2/4 to 1.5/4 for the lower layer. The results show that the effect of yield surface is very significant.

4.3 Best-Estimate Model

The calculational results of RND26 compare well with the experimentally determined deceleration, but do not compare well in the depth of penetration. The latter comparison is: 2.5m (8.2 ft), calculated; and 2.23 m (7.3 ft) experimental. To respond to this situation, we made the first layer less compressible and made the system a bit stiffer. The modulus reduction factor increases from 4/2 to 2/3. The factor of 2/3 is desirable because it is consistent with the factor of the lower

layer. We also applied this factor to the unloading bulk modulus and shear modulus of the suggested laboratory values of 5476 MPa (7.94 x 10^5 psi) and 1307 MPa (1.90 x 10^5) as reported in section 3.3.5. The resulting shear modulus of 871 MPa (1.26 x 10^5 psi) used in the model is equal to the shear wave velocity of 610 m/s (2000 ft/s) in an elastic system with density of 2.35 g/cm^3 (146 lb/ft^3). The values of shear wave velocity and density actually are equal to the in-situ measurements of the PSA Flight 1771 crash site. The scale factor of 2/3 actually consists of a factor of 2 for the high strain-rate effect and a factor of 1/3 for scale-fracture effect. The values of these factors are based on the result of our literature review.

To reduce the depth of penetration in RND28, we increased the yield stress factors from 1.5/4 for the upper layer to 2/4 and from 1.2/4 to 1.5/4 for the lower layer. The effect of these adjustments on the responses are very significant. The response deceleration increases 24% from RND26. The average value in the earlier time is 2558 g. The depth of penetration becomes 3 m (7.7 ft), which is a 12% of reduction from RND27. Because the major amount of kinetic energy is required to break through the hard surface layer, it is seen that the later response is relatively weak compared to the experimental data. Thus, we dropped the stress factor from 2/4 to 1.75/4 for the upper layer (RND29) and kept the remaining parameters the same as those for RND28. The results are closer to the experimental data. The response acceleration is higher but conservative. We therefore identify RND29 as the best estimate model. The factor of 1.5 to 1.75 applied to the defined yield stress of laboratory test data is about the right factor for high strain-rate effect, while the factor of 1/4 is about the right scale factor for the poor quality rocks of the PSA Flight 1771 crash site.

Table 4-3 shows the best estimated average material properties as used in the RND29 calculation. Figs. 4-6 and 4-7 compare the best estimate P-V curves with those of laboratory tests on intact specimens. Fig. 4-8 shows how the best-estimate P-V curve does when fitted into a dimensionless plot to derive the characteristic P-V relationship of the outcrop material. Fig. 4-9 shows the difference in stress invariant versus pressure relationship between the best-estimate model and the laboratory test data.

4.4 Modeling Uncertainty

A large source of uncertainty is related to the determination of the model parameters to be used in the analysis. This involves measuring material properties in the laboratory and relating them to the properties in-situ. The uncertainty bounds of the latter is assessed in Section 3.3.4. The present section briefly described the uncertainty bounds for each input parameter from the test data.

The strength data points obtained from unconfined compression tests were analyzed to get the standard deviation and the coefficient of variation (COV). Since the

Table 4-3 **Best estimate of average material parameters and properties of the PSA Flight 1771 crash site for benchmark analysis of penetration tests.**

Layer	Thickness (in.)	ρ ($\times 10^{-4}$)	G ($\times 10^{5}$)	K_u ($\times 10^{5}$)	P_t ($\times 10^{-5}$)	Yield function constants a_0 ($\times 10^{5}$)	a_1 ($\times 10^{3}$)	a_2 ($\times 10^{-3}$)	P-V relationship
1	66	2.19	1.26	5.29	-1.45	2.22	1.05	5.02	Figure 4.6
2	∞	2.19	1.26	4.57	-1.45	1.87	0.79	3.41	Figure 4.7

Notes: ρ = Density in lb-s/in.^{4}

G = Shear modulus in psi.

K_u = Bulk unloading modulus in psi.

P_t = Pressure cutoff for tensile fracture in psi.

Yield function constants are defined on the basis of material type 5 (soil and crushable foam) of the DYNA code. On the yield surface, the model defines $\sigma_y = [3(a_0 + a_1 p + a_2 p^2)]^{1/2}$ where σ_y is the uniaxial yield stress and p is the effective mean pressure. Yield function constants are: a_0 in $(psi)^2$, a_1 in psi, and a_2 without unit.

P - V = Pressures versus volumetric strains as shown in indicated figures.

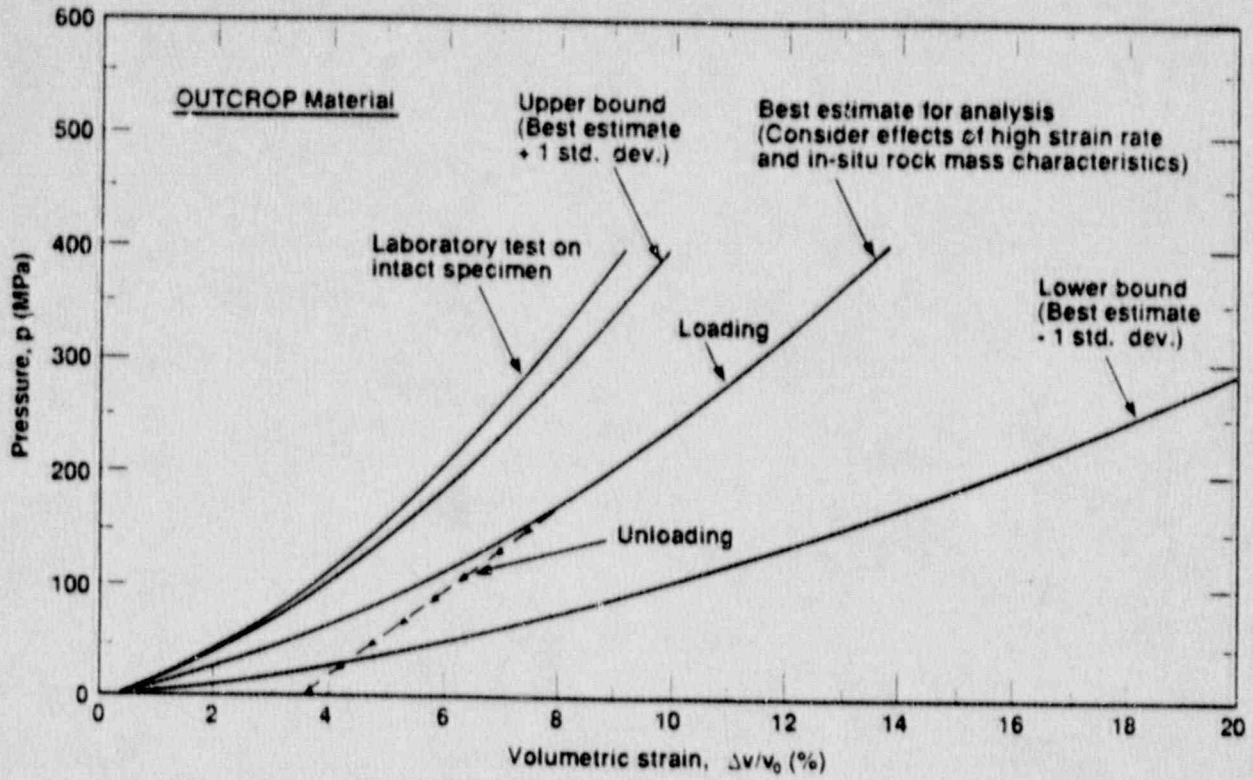

Figure 4-6. Pressure-volumetric strain curves of the best estimate, the upper bound, and the lower bound models together with the laboratory data for the outcrop material.

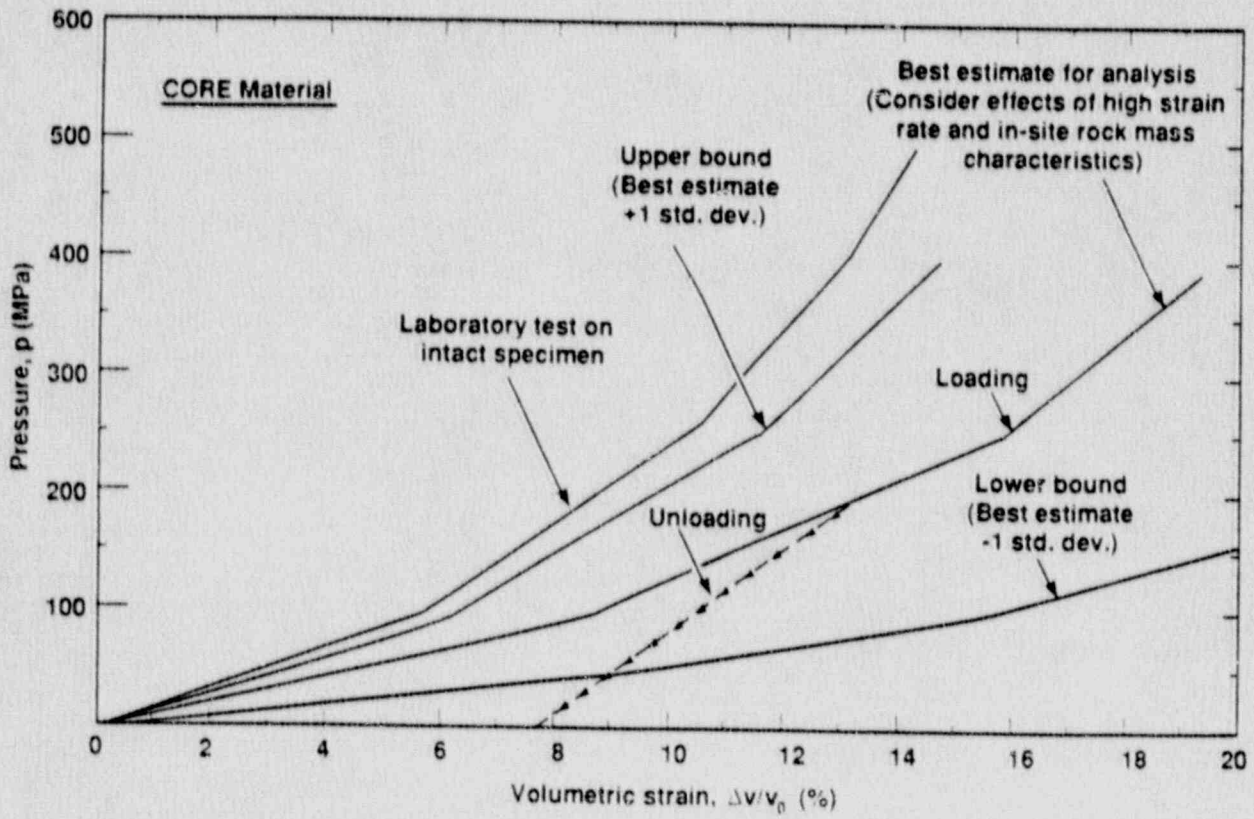

Figure 4-7. Pressure-volumetric strain curves of the best estimate, the upper bound, and the lower bound models together with the laboratory data for the core material.

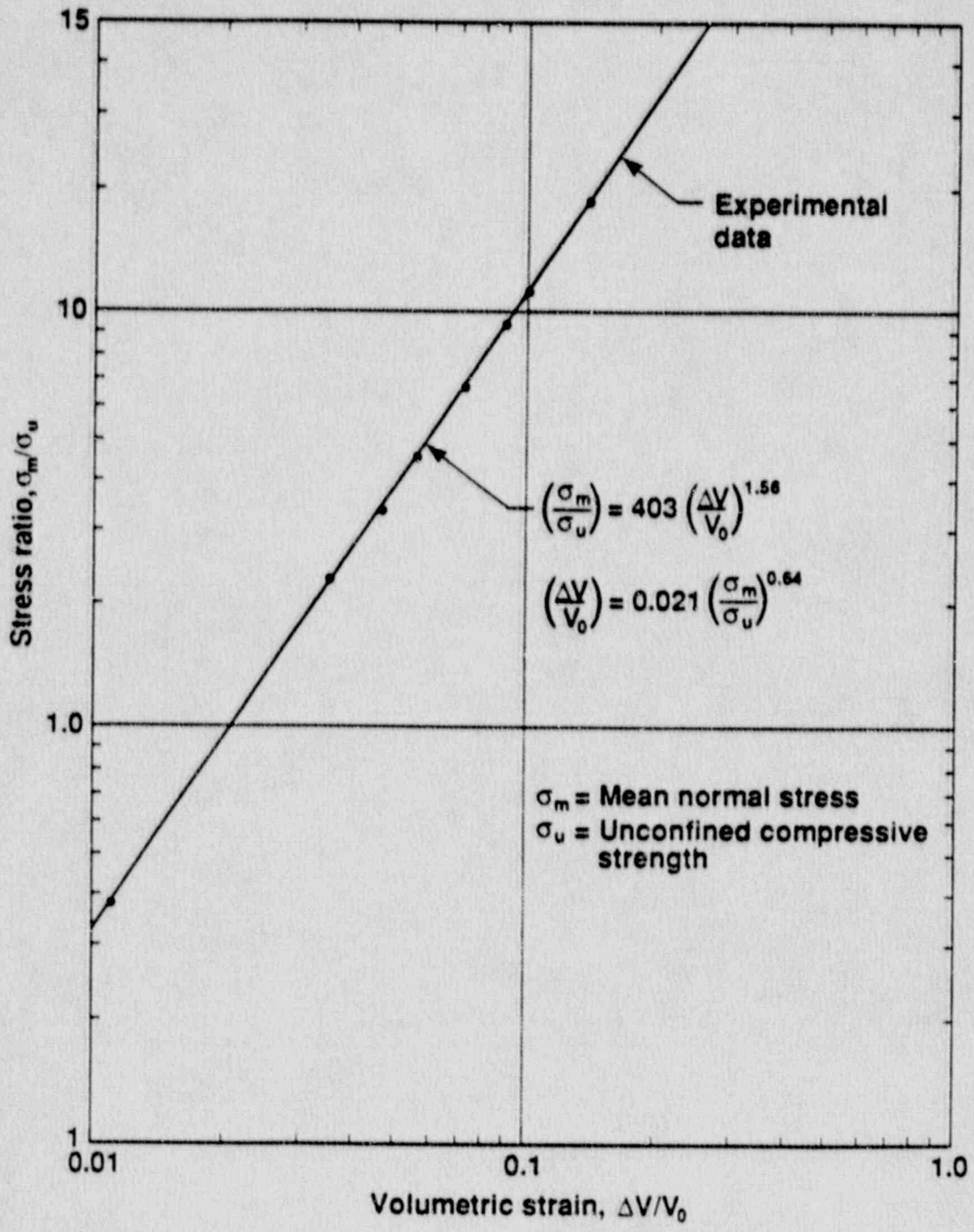

Figure 4-8. The characteristic pressure versus volumetric strain relationship of the outcrop material.

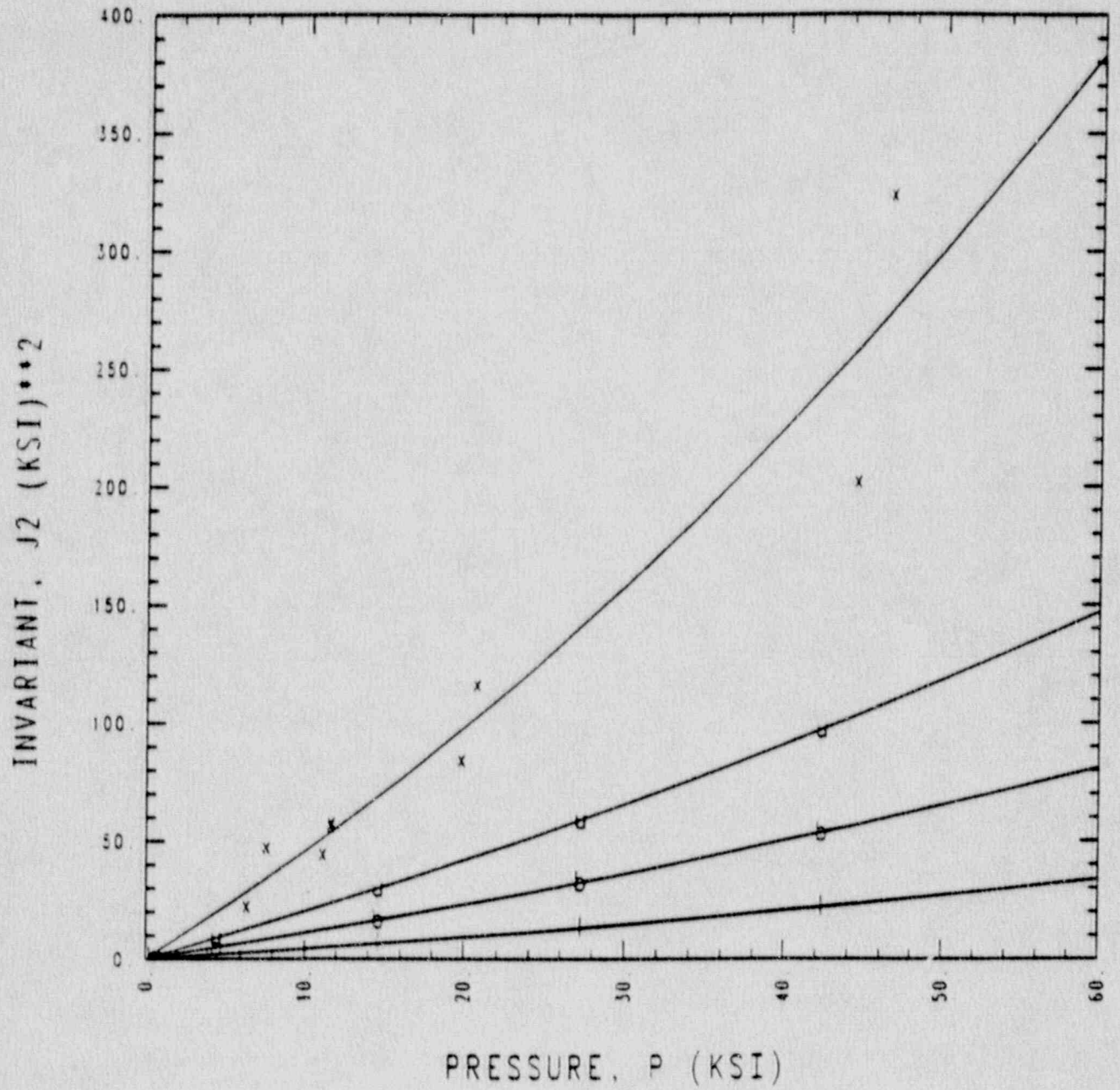

Figure 4-9. Stress invariant, J_2, versus mean pressure curves of the best estimate, the upper bound, and the lower bound models together with the laboratory data for the outcrop material.

strength strongly depends on the confining pressure, one practical way to find the overall standard deviation is to normalize the data points to their mean strength at each confining pressure and then proceed to find the standard deviation on the normalized data. The standard deviation of the normalized strength is about 0.17 which is also the value of COV because the mean value of normalized strength is equal to 1. The actual values of standard deviation at each confining pressure level are obtained by the multiplication of normalized COV to the average mean strength at each confining pressure. Thus the upper and the lower bound of the yield stress may be directly defined by the calculated standard deviation. To find the coefficients of yield function of the upper and lower bound of yield stress, the least square minimization technique as described in Section 3.3.2.3 was applied. The upper bound, the best estimate, and the lower bound of the stress invariants, and the mean normal stress are shown in Fig. 4-9.

The variation of Young's modulus was analyzed based on the laboratory test data shown in Table 3-6. The COV is 43.5%. Thus, to estimate the upper and the lower bound of the P-V curves for the model, we simply scale the best estimate of volumetric strains at each pressure by a factor of (1 ± 0.435). The upper bound, the best estimate, and the lower bound of P-V curves together with the laboratory P-V curve of the intact specimen are shown in Figs. 4-6 and 4-7 for both layers. Since the bulk modulus, the shear modulus of a material are all related through the Poisson's ratio, without specific data available we simply apply the same COV value to estimate the upper and the lower bound of the unloading bulk and shear modulus. As stated previously, the COV of the rock density based on 47 measurements of laboratory specimen is 5.2%.

4.5 Upper and Lower Bound Models

The upper and lower bound models were developed using the COV values of each parameter from test data. The distribution of each parameter can be analyzed or assumed (e.g., lognormal distribution). Once the mean, the COV and the distribution type are given, sets of input parameters can be generated and probabilistic analysis can be conducted using the approach as applied in our previous research project (Ref. 21). However, it is not practical to perform such analysis due to the high expense of nonlinear DYNA calculations. Therefore, we conservatively combined the upper bound parameters together to define the upper bound model. This is a conservative and practical approach and the models may be able to cover a wide range on uncertainty. Tables 4-4 and 4-5 present the parameters and properties of the upper and lower bound models. The calculated average deceleration and penetration depth are shown in Table 4-1.

Table 4-4 Estimated upper-bound material properties of the PSA Flight 1771 crash site for benchmark analysis of penetrator tests.

Layer	Thickness (in.)	ρ (x 10^{-4})	G (x 10^5)	K_u (x 10^5)	P_t (x 10^{-5})	Yield function constants a_0 (x 10^5)	a_1 (x 10^3)	a_2 (x 10^{-3})	P-V Relationship
1	66	2.31	1.81	7.59	-1.45	2.29	1.91	8.92	Figure 4.6
2	∞	2.31	1.81	6.56	-1.45	2.38	1.59	6.64	Figure 4.7

Note: for ρ, G, K_u, P_t, yield function constants, and P-V refer to the notes in Table 4-3.

Table 4-5 Estimated lower-bound material properties of the PSA Flight 1771 crash site for benchmark analysis of penetrator tests.

Layer	Thickness (in.)	ρ (x 10^{-4})	G (x 10^5)	K_u (x 10^5)	P_t (x 10^{-5})	Yield function constants a_0 (x 10^5)	a_1 (x 10^3)	a_2 (x 10^{-3})	P-V Relationship
1	66	2.08	0.71	2.99	-1.45	1.26	0.41	2.62	Figure 4.6
2	∞	2.08	0.71	2.58	-1.45	0.79	0.25	1.61	Figure 4.7

Note: for ρ, G, K_u, P_t, yield function constants, and P-V refer to the notes in Table 4-3.

5.0 DEVELOPMENT OF MODEL PARAMETERS FOR OTHER GEOLOGICAL MATERIALS

In support of the development (controlled) test criteria, an unyielding surface equivalence methodology was developed using results obtained from finite element analysis and from empirical equations of the earth penetrator (Ref. 5). An extensive series of finite element analyses was conducted for specific packages impacting on PSA Flight 1771 crash site and other targets with various hardness (Refs. 5 and 6). Model parameters and geotechnical properties must be given for the analyses. In addition to the PSA Flight 1771 crash site, we selected three other target materials whose geotechnical properties and S-numbers have been published for the development of constitutive models for finite element analysis. The three target materials are:

1) Intensely weathered and fractured granite, S=0.9,
2) Low strength unfractured Antelope tuff, S=1.26,
3) Stiff Antelope Lake soil, S=5.5.

The model parameters for each target material are briefly summarized as follow:

5.1 Intensely weathered and fractured granite

Experimental study on mechanical behavior of dry Westerly granite at confining pressure up to 4 GPa was published by H. C. Heard et al. (Ref. 22). Laboratory tests include pressure-volume, uniaxial stress loading to failure, uniaxial strain, and ultrasonic velocity measurements. The P-V relationship for the Westerly granite was determined to 4 GPa from six tests which included four hydrostatic tests to 114 GPa and two quasi-hydrostatic tests to 4 GPa. The hydrostatic measurements were carried out on 32 mm-diam. by 50 mm-long cylinders jacketed in 0.25 mm copper to prevent penetration of the pressure fluid into granite. Axial and circumferential strains were measured using resistance strain gages bonded to the metal jacket. The average P-V curve from laboratory tests of intact specimens is shown in Fig. 5-1.

The ultimate compressive strength of dry Westerly granite was determined from a series of triaxial compression tests with confining pressure from 0.1 to 700 MPa. The failure envelope drawn through the data points of the maximum shear strength vs confining pressure is a smooth curve. Axial stress vs axial strain curves for all tests showed a quasi-elastic portion followed by a narrow yielding that finally terminated in fracture. Total permanent strains before onset of fracture were about 1 to 2% and tended to increase somewhat with pressure. The mechanism of failure is dependent on normal stress. For confining pressure less than 1.0 GPa, shear failure and fractional sliding of adjacent surfaces are important failure mechanisms. At some higher pressure, plastic flow in the component mineral may occur. We assume that near the ground surface the granite is intensely weathered and fractured as the sandstone in the PSA Flight 1771 crash site. For the purpose of model development,

we used the same scale factor of 1.75/4 to accou nt for scale-fractured and high strain-rate effect. We also applied the same procedure as used in the development of the PSA crash site models for Westerly granite. Fig. 5-2 shows the defined yield stress vs the mean normal stress. The data points shown by a solid dot are actual test data scaled by this factor while the solid line drawn through most of the points is the best fit of the paraboloid-shape yield surface. In the same figure we also show the data of post-fracture strength of Westerly granite (Ref. 20) as well as the data of intensely weathered and fractured sandstone of the PSA Flight 1771 crash site.

The other properties and parameters required for the Model 5 of DYNA analysis are summarized in Table 5-1.

Table 5-1 Geotechnical properties and model parameters of intensely weathered and fractured Westerly granite.

Parameters or Properties	Best estimate or average
* S - Number	0.9
Bulk density (pcf)	164.
* Unloading bulk modulus (psi)	3.21×10^6
* Shear modulus (psi)	1.43×10^6
Poisson's ratio	0.18
Porosity	0.8
Pressure cutoff (psi)	-32.
Yield function constant, a_0 $(psi)^2$	3.333×10^5
Yield function constant, a_1 (psi)	9.805×10^3
Yield function constant, a_2	9.822×10^{-3}

* The factor of 1.75/4 applied for fracture and high strain-rate effect.

5.2 Unfractured Antelope Tuff

Geotechnical properties of Antelope tuff obtained from laboratory test data were summarized by Hightower (Ref. 23). The data provided is a summary of the physical and strength properties of core samples from three borings identified as AT #8, AT #9, and AT #10 from the target site (the Davis Gun test site) near the southern end of the Tonopah Test Range (TTR). The target is welded ash flow tuff. The rock is porous, whiteish-gray in color, and low in strength. The flow is over 25 ft thick and generally unfractured horizontally and vertically.

Fig. 5-3 shows the results of hydrostatic compression tests for the pressure up to 400 MPa. Among the P-V curves, three are from AT#10 at different depths, two from

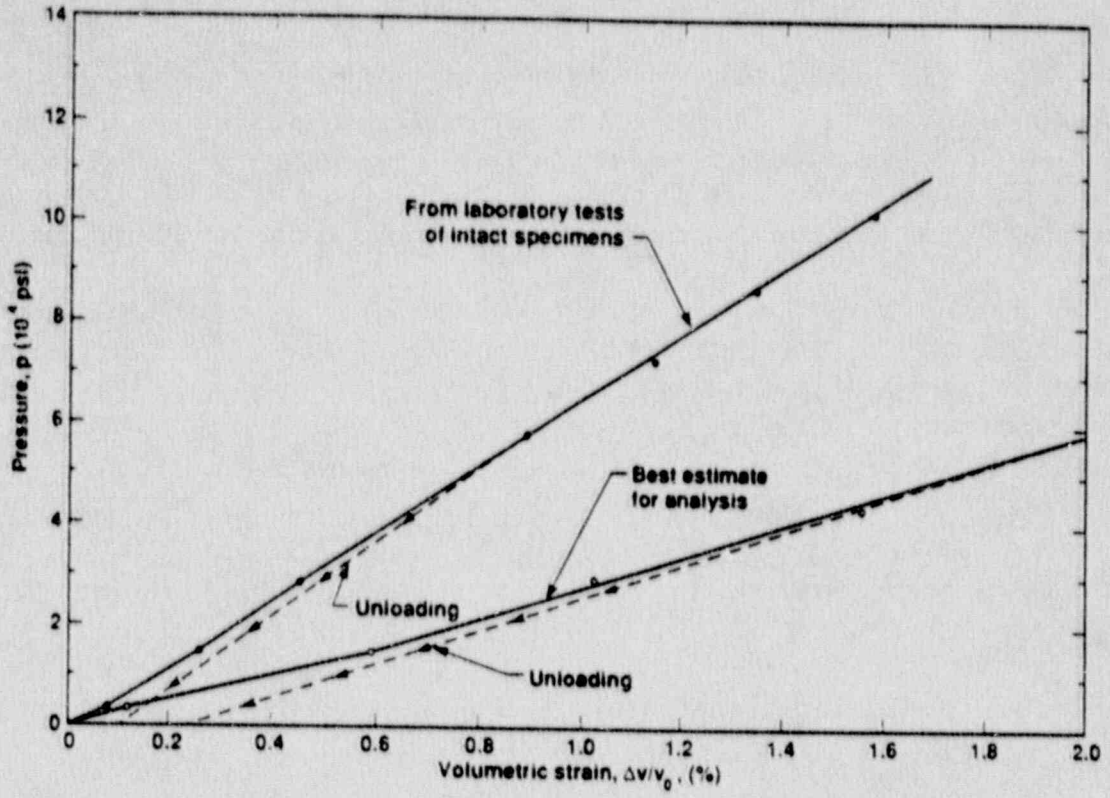

Figure 5-1. Pressure-volumetric strain curves of Westerly granite.

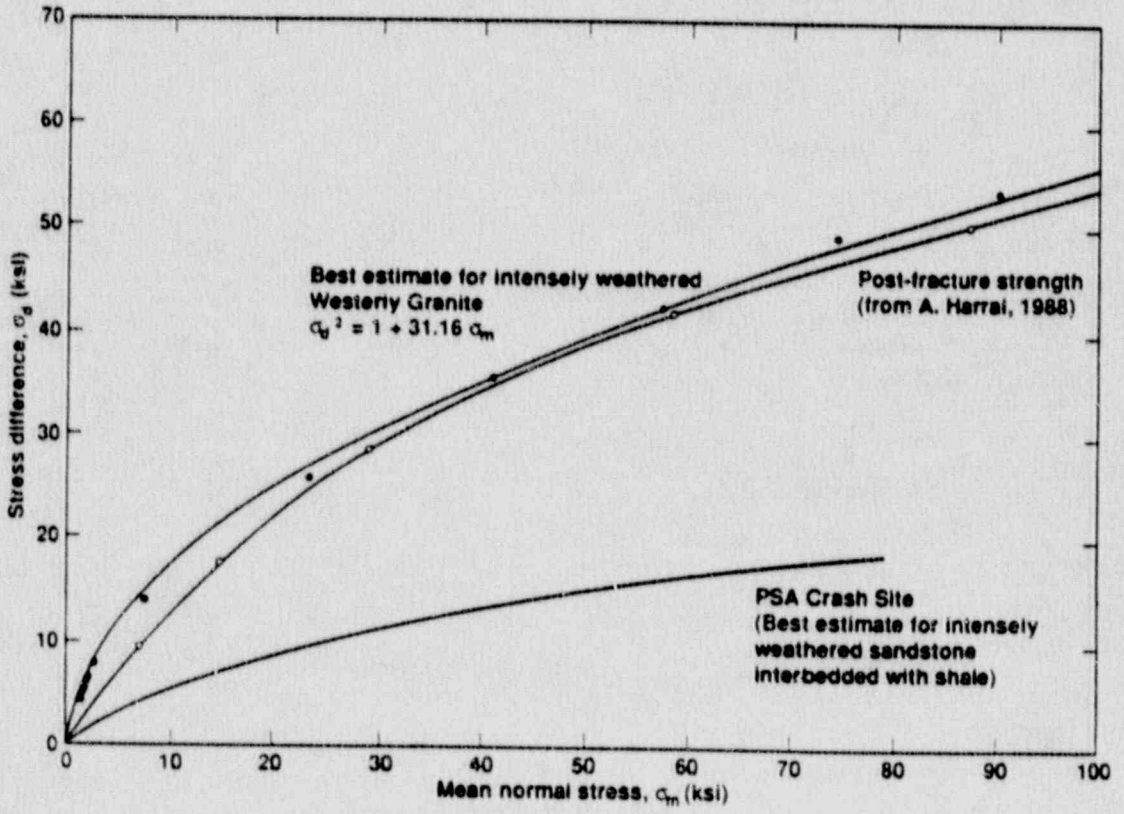

Figure 5-2. Deviatoric stress vs mean normal stress of intensely weathered and fractured Westerly granite.

AT#8, and one from AT#9. The characteristics of the P-V curves among all the tests are somehow similar. The middle curve from AT#8 can be used to represent the overall compressibility of the Antelope tuff. The unloading behaviors of the rock from compression tests (for AT#8) were shown in Ref. 24. The average ratio of unloading and loading bulk modulus for the pressure up to 200 MPa is about 2.2.

The triaxial compression test on samples from AT#8 were conducted for confining pressures 133 MPa, 266 MPa and 325 MPa. There are two tests for each confining pressure. In addition, three unconfined compression tests were also conducted. The failure surface is defined by the ultimate strength of each test. Fig. 5-4 shows the test data and their best fit for the failure surface. From the best fit curve, it is easy to find that the cohesive strength τ_o, is about 1.67 ksi and the slope of the curve, μ, is 0.96.

The other geotechnical properties and model parameters are shown in Table 5-2.

Table 5-2 Geotechnical properties and model parameter of unfractured Antelope Tuff.

Parameters or Properties	Best estimate or average
S - Number	1.25
Bulk density (pcf)	107.3
Water content (%)	<2.0
Unloading bulk modulus (psi)	6.2×10^5
Shear modulus (psi)	1.91×10^5
Poisson's ratio	0.18
Porosity (%)	33.0
Pressure cutoff (psi)	-80.
Yield function constant, a_0 $(psi)^2$	9.30×10^5
Yield function constant, a_1 (psi)	1.11×10^3
Yield function constant, a_2	0.31
Unconfined shear strength (psi)	2400

5.3 Stiff Antelope Lake Soil

The geotechnical properties of Antelope Lake soil were investigated and published in Ref. 25. Soil samples were taken from a boring hole in Antelope Lake, Tonopah Test Range, Tonopah, Nevada. Laboratory tests were performed on soil samples to evaluate their behavior and strength characteristics at confining pressure varying

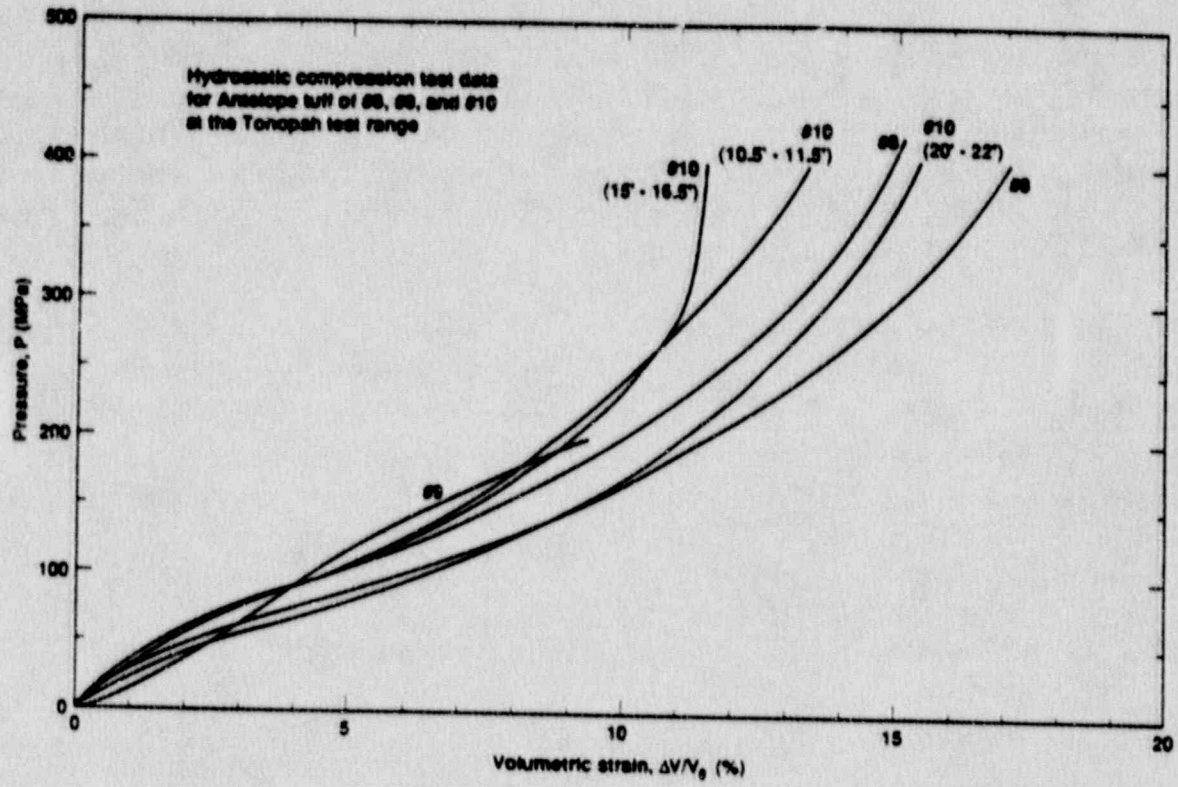

Figure 5-3. Pressure-volumetric strain curves of unfractured Antelope Lake tuff.

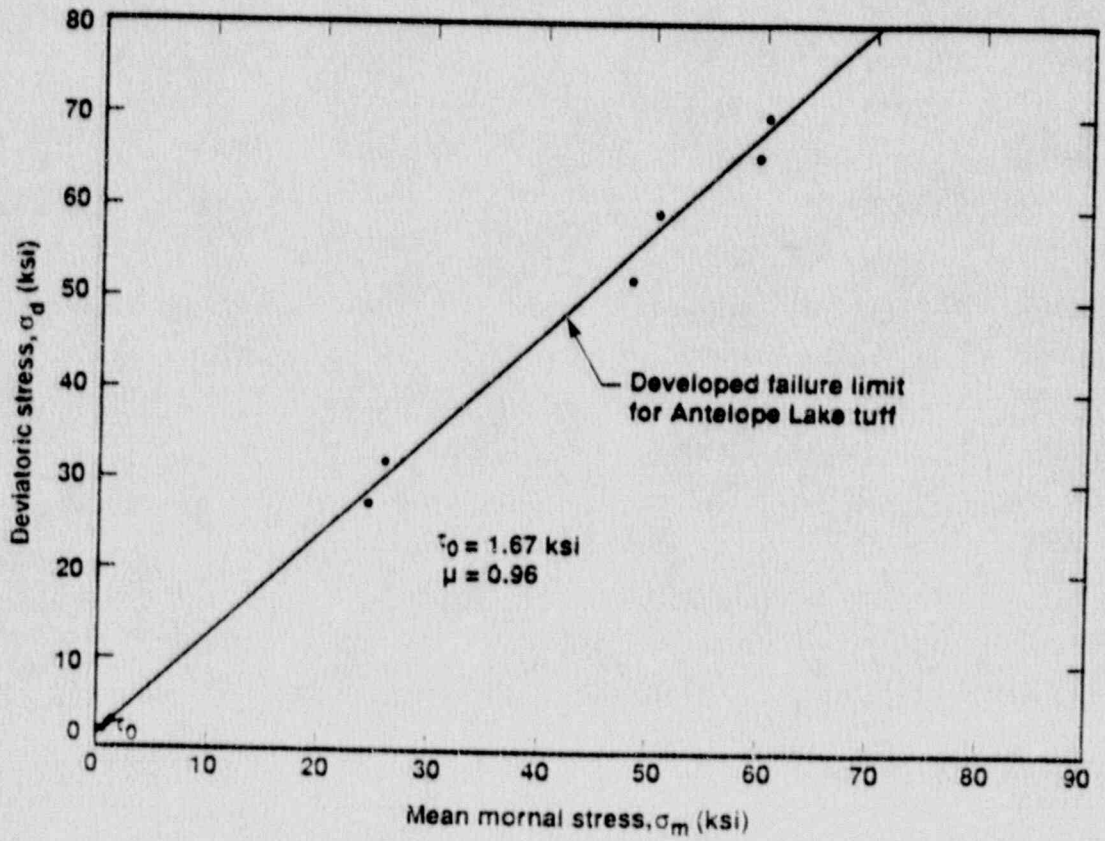

Figure 5-4. Deviatoric stress vs mean normal stress of unfractured Antelope Lake tuff.

from near those experienced by the soil at its sample location to 550 bars, and loading rates ranging from approximately 20 in/min to .016 in/min. The test hole showed the site consisting of very stiff silty clays over very dense, slightly sandy silts with occasionally gravelly sands. Additional laboratory test data were also given in Ref. 26 in which the data of 6 static unconfined compression tests and 12 static triaxial tests were reported.

Fig. 5-5 shows the best estimate of P-V curve from hydrostatic compression tests presented in Ref. 26. There is no P-V data given in Ref. 25. Fig. 5-6 shows the failure limit of the soil based on the ultimate strength of compression tests. The straight line fits the data points best. The cohesive strength, τ_o, is about 100 psi and the slope of the surface, μ, is 0.27. The yield function constants, a_o, a_1, and a_3 are calculated based on the formula given in section 3.3.2.1. The other geotechnical properties and model parameters are shown in Table 5-3.

Table 5-3 Geotechnical properties and model parameters of stiff Antelope Lake soil.

Parameters or Properties	Best estimate or average
S-Number	5.6
Bulk density (pcf)	117
Water content (%)	18.6
Unloading bulk modulus (psi)	2.21×10^5
Shear modulus (psi)	5.0×10^4
Poisson's ratio	0.35
Pressure cutoff (psi)	-20.
Yield function constant, a_0 $(psi)^2$	3.33×10^3
Yield function constant, a_1 (psi)	18.0
Yield function constant, a_2	0.024
Unconfined shear strength (psi)	84.0

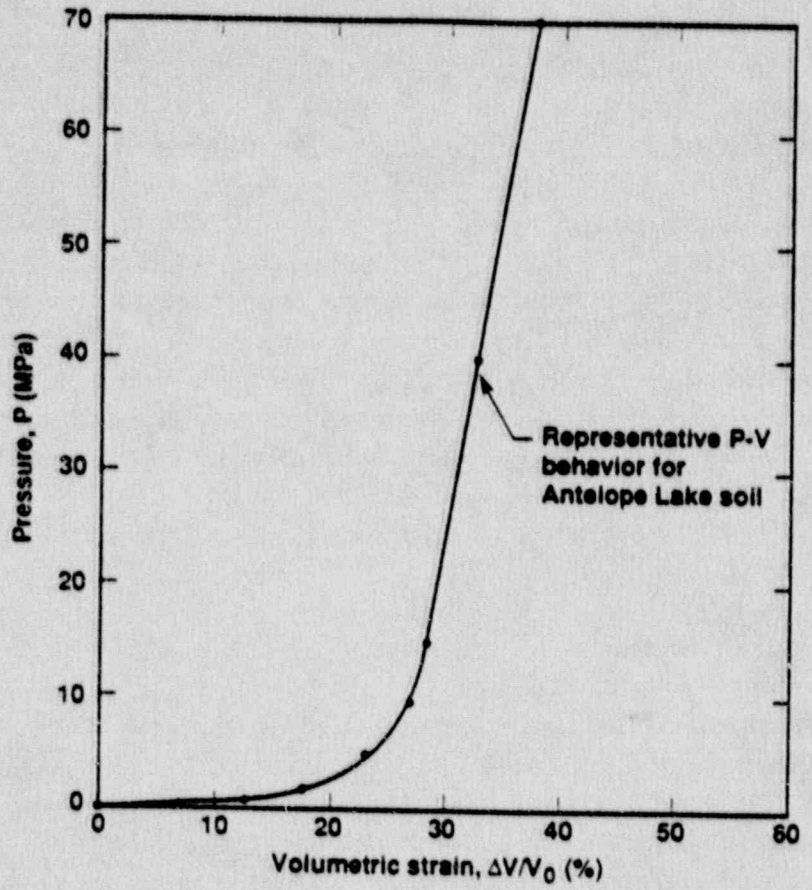

Figure 5-5. Pressure-volumetric strain curve of stiff Antelope Lake soil.

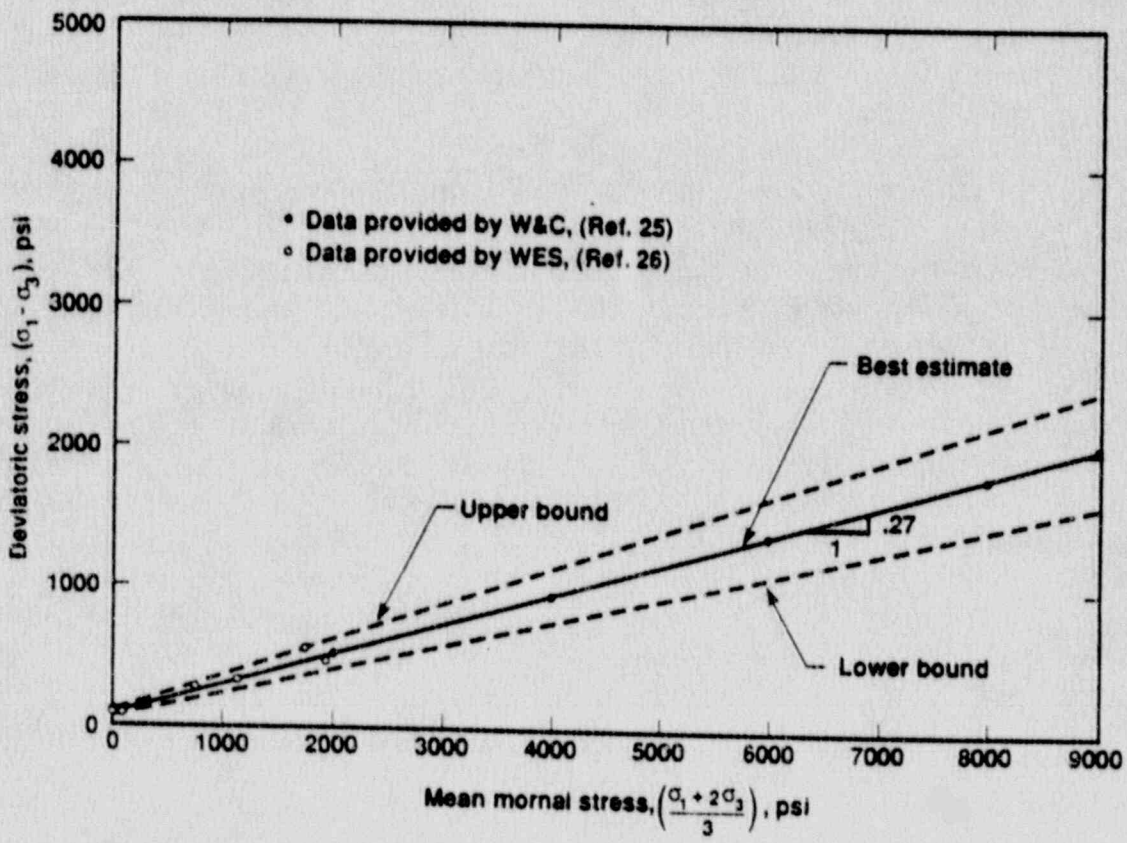

Figure 5-6. Deviatoric stress vs mean normal stress of Antelope Lake soil.

6. SUMMARY AND CONCLUSIONS

Section 5062 of Public Law 100-203 concerns the safety of plutonium containers transported by air through United States airspace. In response to this law, the U.S. NRC established a program for certifying plutonium air transport packages. The law requires certain tests to be conducted as part of the certification process. These tests include a drop test of the package and a crash test of the cargo aircraft with test packages aboard to replicate actual worst-case aircraft accident conditions. In lieu of the aircraft crash test, package development (controlled) tests may be substituted, provided that the stresses produced by development tests exceed the stresses produced by a worst-case accident. The NRC specified that the conditions associated with the crash of PSA Flight 1771 on December 7, 1987 represent a worst-case aircraft accident and are therefore suitable for use as the basis for conducting the required tests.

In order to assure adequacy of testing, the site characteristics and constitutive properties of the geological materials at the PSA Flight 1771 crash site were evaluated in support of the development of crash site criteria for the aircraft crash test. Field investigations consisted of topography surveys, exploratory borings, seismic refraction measurements, and dynamic penetration tests. Laboratory tests measured the basic engineering properties, compressibility characteristics, and stress-strain behaviors of the soil/rock samples. Dynamic penetration tests provided the data (e.g., S-number) for the characterization of the site under the condition of high-velocity impact. The measured deceleration responses and penetration depths were used as a benchmark to determine the most suitable constitutive properties of the PSA Flight 1771 crash site. These constitutive properties were used for conducting finite element analyses in support of draft criteria for development (controlled) package tests.

PSA Flight 1771 crashed near the top of a hillside at an approximate elevation of 403 m above mean sea level. The slope gradients of the hill vary from 20% to 40% in the vicinity of the impact point. The site consists of a thin layer (0.2 m to 0.6 m) of colluvial deposits overlying a formation of sedimentary rocks. The rocks consist primarily of interbedded clay shales and silty sandstones, with occasional seams of siltstone and claystone. The upper portion of the rock formation has been decomposed through weathering to a residual soil condition. The remainder of the rock formation graded with depth from intensely weathered to unweathered. As a result of past tectonic activity, rock in the vicinity of the crash site has been intensely fractured and sheared.

The engineering soil/rock properties, including compressibility characteristics and stress-strain behaviors, were determined by various laboratory tests. The soil/rock properties include bulk density, moisture content, porosity, shear modulus, bulk modulus, and Poisson's ratio. The average penetrability constant (S-number) of the soil is about 3.4 ± 0.3. Changes of soil density and intergranular effective stress are controlled by the volumetric compressibility characteristics of soils and by the degree

of saturation existing in the soil at the time of the crash. For impact-crash analysis the volumetric compressibility curve at various depths in the soil profile and the variation of undrained shear strength with depth were developed. The failure surface of the soils was modeled as cone-shaped with the slope of failure surface of 0.37.

The overall seismic shear and compressional wave-velocities in the upper 15 m of the site were measured by a seismic downhole survey. In the upper 4.6 m of intensely weathered rock layers, the average shear wave velocity was 610 m/s and the average compressional wave velocity was 1320 m/s. The average penetrability constant of the rock is about 2.5 $\pm$ 0.5. Pressure-volumetric tests were conducted to determine the change of bulk modulus with pressure of the intact rock samples and to investigate the unloading behaviors. During the first stage of loading up to 70 MPa, the crack and large void in the material was closed. From the loading stage of 70 MPa to 250 MPa, the pore voids collapsed and the material was more compacted. For pressure above 250 MPa, the material was in grain-to-grain constact and was eventually crushed. The compressive strengths were determined by unconfined and triaxial compressional tests up to a maximum confining pressure of 500 MPa. The rock samples tested at low confining pressure or unconfined condition fail in a brittle manner when the stress state reaches its ultimate strength. On the other hand, the samples tested at pressures of 100 MPa and above show ductile strain-hardening behavior, with compressive strength increasing with strain at high pressures. The strength data of the compressional tests were used to develop the yield and failure surfaces of the material.

The development of the model parameters is based on evaluation of data obtained from laboratory tests and in-situ measurements. However, the nature of the geological discontinuities and fractures within the zone of influence significantly affect the determination of the strength and the compressibility of the rock mass. The nature of loading condition due to the high velocity impact can also significantly change impact response. These two effects were assessed through literature review for similar geological materials. The overall strength and deformation modulus of the in-situ fracture rocks are only about 25% to 50% of those obtained by laboratory tests of intact samples. The review also indicates that the strength could increase from 1.3 to 2.6 times from static loading to impact loading. Most of the data show that the strength factor increases in the range between 1.5 and 1.8. From static to dynamic impact load conditions, a factor of increase in modulus between 1.3 to 2.0 is observed. The effects of the field condition (scale-fracture effect) and loading condition (strain-rate effect) were considered and explicitly included in model development. The effect of the PSA Flight 1771 crash on geological material beneath the site is minor. The densification of soil/rock materials by the PSA Flight 1771 accident was not considered in the development of constitutive models.

A large source of uncertainty is related to the determination of the model parameters used in the analysis. This involves measuring material properties in

the laboratory and relating them to the properties in-situ. The variation of compressive strength, deformation modulus and density was evaluated for the development of the upper and lower bound models. The values of COV are: 0.17 for normalized strength, 0.44 for deformation modulus, and 0.05 for density. The upper bound parameters were combined to define the upper bound model. This is a conservative and practical approach, and the model may be capable of covering a wide range of uncertainty.

Four gas-gun penetration tests conducted at the PSA Flight 1771 crash site provided valuable experimental data that can be used as benchmarks to determine the most suitable constitutive properties of the site. The comparison of the calculation results with the experimental data led to the selection of the best estimate model. The calculation results of the best estimate model compare reasonably well with the measured data. The difference between the calculated and the measured value of the penetration depth is within 5%. The calculated average response acceleration is 19% higher than the measured average value within the first 5 ms. Excellent agreement is observed between 5 and 10 ms. For later response (>10 ms), the calculated average deceleration is 24% smaller than the measured value. Furthermore, the general shapes of the calculated time histories of acceleration, velocity, and displacement compare reasonably well with those of the experimental data. The sensitivity study indicates that the most sensitive model parameter is the defined yield (or failure) surface function. The shear modulus and bulk unloading modulus are also important. The calculation results are not very sensitive to scale changes in the P-V curve.

It is difficult to accurately model intensely weathered and fractured rocks for impact analysis; also, there is a discrepancy between the real situtation and the numerical model (i.e., 2D vs 3D, normal vs slightly inclined penetration). Even so, the comparison of the calculation results with experimental data reveals that the developed constitutive properties reasonably represent the material properties of the PSA Flight 1771 crash site under the high velocity impact condition. The constitutive properties of the best estimate model are suitable for conducting crash-impact analyses in support of appropriate development (controlled) tests for the design of PAT packages that meet requirements to be established.

Three target materials whose soil constants and geotechnical properties have been published were used for the development of constitutive properties for DYNA analyses. These analysis results were used in support of the development of a methodology for establishing the equivalence between impact velocity of a package on an arbitrary surface and an unyielding surface.

7. REFERENCES

1. C. E. Walter, J. H. VanSant, and C. K. Chou, *Draft Criteria for Package Drop and Aircraft Crash Tests*, Lawrence Livermore National Laboratory, Livermore, CA, UCID-21697, (June, 1989).

2. C. W. Young, Sandia National Laboratory, Albuquerque, NM, letter with data report by V. P. Salazar et al. to J. C. Chen, (June 16, 1989).

3 J. O. Hallquist, *User's Manual for DYNA2D—An Explicit Two-dimensional Hydrodynamic Finite Element Code with Interactive Rezoning and Graphical Display*, Lawrence Livermore National Laboratory, Livermore, CA, UCID-18756, Rev. 3 (March 1988).

4. J. O. Hallquist, *DYNA3D User's Manual (Nonlinear Dynamic Analysis of Structures in Three Dimensions)*, Lawrence Livermore National Laboratory, Livermore, CA, UCID-19592, Rev. 4 (April 1988).

5. T. F. Chen, *The Mechanical Response to Impact of a Representative Package*, Lawrence Livermore National Laboratory, Livermore, CA, PATC-IR 90-03, (June, 1990).

6 M. C. Witte, *Structural Impact Analyses*, Lawrence Livermore National Laboratory, Livermore, CA, PATC-IR-89-11, (April 1990).

7. D. W. Carpenter, J. C. Chen, and G. S. Holman, *An Engineering Geologic Evaluation of the PSA Flight 1771 Crash Site Near Paso Robles, California*, Lawrence Livermore National Laboratory, Livermore, CA, PATC-IR 89-04, (October 1989).

8. C. W. Young, *The Development of Empirical Equations for Predicting Depth of an Earth-Penetrating Projectile*, Sandia National Laboratories, Albuquerque, NM, SC-DR-67-60 (May 1967).

9. C. W. Young, *Depth Prediction for Earth-Penetrating Projectiles*, Journal of Soil Mechanics and Foundations Division, Proc. Am, Civil Engineers, pp. 803 (May 1969).

10. C. W. Young, *Empirical Equations for Predicting Penetration Performance in Layered Earth Material for Complex Penetrator Configurations*, Sandia National Laboratories, Albuquerque, NM, SC-DR-72-0523 (December 1972).

11. C. W. Young, *Equations for Predicting Earth Penetration by Projectiles: An Update*, Sandia National Laboratories Report SAND 88-0013, Advanced Projects Division II, Sandia National Laboratories, Albuquerque, NM (July 1988).

12. R.W. Rosinsky, *Lagrangen Finite Element Analysis of the Earth Penetration Weapon*, Lawrence Livermore National Laboratory, Livermore, CA, UCID 20836 (November 1985).

13. R. D. Krieg, *A Simple Constitutive Description for Cellular Concrete*, Report Sandia National Laboratories, Albuquerque, NM, SC-DR-72-0883 (1972).

14. S. J. Sackett, "Geological/Concrete Model Development," private communication, Lawrence Livermore National Laboratory, Livermore, CA, (1987).

15. J. C. Simo, J. W. Ju, K. S. Pister, and R. L. Taylor, *Softening Response, Completeness Condition, and Numerical Algorithms for Cap Model*, Intl. Journal Numer. Analy. Math. Eng. (1988).

16. M. L. Chiesa, *Stress Analysis of Penetrator Cases Upon Ground Impact*, Sandia National Laboratories, Livermore, CA, Proc. of the Earth Penetration Phenomenology Meeting, U.S. Army Engineer Waterways Experiment Station, Vicksburg, MS (April 1988).

17. C. Y. Chang, J. C. Egan, and J. C. Chen, *Constitutive Models and Dynamic Behavior of Soils Under Impact Loading Conditions*, Lawrence Livermore National Laboratory, CA, PATC-IR 89-06 (December 1989).

18. E. L. Wilson, *CAL 78–A Computer Analysis Language for Teaching Structure Analysis*, Structural Engineering and Structural Mechanics, Dept. of Civil Engineering, U. C. Berkeley, Report UC SESM 79-1 (1978).

19. S. C. Blair, J. C. Chen, W. R. Ralph and D. W. Ruddle, *Mechanical Properties of Rocks from PSA Flight 1771 Crash Site*, Lawrence Livermore National Laboratory, Livermore, CA, PATC-IR 89-05 (December 1989).

20. A. Harral, *Finite-Element Simulation of Earth Impact*, Lawrence Livermore National Laboratory, Livermore, CA, Proc. of the Earth Penetration Phenomenology Meeting, U.S. Army Engr. Waterways Experiment Station, Vicksburg, MS (April, 1988).

21. J. J. Johnson, G. L. Goudreau, S. E. Bumpus, and O. R. Maslenikov, *SMACS-Seismic Methodology Analysis Chain with Statics*, Lawrence Livermore National Laboratory, Livermore, CA, NURGG/CR-2015, 9, UCRL-53201, 9, (September 1981).

22. H. C. Heard, A. E. Abey, B. P. Bonner, and R. N. Schock, *Mechanical Behavior of Dry Westerly Granite*, Lawrence Livermore National Laboratory, Livermore, CA, UCRL-51642, (September 1974).

23. M. Hightower, Penetration Benchmark Calculation Information, Appendix A, Memo March 16, 1987, Sandia National Laboratories, Albuquerque, NM, (March 1987).

24. C. H. Cooley, Testing of Antelope Tuff AT#8, letter report from TeraTek Research, Salt Lake City, Utah to N. Yelamanchili of Holmes & Narver, Inc., Mercury, NV (August 1979).

25. Woodward-Clyde Consultants, Additional Geotechnical Service, Tonopah Test Range, Tonopah, Nevada, Report prepared for Sandia National Laboratories, Albuquerque, NM, Job No. 19805-6762, (March 1980).

26. S. A. Akers, Mechanical Properties of Antelope Lake Soils, Waterways Experiment Station, Corps of Engineers, Vicksburg, Mississippi, SL-86-41, (November 1986).

APPENDIX A

LITERATURE REVIEW ON SCALE-FRACTURE AND STRAIN-RATE EFFECTS

During development of the best-estimate model we conducted an extensive literature review to assess the effects of field condition (scale-fracture effect) and loading condition (high strain-rate effect) on the response of a penetrator at impact.

1. Scale-fracture effect

Certain patterns of joints and fractures in a rock mass may be formed due to the long-term process of weathering near the surface zone or shearing in the fault zone. These joints and fractures reduce the effective strength of the rock mass to a value much below the strength of the intact rock. The situation could induce great model difficulty and uncertainty. Several experiments have been conducted to investigate the effect of fracture on both the strength and the modulus of rock specimens. Fig. A-1, from J. M. Raphael and R. E. Goodman (Ref. A-1) shows shear test results on highly fractured greywacke sandstone. Even though the core was fractured, specimens were prepared for triaxial tests by carefully fitting pieces of core together. The envelope of peak triaxial compressive strength of the fractured rock is lower than the envelope of compressive strength of intact rock. The ratio of the peak strengths of fractured rock to intact rock is about 60%. After the triaxial post-peak stages, the residual strength is about 30% of the ultimate strength of intact rock. Similar studies performed by the U.S. Corps of Engineers for quartz Monzonite (see Ref. A-2) are shown in Fig. A-2. The ultimate shear strength is quite different for intact cores, natural jointed cores, and sawed specimens. At the normal stress of 41 MPa (6 ksi), the ultimate shear strength of cores with natural open joints is about 32% that of intact cores. The strength drops to about 21% for a core with sawed joints.

Extensive experiments were also conducted to investigate the effect of specimen size on the mechanical properties of rock. In-situ uniaxial compression tests were conducted by H. R. Pratt, et al. (Ref. A-3) on specimens of quartz diorite and granodiorite ranging from 0.3 m to 2.7 m (1.0 ft to 9.0 ft) in length; laboratory tests were conducted on specimens ranging from 8 cm to 30.5 cm (3.2 in. to 1.0 ft) in length. These test results, together with those of W. S. Brown and S. R. Swanson (Ref. A-4) are shown in Fig. A-3. As can be seen in this figure, no further decrease in strength was observed when the specimen length exceeded about 0.5 m (1.5 ft). The variation of strength among in-situ tests is not important, but a strong variation from laboratory test data is observed. The ratio of average strength between in-situ tests and laboratory tests is about 1 to 4.

The modulus of elasticity of the intact rock specimens obtained from laboratory tests is always larger than the modulus determined from the large-scale field tests. The

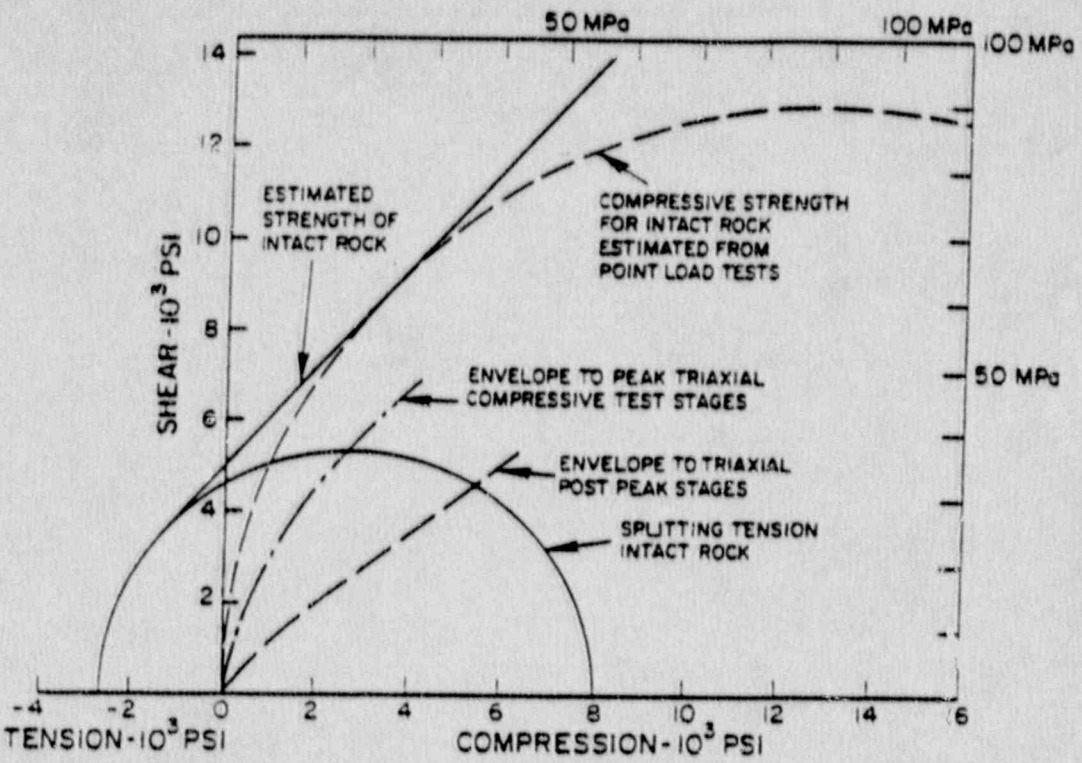

Figure A-1. Comparison of shear strength between the intact and highly fractured greywacke sandstone. (Ref. A-1)

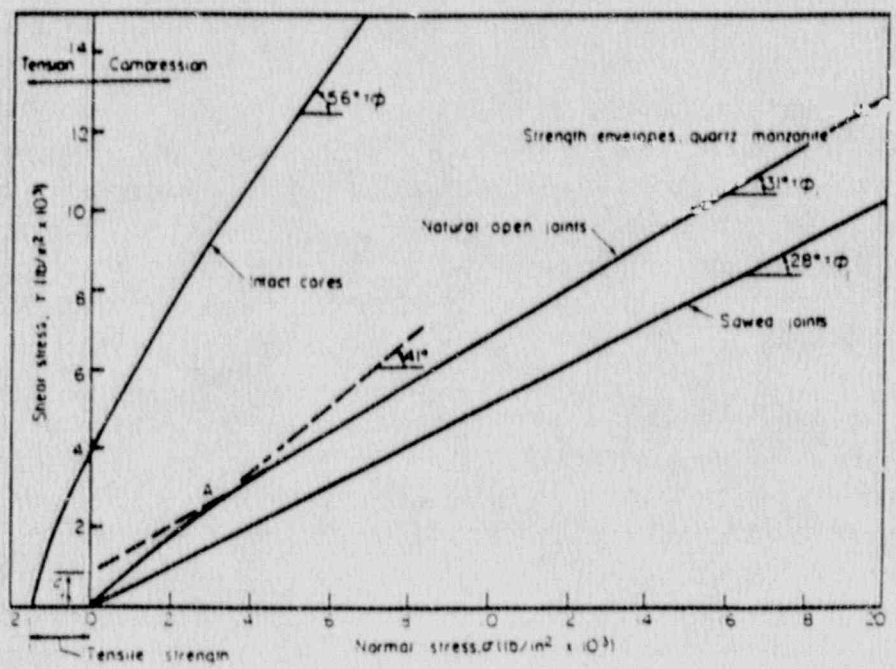

Figure A-2. Comparison of shear strength among the intact core, natural jointed core, and sawed joint specimen of quartz monzonite. (Ref. A-2)

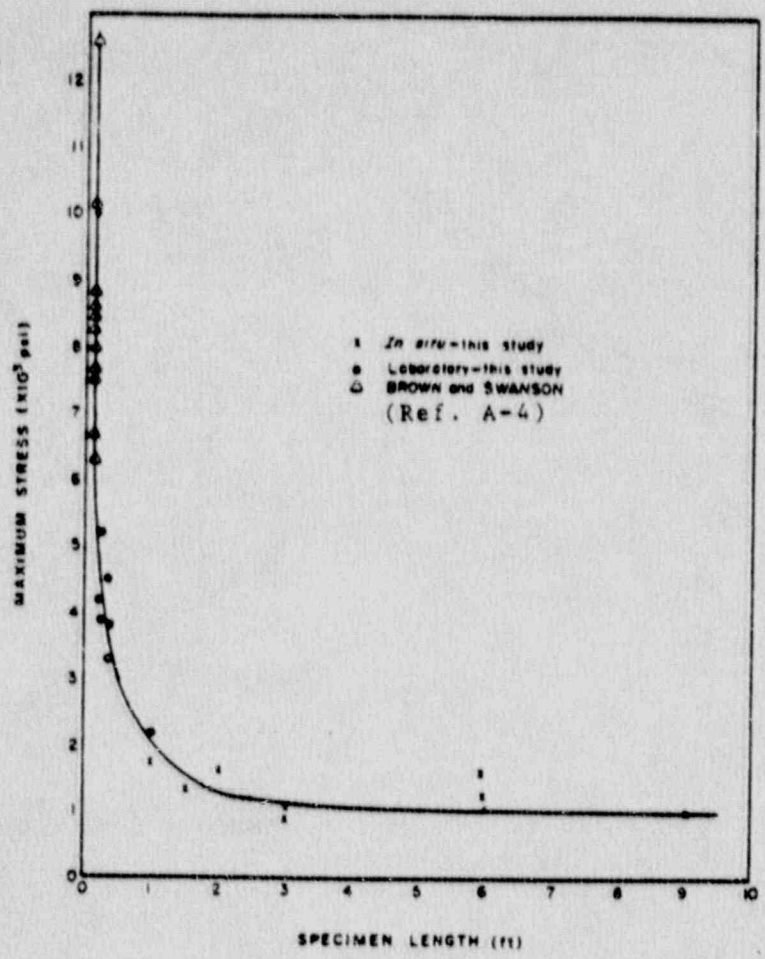

Figure A-3. Effect of specimen size on unjointed diorite. (Ref. A-3)

deformation modulus of the intact rock specimens establishes an upper bound for the modulus of the rock mass for the case in which the joints or fractures are widely spaced. As the rock mass is severely fractured, the deformation modulus of the rock mass is reduced to a smaller fraction of the deformation modulus determined from laboratory specimens. The ratio of the deformation modulus measured in the field to the deformation modulus measured on intact specimens in a laboratory is termed the modulus reduction factor.

Many investigators have published this type of data from large rock testing projects. Z. T. Bieniawski (Ref. A-5) summarized results from 17 rock testing projects. F. E. Heuze (Ref. A-6) conducted an extensive literature search for this type of data and summarized additional results from 11 large rock-testing projects. After combining all the test data, Heuze analyzed the values of modulus reduction factors according to the class of rock and the type of test, as shown in Tables A-1 and A-2. In either grouping, the average ratio is 0.38 to 0.39. Thus, modulus values measured in the laboratory are, on the average, 2.5 times higher than values measured in most field-tests for all rock types. In 1980, Heuze updated the data and cited an additional 24 test results. The values of the mean and standard deviation fall into the range of the previous data.

Table A-1 Ratios of E_F/E_L for the three rock classes (Ref. A-6).

Rock class	No. of results	Mean	Std. dev.
Igneous	15	0.35	0.16
Metamorphics	41	0.36	0.23
Sedimentaries	22	0.42	0.26

Table A-2 Ratios of E_F/E_L for various types of field deformability tests (Ref. A-6).

Type of test	No. of results	Mean	Std. dev.
Plate bearing	27	0.32	0.26
Full scale deformation	14	0.44	0.26
Plate jacks	10	0.54	0.27
Borehold jack or dilatometer	9	0.33	0.17
Pressure chamber	8	0.45	0.22
Petite seismique	5	0.34	0.05
Others	5	0.42	0.14

It should be noted that the modulus reduction factor of the rock mass should be dependent upon the in-situ rock quality. The value of the reduction factor will normally decrease as the quality of the rock mass decreases. A comparison of rock mass quality designation (RQD) and field deformation modulus (E_F) was made using data of 24 vertical and horizontal plate jack tests performed at Dworshak Dam Site (Ref. A-7). The test site is located in a high-strength granite gneiss of excellent rock mass quality. One group of measurements from the field tests was made on the rock surface and another group of measurements was made from approximately 0.3 m or 0.6 m to 5.5 m (1 ft or 2 ft to 18 ft) beneath the surface. An Nx, size core (5.4-cm diameter), was taken to a depth of 6.1 m (20 ft) beneath the surface at each plate-test location. Unconfined compression tests were performed on intact core specimens to determine laboratory modulus (E_L), and RQD was assessed from cores taken.

Variations in the modulus reduction factor, E_F/E_L, were a function of rock fracture, and not dependent on intact properties. The intact modulus, E_L, was approximately 62 GPa (9×10^6 psi), and it did not vary greatly across the site. It can be seen from the figure that the deformation modulus determined from the buried gauges was consistently higher than the modulus obtained from surface gauges. This fact indicated that rock near the surface has been weathered and had more fracture, even though the granite gneiss was an excellent quality rock. It is apparent that most modulus ratios on the surface area range between 10% to 60%.

Test data from 10 other sites were combined to this specific site (Ref. A-7). Fig. A-4 shows modulus reduction factors expressed by E_F/E_{seis} versus the rock quality factors given in terms of the square of the velocity ratio $(V_F/V_L)^2$. The velocity ratio V_F/V_L where V_F and V_L are the compressional wave velocities of the rock mass in-situ and of the intact specimen, respectively, was shown to be equivalent to RQD.

The field seismic modulus E_{seis}, is obtained from the field seismic velocity measurement of the site. A highly fractured or weathered rock will exhibit a lower velocity than will a sound rock mass. The field seismic modulus, E_{seis} ,is always higher than the static deformation modulus determined by plate-bearing tests because the seismic pulse is of a very short duration and low-stress level. It can be seen that the reduction factor falls off very sharply as the rock-quality factor decreases from 100% to about 60%. A further decrease in the rock quality factor is not accompanied by a further decrease in the modulus reduction factor. The data show that, for very poor quality rocks such as those at the PSA Flight 1771 crash site, the modulus reduction factor is about 20%.

We conclude from this extensive review of the published data that for modeling purposes, the deformation modulus obtained from laboratory tests on intact specimens should be reduced to about 20% to 50% of its laboratory value.

2. Strain-rate effect

The constitutive relation described in Section 3.3.1 of this report does not, consider internally, the strain-rate effect in the model. It is therefore necessary to include the strain-rate effect explicitly through the model parameters input to the DYNA code. Our laboratory tests (Ref. 19 of this report) of intact specimens of the geological materials from the PSA Flight 1771 crash site show that compression tests with a high strain-rate do increase the strength and modulus as compared to those with a low strain-rate. However, due to the restriction of testing equipment, the strain-rates examined only increased from 10^{-4}/s to 20/s. The increase of strain-rate from our tests is far smaller than the expected strain-rate induced by a high velocity impact load such as an aircraft crash or package drop. Because of these factors, we also conducted an extensive review to assess the effect of a high strain-rate on the compressive strength and deformation modulus of geological materials.

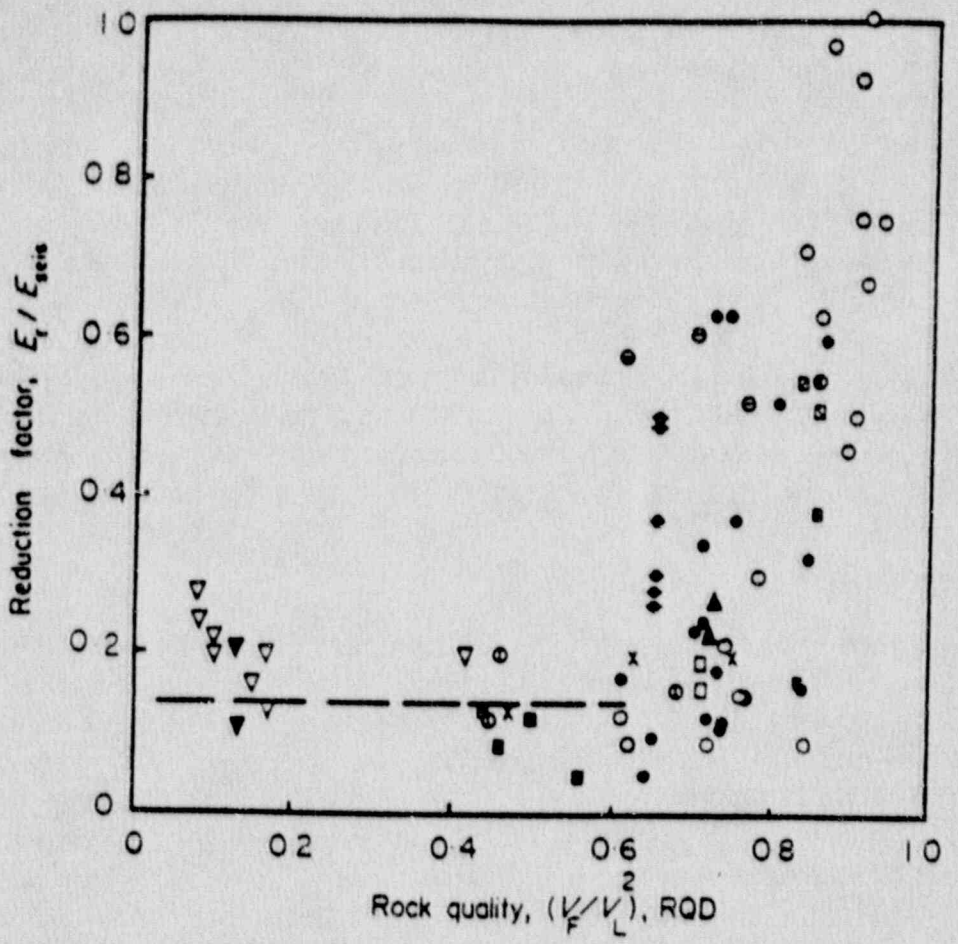

- Dworshak Dam, pressure chamber test (F), buried gauges
- Dworshak Dam, pressure chamber test (F), surface gauges
- Dworshak Dam, pressure chamber test (E), buried gauges
- Dworshak Dam, pressure chamber test (E), surface gauges
- Dworshak Dam, jacking tests, surface gauges
- Dworshak Dam, jacking tests, buried gauges
- Latiyan Dam, Iran
- Kariba Dam, slightly weathered gneiss
- Kariba Dam, heavily jointed quartzite
- Nevada test site, dacite porphyry
- Morrow Point Dam
- Ananaigawa Dam
- Agri River, Italy
- Koshibu Dam, jacking tests
- Koshibu Dam, pressure chamber tests
- El Noville, Mexico
- Onodera
- Vajont Dam, Italy, upper slope, pressure chamber test

Figure A-4. Variation of modulus reduction factor with rock quality. (Ref. A-7)

First, we briefly summarize our review of soil materials; then we summarize our review of the rock materials.

Soil materials. The rate of loading can significantly affect both the compressive strength and the deformation modulus. For soil materials, the shear behavior is controlled by the effective stress state of soils and thus depends on the level of pore-water pressure generated by the loading conditions. If the rate of loading is slow enough to allow pore-water pressure dissipation, then there is no pore-water pressure generated, and the load is transmitted by intergranular soil particles. Therefore, the soil is loaded in a drained condition. However, if the rate of loading is extremely high—such as that associated with an aircraft crash or package drop—the shear of soil is in the undrained condition because there is not enough time to allow pore-water pressure to dissipate through the drainage of pore spaces in the soils. Thus, the effect of loading is also dependent on the degree of saturation and the type of soils (i.e., how well water drains from the soil).

We have done an extensive review of the effect of loading rate on the shear strength and compressibility of various soil types with different degrees of saturation (Ref. 17). Generally, for dry or moist sandy soil, the effect of high strain-rate on shear strength is not significant because of the high compressibility of the air. The presence of air in the pore spaces has very little effect on effective stress until the degree of saturation is greater than 85%: at this point, the effects become important. For soils whose pore spaces are saturated with water or contain a large portion of water, the effect of high strain-rate loading on the strength and deformability is very significant. A. Casagrande and S. D. Wilson (Ref. A-8) studied the effect of rate of loading on the strength of clays and shales and showed that the strength ratio increases from 1 to a range of 1.75 to 2.2 when the time-to-failure changes from 1 to 10^{-4} min. Table A-3 taken from R. V. Whitman (Ref. A-9) indicates that the strength of cohesive soil can increase by factors of 1.5 to 2 (with some factors as high as 4) when the rate of strain was increased by a factor of about 10^4. L. Bjerrum, et al. (Ref. A-10) and R. E. Crawford et al. (Ref. A-11) conducted tests on two different normally consolidated marine clays, and they demonstrated that excess pore-water pressure generated during shear was considerably less for shorter times to failure than for slower rates of loading. The soils which are loaded rapidly must attain a larger shear stress than the soils loaded slowly because the excess pore-water pressure is lower. Their results showed that the strength of the marine clay increases about 20% to 35% from the slow rate of 200 h to failure to a moderately higher rate of 0.1 h to failure. During the 1960s, several studies were performed at the Massachusetts Institute of Technology (MIT) and U.S. Army Engineer Waterway Experiment Station (WES) that examined the strain-rate phenomenon within a range of higher rates of loading. The results of these studies for a variety of soil types—including sands, silty sands, clayey silt, silty clay, and fat clay—indicated trends of response very similar to the findings described above. The details of these studies may be found in R. V. Whitman and K. A. Healy (Refs. A-12 and A-13), A. M. Richardson (Refs. A-14 and A-15), and K. A. Healy (Refs. 31 through 33).

Table A-3. Summary of transient-loading triaxial tests on cohesive soils (Ref. A-9).

	PI %	PL %	w %	Chamber Pressure psi	Static Compressive Strength psi	Strain-Rate Effect* At Low Stress (1/2 to 4%)	Strain-Rate Effect* At Peak Stress
Medium-soft, slightly sensitive clay, undistributed	24	26	27	0	10	2.0	4.0
Compacted silty sand	17	11	12	0	25	1.8	2.7
Normally consolidated, sensitive ocean sediment, undisturbed	63	49	92	0	0.3	2.0	2.4
Tough compacted fill	41	21	26	42	35	2.0	2.0
Slightly organic silty clay; undisturbed, saturated	21	22	35	0	22	1.6	1.9
				85	54	1.7	1.7
Compacted silty sand	17	11	16	0	10	1.7	1.7
Plastic clay, remolded	27	38	44	0	15	1.6	1.8
Plastic clay, remolded	27	38	48	0	7	1.6	1.8
Plastic clay, remolded, saturated	38	24	30	60	36	1.6	1.8
Stiff dray clay, undisturbed	23	30	20	0	250	1.4	1.6
				30	330	1.4	1.4
Slightly organic silty clay; undisturbed, saturated							1.6
Compacted silty clay (also sedimented specimens of same soil)			20	0	30		1.3
			20	15	40		1.2
Compacted plastic clay	38	24	25	0	25		1.4
				15	40		1.5
Compacted clay loam	23	22	21	0	13	1.5	2.5
				30	15	1.5	1.7

* Ratio of resistance at 1000%/s to resistance at 0.03%/s.

The effects of strain-rate on stress-deformation behavior (modulus) are also important considerations for modeling the dynamic response of a soil mass. It has been found that the increase of soil stiffness as measured by shear modulus due to the increase of strain-rate is approximately in the same proportion as soil strength increases. The details of the results can be found in Refs. A-8, A-9, and A-13. In addition, stress/strain responses to strain-rate changes have been discussed by A. Casagrande and W. L. Shannon (Refs. A-19 and A-20) and Y. P. Void and R. G. Campanella (Ref. A-21).

The effect of high transient loading on compressibility has been shown by J. V. Farr (Ref. A-22) for four partially saturated soils. Fig. A-5 shows the pressure/volumetric strain curves for Enewetak beach sand under different strain-rate conditions. Note that at the same value of volumetric strain, the tests for higher strain-rate require higher applied stress. The results of other tests of flume sand, Yuma clayey sand, and Vicksburg Loess show a similar effect. Based on the results

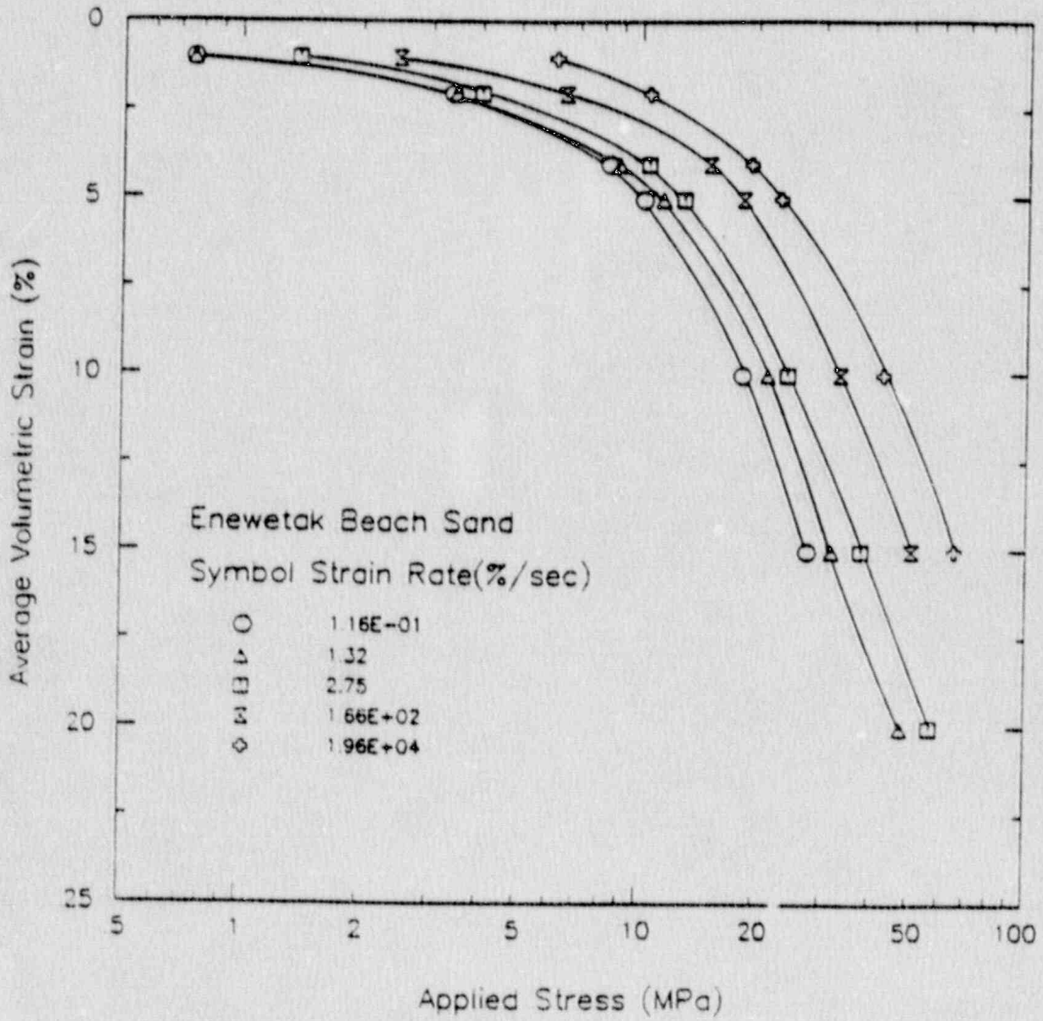

Figure A-5. Strain-rate effect on pressure/volumetric characteristics of Enewetak beach sand. (Ref. A-22)

of laboratory tests and comparison with field tests, Farr concluded that an order of magnitude stiffening of soil uniaxial strain loading moduli does not occur under large impulse-type loading with times to peak pressure of less than 1 ms. As speculated by Jackson et al. (Ref. A-23), increases in moduli ranging up to 125% were determined for the soils tested at their field values of water content and density.

Rock materials. The strain effect on strength and deformation modulus are also very important for rock materials. There is substantial evidence that both stiffness and strength values increase as strain-rates increase. S. Serdengecti and G. D. Boozer (Ref. A-24) showed that the unconfined compressive strength of the Berea sandstone increases from 55 to 83 MPa (8000 to 12,000 psi) when the specimen was tested from a moderate slow rate of 30 s to failure to a higher rate of 0.03 s to failure. The strength increases about 50%. A. Kumar (Ref. A-25) studied the effect of strain-rate on the strength of basalt and granite, and he showed that on the low side of the intermediate range, the effect of changes in strain-rate is not dramatic; however, above the strain-rate of 10^3/s the strength increases rapidly. S. J. Green and R. D. Perkins (Ref. A-26) reported the results of uniaxial compression tests at strain-rates from 10^{-4} to 10^4/s on Solenhofen limestone, Westerly granite, and dry tuff. The limestone shows sensitivity of fracture stress to strain-rate, particularly at the high strain-rates. For the high rates of loading, the stress increased almost exponentially at the rate shown in Fig. A-6. The stress, strain-rate behavior of Solenhofen limestone and room temperature and atmospheric pressure are shown in Fig. A-7. The deformation and fracture of Westerly granite were found to be affected by dynamic loading over strain-rates from 10^{-4} to 10^3/s. The stress-strain curves are shown in Fig. A-8. The end points of these curves define the fracture points and the ultimate stress for the specimen. The bars indicate the data scatter for 4 to 8 tests per condition. It is obvious that the fracture stress increases with strain-rates. Stiffness also increases with strain-rate, with the approximately linear slope varying from about 570 to 860k bars. Dry tuff rock exhibited sensitivity to the rate of loading through increased fracture stress, with rates as shown in Fig. A-9.

The increase of stiffness with an increase of strain-rate is also observed. R. D. Perkins, et al. (Ref. A-27) did similar tests on porphyritic tonalite at strain-rates covering quasistatic (10^{-3}/s) to stress wave (10^3/s) regions. Their test results also indicate that the ultimate stress and stiffness were strain-rate sensitive, showing increased strength and increased stiffness with increased strain-rate. A factor of about 1.8 in stress ratio was found between the test at a strain-rate of 3×10^{-4}/s and the test at a strain-rate of 1.6×10^3/s. The pressure and volumetric strain of the material for testing rates of 3×10^{-4}/s and 6×10^{-1}/s, are shown in Fig. A-10. It is observed that the stress increases about 70% at a certain volumetric strain level (0.22%) from the quasistatic test to the dynamic test.

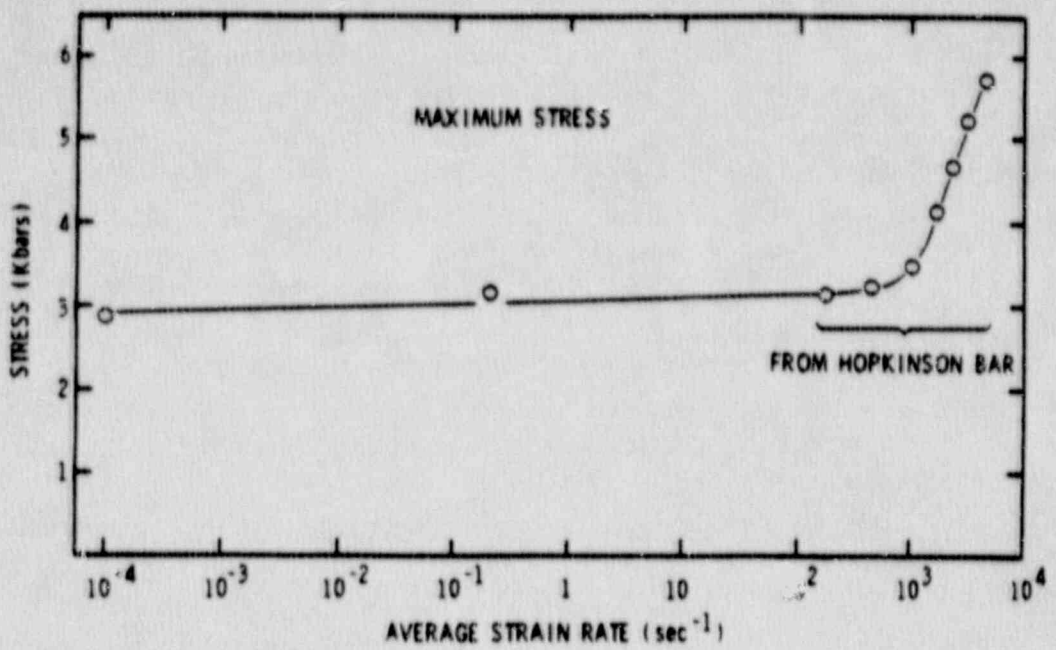

Figure A-6. Fracture stress versus log strain-rate for Solenhofen Limestone. (Ref. A-26)

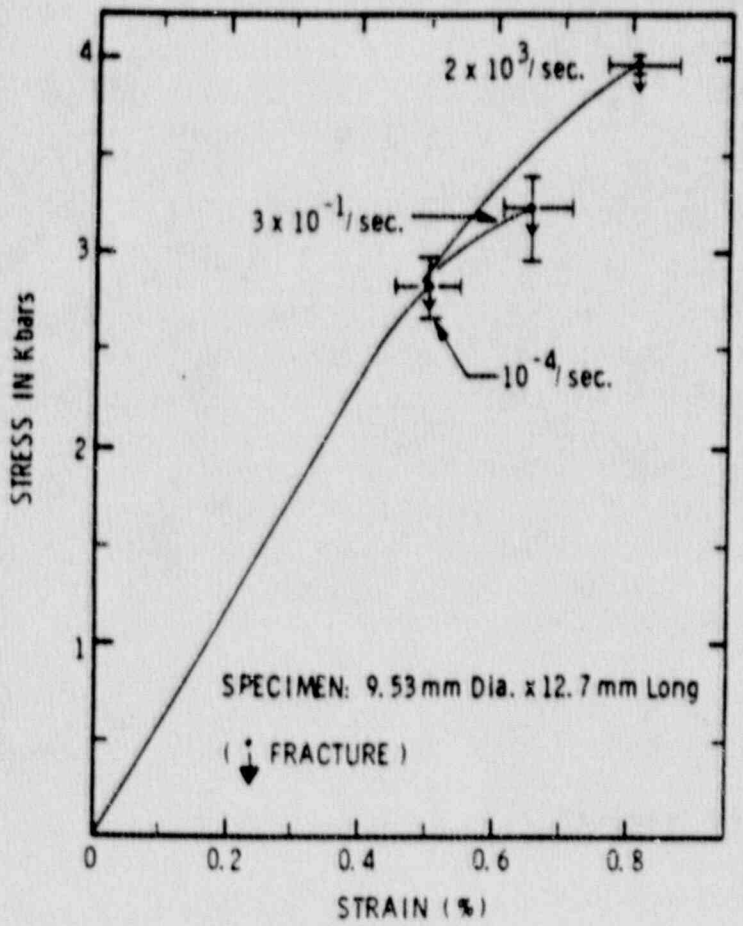

Figure A-7. Stress, strain-rate behavior of Solenhafen Limestone. (Ref. A-26)

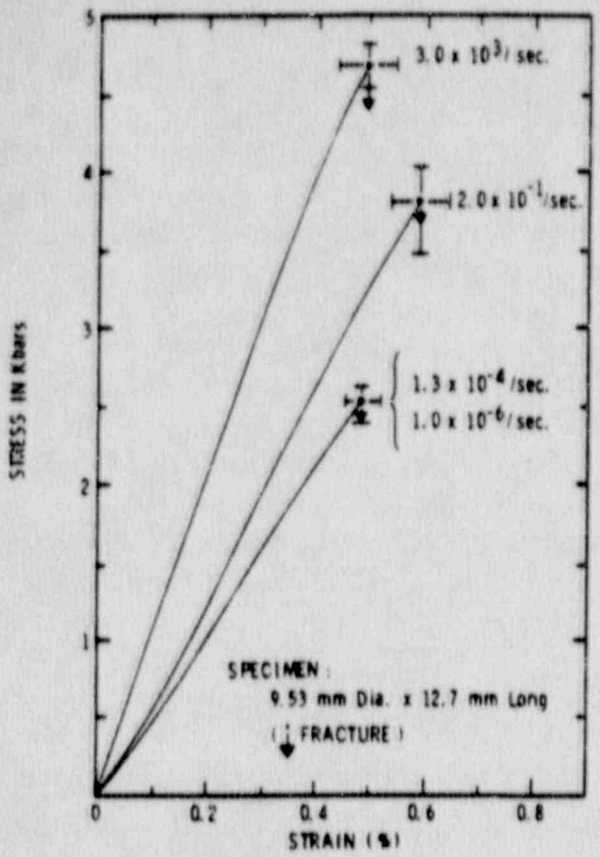

Figure A-8. Stress, strain, strain-rate behavior of Westerly granite. (Ref. A-26)

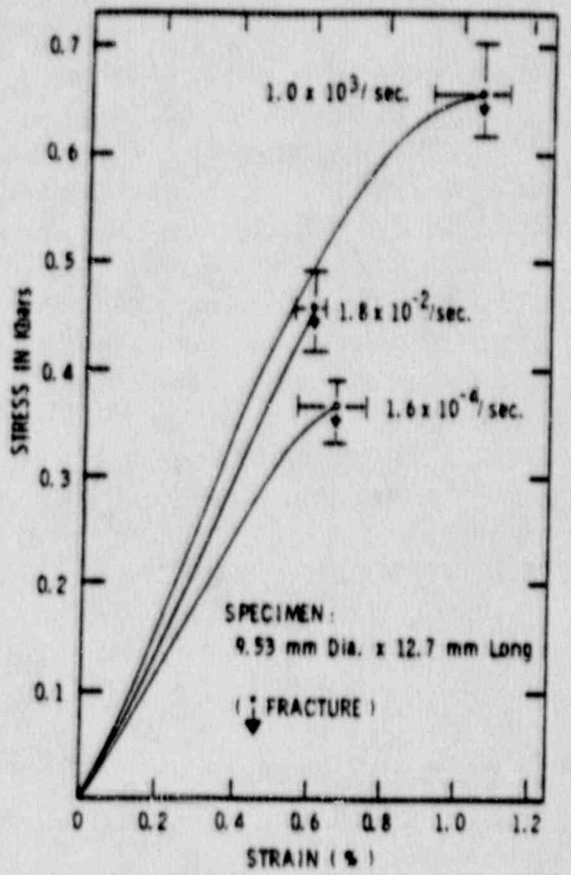

Figure A-9. Stress, strain, strain-rate behavior of volcanic tuff. (Ref. A-26)

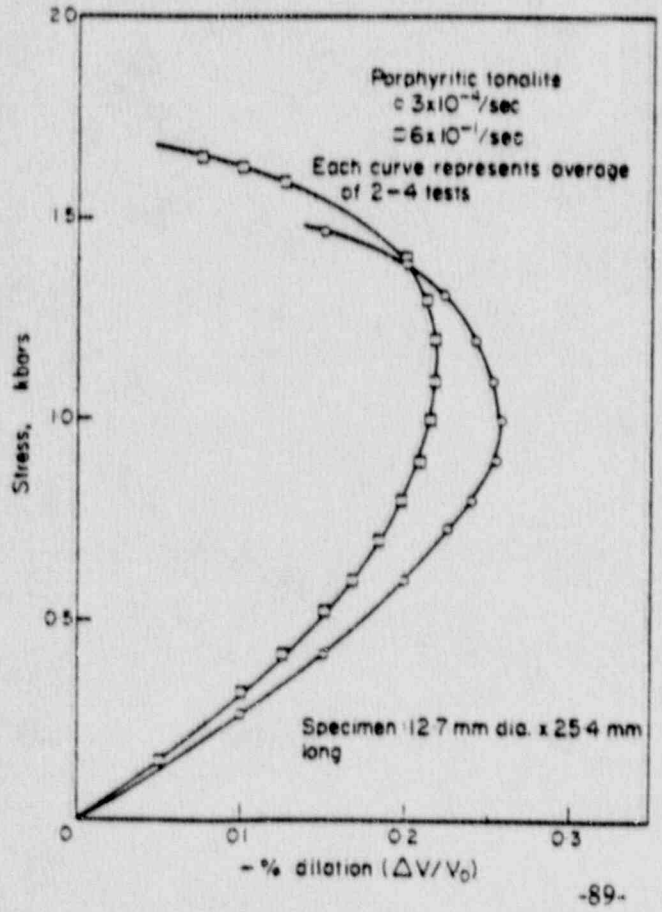

Figure A-10.
Strain-rate effect on volume change as a function of stress level for rock cores of porphyritic tonalities.
(Ref. A-27)

The effect of the rate of loading on strength and Young's modulus of elasticity of three types of rocks (including basalt, granite, and tuff from the Nevada Test Site) has been reported by R. L. Stowe and D. L. Ainsworth (Ref. A-28). Table A-4 shows their testing results for average ultimate strength, Young's modulus, and Poisson's ratio for different loading rates. It can be seen that the strength and modulus of the basalt are not greatly affected by a small increase in loading rates. However, when the loading rate increases to the order of 10^7 psi/s (shock loading test), the ratios of rapid-to-static strength and modulus increase to 1.65 and 1.56, respectively. Only one static and one dynamic test for granite are shown—the ratios for strength and modulus are 1.27 and 1.28. The test results of tuff show that the ratio of rapid to static strength may go up to 2.58 and that the ratio of rapid to static modulus is 1.56. The confined compressive strength of the three rocks studied increased with an increase in the logarithmic rates of loading. Young's modulus of elasticity increases with an increase in the rate of loading up to about 2×10^{11} psi/s. This is based on a comparison of the constrained modulus calculated from the shock loading data and unconstrained modulus of all three rocks.

Table A-4. Average static and rapid unconfined test results (Ref. A-28).

Type of rock	Loading Rate, psi /s	Ultimate compressive strength, psi	Young's modulus of elasticity 10^{-6}, psi	Poisson's ratio	No. of specimens
Basalt	1	20,960	4.28	0.37	3
Basalt	50	21,570	4.47	0.28	3
Basalt	500	21,840	4.72	0.29	3
Basalt	2.06×10^5	25,280	3.25	0.34	3
Basalt	3.13×10^6	28,170	5.00		
Basalt	1.29×10^7	32,390	4.68	0.20	1
Basalt	1.34×10^7	34,580	6.66	0.25	1
Basalt	1.60×10^7	32,120	4.73	0.23	1
Granite	50	24,490	9.26	0.33	3
Granite	1.00×10^7	30,990	11.82	0.22	7
Tuff	50	1,640	0.54	0.19	3
Tuff	1.68×10^5	1,850	0.33	0.42	1
Tuff	3.11×10^5	2,490	0.41	0.49	1
Tuff	8.46×10^5	4,230	0.91	0.36	1

R. N. Shock and H. C. Heard (Ref. 4A-29) studied the static mechanical properties and shock loading response of granite and combined their data with data published by J. M. Logan and J. Handin (Ref. A-30) showing the effect of strain-rate on failure surface (Fig. 3A-11). The increase in strain-rate raises the failure surface. The increase in strength for an order of magnitude increase in strain-rate is

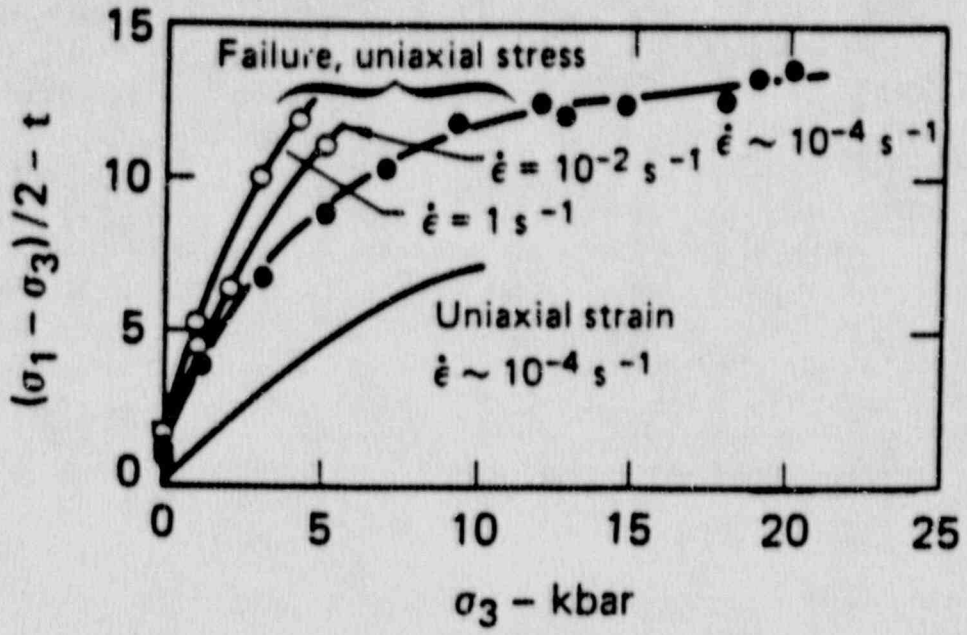

Figure A-11. Strain-rate effect on failure envelopes of rock cores of Westerly granite. (Ref. A-29)

approximately 10%. Thus it can be expected that, at the high rate characteristic of shock loading (~10^4 to 10^{-6}/s), the level of the failure surface will be raised at least 50 to 60%. Strain-rate effects on the mechanical properties of oil shale have been reported by P. M. Hoyt, et al. (Ref. A-31) and J. Lankford, Jr. (Ref. A-32). J. Lankford, Jr. investigated the strain-rate dependence of strength and ductility for oil shale. Lankford tested 98 specimens at various confining pressures and various strain-rates (from 1.73×10^{-4} to 1.87×10^3/s). From 18 confined tests, Lankford concluded that failure strength increased with strain-rate, while the inelastic strain-to-failure was essentially invariant with respect to strain-rate. The actual strength of the shale nearly tripled, going from about 62.1 to 165.6 MPa (9 to 24 ksi) as the strain-rate varied from 1.7×10^{-4} to 2×10^3/s. K. P. Chong et al. (Ref. A-33) investigated the influence of strain-rate on the ultimate compressive stress, the ultimate strain, and the initial Young's modulus for oil shale of Green River Formation in Wyoming. They tested 300 specimens with strain-rates varying from 1×10^{-1} to 1×10^{-1} /s. They found that the ultimate fracture stress of oil shale under compressive conditions was observed to be influenced linearly by the volumetric organic content and the logarithmic strain-rate. The linear relationship enables the ultimate strength to be extrapolated into the impact strain-rates of 10^4 /s. The results of higher strain-rate tests showed a higher Young's modulus than those at the lower strain-rate. The effect of strain-rate on the initial average Young's modulus and the Poisson's ratio for Colorado shales were recently reported by K. P. Chong et al. (Ref. A-34).

T. L. Blanton (Ref. A-35) investigated the effect of intermediate strain-rate (10^{-2} to 10 s^{-1}) on the mechanical behavior of three rocks: Charcoal granodiorite, Berea sandstone, and Indiana limestone. For each rock at each confining pressure, the ultimate strength is relatively constant up to a strain-rate of s^{-1}; apparently, the ultimate strength increases abruptly above this strain-rate. Blanton argued that the apparent sudden increase in strength is due to (test) machine inertia and does not reflect a real increase in the strength of the rocks. Unfortunately, his tests were limited to the rate of 10/s. The effect of machine inertia on the high strain-rate induced by impact loading are not clear at this time. Fig. A-12 shows the overplots of the effect of strain-rate on compressive strength for different rocks tested by the different investigators cited in this section. Similar data (Fig. A-13) were presented by R. Kobayaski (Ref. A-36) showing the experimental variation of compressive strength with strain-rate for different rocks.

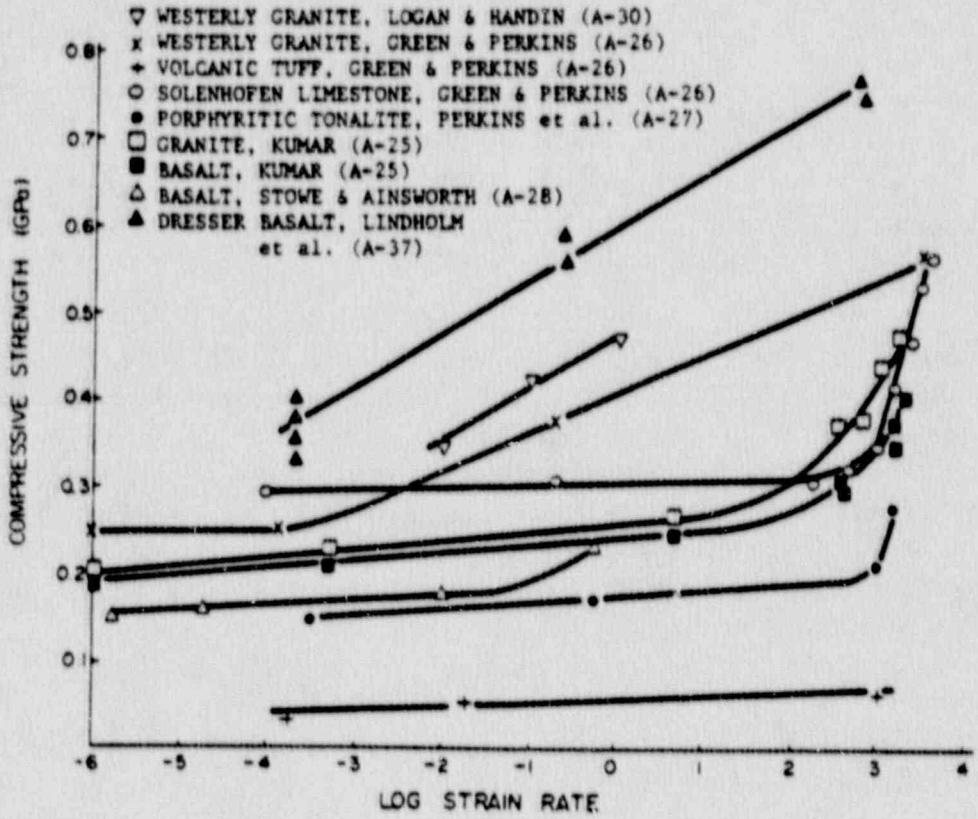

Figure A-12. Strain-rate effect on compressive strength of core samples of different rocks. (Ref. A-35)

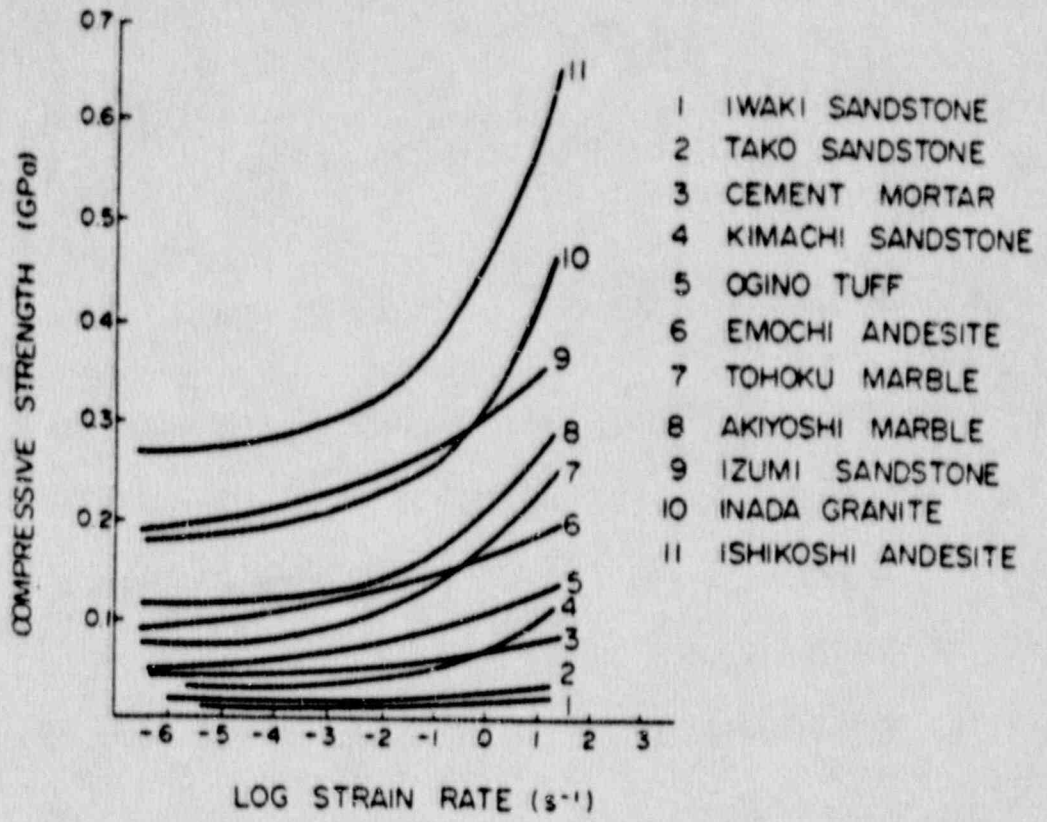

Figure A-13. Experimental variation of compressive strength with strain rate from Kobayaski. (Ref. A-36)

REFERENCES

A-1. J. M. Raphael and R. E. Goodman, *Strength and Deformability of Highly Fractured Rock*, Journ of the Geotechnical Eng. Division, ASCE, GT11, pp. 1285-1300 (November 1977).

A-2. U.S. Corps Engineers, *Strengthening of Rock Against Shock Effects*, Piledriver Project, MRD Lab. 64/90, U.S. Army Corps Engineers, Mo River Div. Lab., Omaha, NB (1964)

A-3. H. R. Pratt, A. D. Black, W. S. Brown and W. F. Brace, *The Effect of Specimen on the Mechanical Properties of Unjointed Diorite*, Int. Jour. Rock Mechanics and Mining Science, VA ,pp. 513-529 (1972)

A-4. W. S. Brown, and S. R. Swanson, *Influence of Load Path and State of Stress on Failure Strength and Stress-Strain Properties of Rocks*, Report UTEC 70-025, University of Utah, Mechanical Engineering Department (1970).

A-5. Z. T. Bieniawski, *Determining Rock Mass Deformability: Experience from Case Histories*, Int. J. Rock Mechanics and Mining Science, **15**, 5, pp. 237-247 (October 1978)

A-6. F.E. Heuze, *Scale Effects in the Determination of Rock Mass Strength and Deformability*, Rock Mechanics, **12**, pp. 167-192 (1979).

A-7. D. V. Deere, A. J. Hendron, Jr., F. D. Patton, and E. J. Cording, *Design of Surface and Near Surface Construction in Rock*, Symp. Rock Mech., 8th, MN (1966).

A-8. A. Casagrande and S. D. Wilson, *Effect of Rate of Loading on the Strength of Clays and Shales at Constant Water Content*, Geotechnique, **2**, No. 3, pp. 251-263 (1951).

A-9. R. V. Whitman, *The Response of Soils to Dynamic Loading, Report No. 36*, Contract Report No. 3-26, U.S. Army Engineer Waterway Experiment Station, Vicksburg, MS.

A-10. L. Bjerrum, N. Simons, and I. Torblaa, *The Effect of Time in the Shear Strength of a Soft Marine Clay*, Proceedings of the Conference on Earth Pressure Problems, Brussels. Belgium, I, pp. 148-58 (1958).

A-11. R. E. Crawford, C. J. Higgins and E. H. Bultmann, *The Air Force Manual for Design and Analysis of Hardened Structures*, Report AFWL-TR-74-102, Air Force Weapons Laboratory, Kirtland Air Force Base, NM (1974).

A-12. R. V. Whitman, and K. A. Healy, *Shear Strength of Sands During Rapid Loadings*, Journal of the Soil Mechanics and Foundation Engineering Division, ASCE, 88, SM2, pp. 99-132 (April 1962).

A-13. R. V. Whitman and K. A. Healy, *Shearing Resistance of Sands During Rapid Loadings, Report 9: The Response of Soils to Dynamic Loadings*, U.S. Army Engineer Waterways Experiment Station, Vicksburg, MS (May 1962).

A-14. A. M. Richardson, Jr. , *The Response of Soils to Dynamic Loads; Report 6: Effect of Rate of Strain on Stress-Strain Behavior of Saturated Soils*, U.S. Army Engineer Waterways Experiment Station, Vicksburg, MS (April 1961).

A-15. A. M. Richardson, Jr., *The Response of Soils to Dynamic Loadings, Report 16: Effective Stress Versus Strength-Saturated Fat Clay*, U.S. Army Engineer Waterways Experiment Station, Vicksburg, MS (April 1963).

A-16. K. A. Healy, *The Response of Soils to Dynamic Loadings, Report 11: Triaxial Tests Upon Saturated Fine Silty Sand*, U.S. Army Waterways Experiment Station, Vicksburg, MS (1962).

A-17. K. A. Healy, *The Response of Soils to Dynamic Loadings, Report 13: The Dependence of Dilation in Sand on Rate of Shear Strain*, U.S. Army Waterways Experiment Station, Vicksburg, MS (1963).

A-18. K. A. Healy, *The Response of Soils to Dynamic Loadings, Report 15: Undrained Strength of Saturated Clayey Silt*, U.S. Army Waterways Experiment Station, Vicksburg, MS (1963).

A-19. A. Casagrande and W. L. Shannon, *Research on Stress Deformation and Strength Characteristics of Soils and Soft Rocks Under Transient Loading, Soil Mechanics Series No. 31*, Harvard University, Cambridge, MA (1948).

A-20. A. Casagrande and W. L. Shannon, *Stress-Deformation and Strength Characteristics of Soils Under Dynamic Loads*, Proceedings of the Second International Conference on Soil Mechanics and Foundation Engineer, V, pp. 29-34 (1948).

A-21. Y. P. Vaid and R. G. Campanella, *Time -Dependent Behavior of Undisturbed Clay*, J. of the Geotechnical Engineering Division, ASCE, **103**, GT7, pp. 693-709, (July 1977).

A-22. J. V. Farr, *Loading Effects on the One-Dimensional Compressibility of Four Partially Saturated Soils*, Technical Report SL-86-46, U.S. Army Engineer Waterways Experiment Station, Vicksburg, MS.

A-23. J. G. Jackson, Jr., J. Q. Ehrgott, and B. Rohani, *Loading Rate Effects on Compressibility of Sand*, Misc. Paper SL-79-24, U.S. Army Waterways Experiment Station, Vicksburg, MS (1979).

A-24. S. Serdengecti and G. D. Boozer, *The Effects of Strain-rate and Temperature on Behavior of Rocks Subjected to Triaxial Compression*, Proc. Symp. Rock Mech 4th Bull. Mineral Ind. Expt. Sta. Penn State University, No. 76 (1961).

A-25. A. Kumar, *The Effect of Stress Rate and Temperature on Strength of Basult and Granite*," Geophysics **33**, 501 (1968).

A-26. S. J. Green and R. D. Perkins, *Uniaxial Compression Tests at Varying Strain-rates on Three Geologic Materials*, Proc. 10th Symposium on Rock Mechanics, Austin, TX, pp. 35-54 (Port City Press, Baltimore, MD, 1972)

A-27. R. D. Perkins, S. J. Green, and M. Friedman, *Uniaxial Stress Behavior of Porphyritic Tonalite at Strain-rates to 10^3/seconds*, Int. J. Rock Mech. and Min. Sci. 7, pp. 527-535, (Pergamon Press 1970)

A-28. R. L. Stowe and D. L. Ainsworth, *Effect of Rate of Loading on Strength and Young's Modulus of Elasticity of Rock in Basic and Applied Rock Mechanics*, Proc. of 10th Symposium on Rock Mechanics (Editor Gray), Austin, TX, pp. 3-34 (Port City Press, Baltimore, MD, 1972).

A-29. R. N. Schock and H. C. Heard, *Static Mechanical Properties and Shock Loading Response of Granite*, Journal of Geophysical Research, **79**, (11) (April 1974).

A-30. J. M. Logan and J. Handin, *Triaxial Compression Testing at Intermediate Strain-rate Proc. of 12th Symposium on Rock Mechanics*, edited by G. B. Clark, pp. 167-194, American Institute of Mining, Metallurgical and Petroleum Engrs., MO (1970).

A-31. P. M. Hoyt, B. Y. Paulsen, K. P. Chong, and J. W. Smith, *Strain-rate Effects on Mechanical Properties of Oil Shale*, presented at Society for Experimental Stress Analysis, Spring Meeting, Wichita, KS, paper No. CR-6 (1978).

A-32. J. Lankford Jr., *Dynamic Strength of Oil Shale*, Soc. Petrol. Engrs., pp. 17-22, (1976).

A-33. K. P. Chong, P. M. Hoyt, J. W. Smith, and B.Y. Paulsen, *Effects of Strain-rate on Oil Shale Fracturing*, Int. Journ. Rock Mech., Mining Science, and Geomechanics., **17**, pp. 35-43, (Pergamon Press Ltd. 1980).

A-34. K.P. Chong, J. S. Harkins, M. D. Kuruppu, and A. L. Leskinen, *Strain-rate Dependent Mechanical Properties of Western Oil Shale*, in 28th U.S. Symposium on Rock Mechanics, Tucson, AZ (June 29-July 1, 1987).

A-35. T.L. Blanton, *Effect of Strain-rates from 10^{-2} to 10 sec^{-1} in Triaxial Compression Tests on Three Rocks*, Int. Journ. Rock. Mechanics, Mining Science, and Geomechanics, **18**, pp. 47-62, (Pergamon Press Ltd. 1981).

A-36. R. Kobayaski, *On Mechanical Behavior of Rocks under Various Loading-Rates*, Rock Mechanics of Japan, **1**, 56 (1970).

A-37. U. S. Lindholm, L. M. Yeakley, and A. Nagy, *The Dynamic Strength and Fracture Properties of Dresser Basalt*, Int. J. Rock Mech. Min. Sci. and Geomech. Abstr. 11, 181 (1974).